UNIVERSITY OF CALIFORNIA
RIVERSIDE

Thermal Decomposition of Molecules Relevant to Combustion and Chemical Vapor Deposition by Flash Pyrolysis Time-of-Flight Mass Spectrometry

A Dissertation submitted in partial satisfaction
of the requirements for the degree of

Doctor of Philosophy

in

Chemistry

by

Jessy Mario Lemieux

December 2013

Dissertation Committee:
Dr. Jingsong Zhang, Chairperson
Dr. Christopher Bardeen
Dr. David Bocian

The Dissertation of Jessy Mario Lemieux is approved:

_____

_____

_____

Committee Chairperson

University of California, Riverside

ACKNOWLEDGMENTS

Professor Jingsong Zhang

Dr. Steven Chambreau

Dr. Kevin Weber

Paul Jones

Jeff Lefler

Mike Fournier

Stan Sheldon

Professor Christopher Bardeen

Professor David Bocian

DEDICATION

This work is dedicated to my parents who taught me the value of curiosity and learning and have always been there for me.

ABSTRACT OF THE DISSERTATION

Thermal Decomposition of Molecules Relevant to Combustion and Chemical Vapor Deposition by Flash Pyrolysis Time-of-Flight Mass Spectrometry

by

Jessy Mario Lemieux

Doctor of Philosophy, Graduate Program in Chemistry
University of California, Riverside, December 2013
Dr. Jingsong Zhang, Chairperson

Flash pyrolysis coupled with vacuum-ultraviolet photoionization time-of-flight mass spectrometry was used to study the thermal decomposition mechanisms of molecules relevant to fuel combustion and the chemical vapor deposition (CVD) of SiGe, SiC, and GeC. For combustion research, the thermal decomposition of benzyl radical, n-alkanes C_nH_{2n+2} (n = 5-8 and 10), 1-butyl radical, and 1-pentyl radical was performed. Benzyl was confirmed to decompose primarily by ejection of H atom after significant isomerization with loss of methyl observed as a minor decomposition pathway. Thermal decomposition of n-alkanes by C-C bond homolysis was directly observed with preferential fission of central C-C bonds. Methyl radical formation by homolysis of the α C-C bond was observed to be the least significant C-C bond homolysis pathway. Decomposition of 1-butyl by β-scission to form ethene and ethyl radical was directly observed. Significant isomerization of 1-pentyl radicals by 1,4-H migration followed by

β-scission was observed at temperatures below 900 K with direct β-scission of 1-pentyl becoming increasingly prevalent at higher temperatures. Gas phase CVD research included pyrolysis of SiH_4/GeH_4 mixture, tetramethylsilane, tetramethylgermane, and several methylchlorosilanes. Formation of highly unsaturated $SiGeH_z$, Si_2GeH_z, Si_3GeH_z, $SiGe_2H_z$, $SiGe_3H_z$ and $SiGe_5H_z$ clusters in the pyrolysis of a 1 to 1 SiH_4/GeH_4 mixture by a silylene/germylene insertion mechanism was observed. The decomposition of tetramethylsilane and tetramethylgermane by Si-C bond homolysis was confirmed and newly observed secondary decomposition mechanisms were demonstrated. The decomposition of methyltrichlorosilane (MTS), an established SiC CVD precursor, was studied. Decomposition occurred primarily via Si-C bond homolysis at temperatures below 1350 K with elimination of CH_3Cl to form $SiCl_2$ becoming increasingly important as the pyrolysis temperature was increased. The mechanism of MTS decomposition was also compared to two other potential precursors, dimethyldichlorsilane and methyldichlorosilane.

TABLE OF CONTENTS

LIST OF TABLES

LIST OF FIGURES

LIST OF SCHEMES

CHAPTER 1

Introduction

Free radicals, molecules with one or more unpaired electrons, are significant intermediates in a variety of important chemical processes including atmospheric chemistry, fossil fuel processing and combustion, metabolism, interstellar chemistry, and chemical vapor deposition (CVD). The study of free radicals is complicated by the fact that they are highly reactive and, thus, have very short lifetimes. The work in this dissertation involves the study of gas phase free radical intermediates present in thermal decomposition processes relevant to fuel combustion and CVD.

Traditionally, the kinetics of free radical processes, such as fuel combustion and CVD, has been studied by the use of static reactors, flow reactors, or shock tubes with gas chromatographic or mass spectrometric detection.[1] Pyrolysis and sampling times for these techniques are generally on the 10 ms to 10 s time scale. Stable end products are detected and often kinetic modeling is used to infer the identities and reactions of free radical intermediates. Time-resolved spectrometric methods have, more recently, been used to attempt unambiguous detection of radical intermediates and their concentrations, but this is often difficult due to spectral interference from other species.

Advances in computational hardware and theoretical chemistry have allowed for the construction of complex kinetic models and for accurate estimates of the geometries

and energetics of transient free radical intermediates and stable products. Theoretical calculations also allow for the determination of activation energies for potential reaction pathways which has been particularly useful in elucidating pyrolysis mechanisms as they generally follow the lowest energy pathways. Nevertheless, a comprehensive understanding of pyrolysis mechanisms would require complete identification of all reactions and intermediates in a mechanism and all of the kinetic parameters for these reactions, which is still currently impractical using computational methods alone. Direct observation of free radicals and other reactive intermediates in the early stages of thermal decomposition reactions could help to verify and improve current kinetic models and to identify previously unconsidered reaction pathways.

In this work, flash pyrolysis coupled with vacuum-ultraviolet photoionization time-of-flight mass spectrometry (VUV-PI-TOFMS) is used to directly observe radicals and reactive intermediates during the early stages of the pyrolysis of molecules relevant to fuel combustion and CVD. Species of interest, diluted in an inert carrier gas, undergo fast flow through a heated micro-reactor followed by immediate supersonic expansion into high vacuum resulting in a molecular beam, effectively cooling and isolating reactive intermediates before detection by VUV-PI-TOFMS. Heater contact times are in the range of 20 – 100 μs, significantly faster than those in traditional methods, allowing for direct detection of species produced by early unimolecular decomposition reactions.[2]

For combustion research, the thermal decomposition of benzyl, n-butyl, and n-pentyl radicals as well as n-alkanes C_nH2_{n+2} (n = 5-8 and 10) was performed. Benzyl

radical is the main decomposition product of toluene, an important fuel. Toluene is commonly used in jet fuels and as an octane booster in gasoline and can be present in concentrations of up to 15 %.[3] It has also been traditionally used as the primary component in racing fuel. Decomposition products of toluene and benzyl radical have been implicated in the formation of carcinogenic polyaromatic hydrocarbons (PAHs) and soot during combustion.[4] Soot, in turn, is known to cause poor air quality contribute to global climate change.

Linear alkanes are also significant components of gasoline and other fuels. The concentration of various alkanes in gasoline has, in fact, increased in recent years as regulations have been enacted to require lower concentrations of aromatics such as benzene, which is known to be carcinogenic. Linear alkanes are of particular interest because they are known to contribute significantly to engine knock. Due to the industrial importance of alkanes, their pyrolysis reactions have been studied for decades.[5] Pyrolysis of n-alkanes has long been known to follow a radical chain mechanism initiated by the cleavage of C-C bonds.[6] Due to the highly reactive nature of the radicals produced and their numerous potential decomposition pathways, details of alkane pyrolysis mechanisms have been elusive. This work includes a study of the pyrolysis of a series of n-alkanes. Pyrolysis of n-butyl and n-pentyl radicals is also performed to investigate secondary decomposition of these radicals in alkane pyrolysis and as an expansion to work that was done previously on ethyl and propyl radicals in this lab by Weber. et al.[7]

Also investigated are thermal decomposition processes relevant to CVD. CVD involves the high temperature reaction of chemical precursors which decompose to produce a solid film on a substrate. It is commonly used in the semiconductor industry for the production of Si wafers and in the production of other novel materials such as SiGe, SiC and GeC. Numerous engineering studies have been performed to grow and evaluate the quality of SiGe, SiC and GeC thin films produced from a variety of chemical precursors and under a variety of pressure and temperature conditions, but the mechanistic details of these processes are not well understood.[8] Pyrolysis of SiH_4/GeH_4 mixture, tetramethylsilane, tetramethylgermane, and a series of methylchlorosilanes is performed to investigate the gas phase decomposition reactions relevant to the SiGe, SiC and GeC deposition processes.

References

(1) Miller, J. A.; Fisk, G. A. *Chemistry and Engineering News* **1987**, *35*, 22.

(2) Kohn, D. W.; Clauberg, H.; Chen, P. *Review of Scientific Instruments* **1992**, *63*, 4003–4005.

(3) Ji, C.; Egolfopoulos, F. N. *Proceedings of the Combustion Institute* **2011**, *33*, 955–961.

(4) Da Silva, G.; Trevitt, A. J. *Physical Chemistry Chemical Physics : PCCP* **2011**, *13*, 8940–52.

(5) Safarik, I.; Strausz, O. P. *Research on Chemical Intermediates* **1996**, *22*, 275–314.

(6) Kossiakoff, A.; Rice, F. *Journal of the American Chemical Society* **1943**, *65*, 590–595.

(7) Weber, K. H.; Lemieux, J. M.; Zhang, J. *The Journal of Physical Chemistry A* **2009**, *113*, 583–91.

(8) Ge, Y.; Gordon, M. S.; Battaglia, F.; Fox, R. O. *The Journal of Physical Chemistry A* **2007**, *111*, 1475–86.

CHAPTER 2

Experimental

2.1 Apparatus Summary

Thermal decomposition experiments were conducted using a flash pyrolysis vacuum ultraviolet photoionization time-of-flight mass spectrometer (VUV-PI-TOFMS) apparatus constructed in this lab. A diagram of the pyrolysis source and VUV-PI-TOFMS apparatus is shown in Figure 2.1. The pyrolysis source was based on a design by Chen and coworkers[1] and interfaced with a Wiley-Mclaren type linear time-of flight mass spectrometer obtained from R.M. Jordan Corporation (model D-651) allowing for resolution of 200 at m/e = 150.[2]

Analyte molecules diluted in He or Ar at a total backing pressure of 1.5 atm were expanded into vacuum through a SiC nozzle (Carborundum Corp.) with inner diameter 1.0 mm attached to machined alumina piece using a high temperature ceramic adhesive and mounted to a pulsed valve (General Valve, Series 9) with orifice diameter 0.75 mm operating at 10 Hz and 200 μs pulse width. The alumina piece was approximately 1.0 cm long and contained a 1.0 mm diameter inner channel to allow the passage of sample gases. It insulated the pulsed valve from the SiC nozzle both thermally and electrically. A MACOR disc and ceramic screws were used to secure the alumina piece against the pulsed valve for additional mechanical stability.

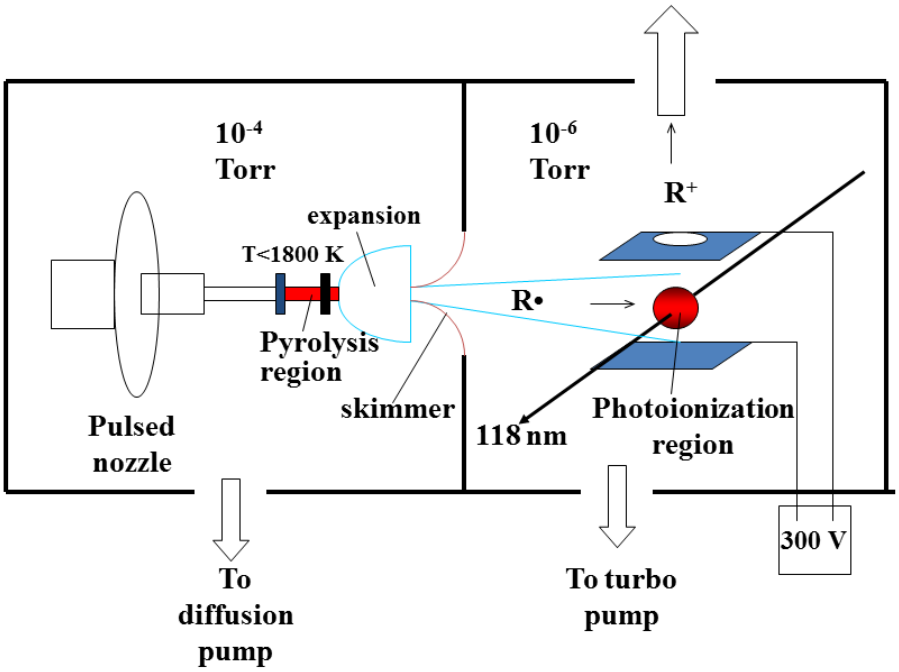

Figure 2.1 Schematic of the flash pyrolysis photoionization time-of-flight mass spectrometer apparatus.

The SiC nozzle was heated resistively by passing current through two graphite electrodes (Poco Graphite) spaced 1.0 cm apart that were press fitted onto the nozzle. Current was controlled by a Variac transformer with light bulbs, connected in parallel, used as current limiters. The temperature of the nozzle was monitored using a type C (Omega) thermocouple attached to the outside of the nozzle. The temperature obtained from the thermocouple was calibrated to the internal temperature by inserting a thermocouple, insulated by a custom ceramic piece, into the nozzle and monitoring the temperature of each thermocouple at inner nozzle temperatures between approximately

500 ^{0}C and 1200 ^{0}C yielding the empirical relationship $T_{internal} = 1.38 (T_{external}) – 200\ ^0$C for temperatures measured in ^{0}C.

Pyrolysis products and unreacted parent molecules were cooled and isolated by supersonic expansion into a vacuum chamber. Vacuum was maintained at approximately 10^{-4} torr during pulsed valve operation and 10^{-6} torr prior to operation by a cryobaffled diffusion pump (Varian, VHS-6). Residence time of the gas molecules within the heated region of the nozzle has been estimated by Chen and co-workers using a similar design to be 20 -100 μs.[1] The resulting molecular beam was extracted using a skimmer positioned approximately 1 cm from the nozzle opening before entry into the photoionization region of the linear time-of-flight mass spectrometer which was maintained at a pressure of approximately 10^{-7} torr using a turbomolecular pump.

Products were ionized by 118 nm (10.45 eV) VUV radiation produced by tripling the frequency of the 355 nm output of a Nd:YAG laser in a Xe cell (~30 Torr) attached directly to the vacuum chamber. The 118 nm radiation was focused by a MgF_2 lens through a small aperture into the photoionization region. Spectra were collected on a digital storage oscilloscope (Tektronix TDS3032, 300MHz) using LabView software and were averaged from 512 laser shots.

This technique affords several advantages. Fast flow through the heated region allows for short thermal decomposition reaction times. Subsequent free expansion into vacuum results in significant cooling of reactive intermediates and isolation in a molecular beam minimizing further reaction. Finally, the use of a 118 nm “soft” ionization source reduces photoionization fragmentation of products generally easing

mass spectra interpretation and allowing for direct identification of free radicals and reactive intermediates produced.

2.2 Supersonic Expansion and Molecular Beams

Supersonic expansion of a gas occurs upon passage of gas atoms or molecules from a high pressure (P_0) reservoir to a low pressure (P_b) region. Conditions are similar to those generated in aircraft jet engines where contraction and expansion results in supersonic air flow.[3] Initial conditions of the gas in the reservoir (P_0,T_0) are referred to as the stagnation state. Under significantly high stagnation state pressures, gas flow resulting from the pressure differential can be treated as an adiabatic, isentropic expansion. Gas molecules will undergo supersonic expansion under the condition that the ratio P_0/P_b exceeds G, defined below:

$$G \equiv \left(\frac{(\gamma+1)}{2} \right)^{\frac{\gamma}{(\gamma+1)}}$$

where γ is the ratio of heat capacities at constant pressure and constant volume C_p/C_v.[4]

For ideal monatomic gases, such as He and Ar, C_p is treated as temperature independent and is equal to 5/2 R. Given the adiabatic assumption, the maximum or terminal velocity of these gases in the jet can be expressed as shown below where *M* is the molar mass of the monatomic gas.[3]

$$u_{max} = \sqrt{\frac{5RT_0}{M}}$$

Note that the maximum velocity is independent of reservoir pressure and the background pressure and depends only on the initial temperature and the molar mass of the gas molecules. This equation yields velocities of 1.77×10^5 and 5.59×10^4 cm s^{-1} for He and Ar, respectively at 300 K reservoir temperature. Velocities approaching these values are readily achieved experimentally.[3]

In our experiments, short heater contact times are achieved by near sonic flow velocity of sample and carrier gases through the SiC nozzle. The near sonic flow occurs upon the entry of gases through the 0.75 mm opening of the pulsed valve into the 1.0 mm diameter nozzle. Collision with the walls of the nozzle results in a series of expansions and contractions resulting in an average flow velocity that is approximately sonic providing a contact time with the heated zone of 20 – 100 μs.[1,5] Measurements by Chen and coworkers confirmed that gas pulse duration and flow velocity from a 4 cm long extension tube versus that of a bare pulsed valve are essentially identical above 1.0 atm stagnation pressure.[1] Pyrolysis precursors differ in mass from the carrier gas but attain the same flow velocity as He or Ar due to repetitive collisions with the carrier gas molecules. This is known as "seeding" of the precursor.

Upon exit from the heated region of the SiC nozzle, gases undergo free expansion. Collisions of product molecules with the carrier gas during expansion result in significant cooling to translational and rotational temperatures under 50 K. Cooling

efficiency is thus, dependent upon the mass of carrier gas with heavier mass carrier gases providing a greater cooling effect. Upon sufficient expansion, gas molecules enter a nearly collision free environment, referred to as the zone of silence, traveling at the terminal velocity of the free jet expansion. This continues until the density the expanding gases approaches that of the background. At this point, a significant increase in entropy occurs as gas particles are rapidly decelerated by collisions with background gases in a shock zone. This zone is referred to as the Mach disk, and its location is given by the following equation where χ_M is the distance of the Mach disk from the source exit and *d* is the nozzle diameter.

$$\frac{\chi_M}{d} = \frac{2}{3}\left(\frac{P_0}{P_b}\right)^{1/2}$$

A skimmer is positioned within the zone of silence to extract molecules into a differentially pumped, low pressure region for detection by VUV-PI-TOFMS. Overall, using this experimental setup, pyrolysis products are cooled by the supersonic expansion, effectively quenching decomposition reactions immediately following passage through the heated region of the SiC tube. Products are also isolated from one another in the collision free environment of the molecular beam preventing further potential bimolecular reactions.

One limitation of this technique is the potential for heterogeneous reactions on the inner surface of the SiC nozzle. This limitation is addressed in two ways: (i) sample molecules are diluted to approximately 1 % or lower molar concentration in inert gas Ar

or He, (ii) sonic flow through the heated region minimizes contact time. The potential for surface reactions was evaluated by Chen and Coworkers using the pyrolysis of t-butyl nitrite $(CH_3)_3CONO$.[6] Heterogeneous decomposition is expected to result in cleavage of the C-O bond to form t-butyl radical and nitrogen dioxide while homogeneous thermal decomposition results in cleavage of the O-N bond forming t-butoxy radical and nitrogen monoxide. Chen et al. observed NO almost exclusively as opposed to NO_2 suggesting little heterogeneous decomposition occurred. Thus, reactions in the SiC nozzle are expected to be primarily homogenous. Nevertheless some extent of heterogeneous reactions is possible. Attempts made by Chambreau et al. in this laboratory to measure the known activation energy of methyl tert-butyl ether by generating Arrhenius plots from MS results yielded values that were 60-70% of the previously measured value.[7] Thus, although pyrolysis in this system appears to be primarily homogenous, this technique cannot be used to reproduce kinetic parameters but is effectively used for qualitative mechanistic insight.

2.3 Vacuum-Ultraviolet Photoionozation Time-of-Flight Mass Spectrometry

After product molecules passed into the VUV-PI-TOFMS chamber, they were ionized by 118 nm single photon ionization. The 118 nm (10.45 eV) VUV radiation was produced by tripling the frequency of the 355 nm output of a Nd:YAG laser in a low pressure Xe cell attached directly to the vacuum chamber. The remaining 355nm fundamental, and the frequency tripled 118 nm radiation, passed through a MgF_2 lens as

it entered the vacuum chamber. Due to the differences in the indices of refraction of 118 nm and 355 nm radiation in the MgF_2 medium, the fundamental 355 nm radiation diverged away from a small aperture leading to the photoionization region, minimizing multiphoton ionization (MPI) and scattered 355 nm radiation in the ionization region.

The 118 nm radiation was focused through the aperture and onto the molecular beam. Alignment of the 118 nm beam and the molecular beam was optimized by adjusting 355 nm focusing lenses in front of the Xe cell, SiC nozzle position, and delay time between the opening of the pulsed valve and the firing of the laser to maximize signal intensity of the peak corresponding to the pyrolysis precursor of interest or a diagnostic standard, such as nitrogen monoxide. Ionization by 118 nm (10.45 eV) single photons results in limited secondary photoionization fragmentation (PIF) of pyrolysis products allowing for unambiguous identification. With a few exceptions, such as diatomic molecules and small organics including ethene and C_nH_{2n+2} ($n < 4$), most products can be ionized and detected.

Due to the divergence of the 355 nm radiation, MPI was minimized in this experimental setup. Removal of the Xe tripling medium resulted in elimination of the ion signal indicating that 355 nm MPI is negligible. MPI due to 118 nm + 355 nm (14.0 eV) photons also appeared to be negligible. This was demonstrated in the pyrolysis mass spectra of pentane (Figure 5.1). MPI fragmentation to produce $C_3H_6^{+\bullet}$ (m/e 42) was not observed although the appearance energy is 11.02, significantly less than 14.0 eV.

One limitation of this system is the occurrence of a small amount of electron impact ionization (EI) due to scattered UV radiation causing the ejection of electrons from metal surfaces. Attempts were made to minimize EI. An iris was employed to minimize the 355 nm spot size before entry into the Xe cell. The size of the aperture allowing 118 nm radiation into the photoionization region was also minimized, however complete elimination of EI was not possible without complete elimination of the photoionization signal as well. Chambreau et al. used 1,3-butadiene as a model system to compare the photoionization mass spectra in this system to an EI mass spectrum obtained by Dannacher et al.[8] and determined that EI contributed to less than 1% of the signal in mass spectra obtained.[7]

Overall, flash pyrolysis VUV-PI-TOFMS has been demonstrated to be an effective way to generate and identify free radicals produced during the initial stages of thermal decomposition reactions. The short reaction time, cooling and isolation of products by supersonic expansion, and the "soft" ionization VUV-PI-TOFMS detection, allow for direct, unambiguous identification of highly reactive intermediates in thermal decomposition reactions.

References

(1) Kohn, D. W.; Clauberg, H.; Chen, P. *Review of Scientific Instruments* **1992**, *63*, 4003–4005.

(2) Lubman, D.; Jordan, R. *Review of Scientific Instruments* **1985**, *56*, 373–376.

(3) Morse, M. *Experimental Methods in The Physical Sciences* **1996**, *29B*, 21–47.

(4) Scoles, G. *Atomic and Molecular Beam Methods*; Vol. 1.; Oxford University Press: New York, 1988.

(5) Chen, P.; Colson, S. D.; Chupka, W. A.; Berson, J. A. *Journal of Physical Chemistry* **1986**, *90*, 2319–2321.

(6) Chen, P.; Colson, S. D.; Chupka, W. A. *Chemical Physics Letters* **1988**, *147*, 466–470.

(7) Chambreau, S. D. Free Radical Production and Thermal Decomposition Mechanisms of Small Molecules by Flash Pyrolysis, University of California, Riverside, 2002, pp. 7–13.

(8) Dannacher, J.; Flamme, J.-P.; Stadelman, J.-P.; Vogt, J. *Chemical Physics* **1980**, *51*, 189–195.

CHAPTER 3

Pyrolysis of Benzyl Radical

3.1 Introduction

Benzyl radical is the primary product of the pyrolysis of substituted benzenes, particularly toluene, and an important intermediate in combustion chemistry. Benzyl is known to be a relatively long lived intermediate because of resonance stabilization and is thus expected to be present in significant concentrations in combustion processes. Due to its importance in combustion chemistry, benzyl pyrolysis has been studied extensively, both experimentally[1–7] and theoretically[8–10], but the decomposition mechanism is still not completely understood.

Benzyl decomposition has been studied using several experimental techniques. Early studies by Smith in 1979 utilized a Knudsen Cell coupled with mass spectrometric detection to monitor toluene decomposition[1]. Rao and Skinner studied decomposition of ethylbenzene and isotopomers using H and D atom atomic resonance absorption spectroscopy (ARAS).[2] Their results indicated that production of C_5H_5 and acetylene from benzyl was a primary decomposition pathway along with some production of C_4H_4 and C_3H_3.

$$C_6H_5CH_2^{\bullet} \rightarrow C_5H_5^{\bullet} + C_2H_2 \qquad (3.1)$$

Decomposition to $C_5H_5^{\bullet}$ and C_2H_2 has also been suggested by shock tube studies performed by Sivaramakrishnan et al. in 1994.[3] Alternatively, shock tube studies performed by Hippler et al. in 1990 suggested a different primary initial decomposition step in which a C_7H_6 fragment and H atom are produced.[5]

$$C_6H_5CH_2^{\bullet} \rightarrow C_7H_6 + H^{\bullet} \qquad (3.2)$$

These results were supported by photolysis experiments by Frochtenicht et al. in 1994 and Song et. al in 2011 as well as shock tube studies by Oehlschlaeger et al. in 2006.[4,6,7]

Benzyl decomposition has also been the subject of several recent theoretical studies. In 1997, Jones et al. performed ab initio calculations to investigate the formation of $C_5H_5^{\bullet} + C_2H_2$ by four proposed mechanisitic pathways.[8] They concluded that the decomposition occurs via a 6-methylenebicyclo[3.1.0]hex-3-en-2-yl (MBH) intermediate with the maximum barrier of about 99 kcal/mol. Recent ab initio studies support a lower energy decomposition mechanism via reaction 3.2 with the C_7H_6 fragment proposed to be fullvenallene with a barrier of about 85 kcal/mol.[9,10]

Fullvenallene was first identified as the most stable C_7H_6 molecule upon an ab inito theoretical investigation by Wong et al. in 1996.[11] In 2009, Cavalotti et. al proposed the formation of fulvenallene through the process depicted in Figure 3.1 also based on ab initio calculations.[9] The mechanism investigated involves the isomerization of benzyl to MBH (**3**). This is followed by further isomerization to the cyclopentadiene-vinyl radical (**10**) and then either (a) direct dissociation to fulvenallene (**13**) and H atom by loss of the

tertiary H atom with an energy barrier of 86.8 kcal mol^{-1}, (b) further isomerization of cyclopentadiene-vinyl radical to cyclopentadienyl-ethene (**12**) radical via 1,2 H shift of the tertiary H atom followed by loss of this H atom with an overall energy barrier of 86.2 kcal mol^{-1}, or (c) isomerization of cyclopentadiene-vinyl radical to cyclopentadienyl-allene (**11**) radical via 1,2-H shift of the tertiary H atom to a vicinial CH group on the ring followed by a loss of this or the other H atom on the same carbon with an overall energy barrier of 81.6 kcal mol^{-1}.

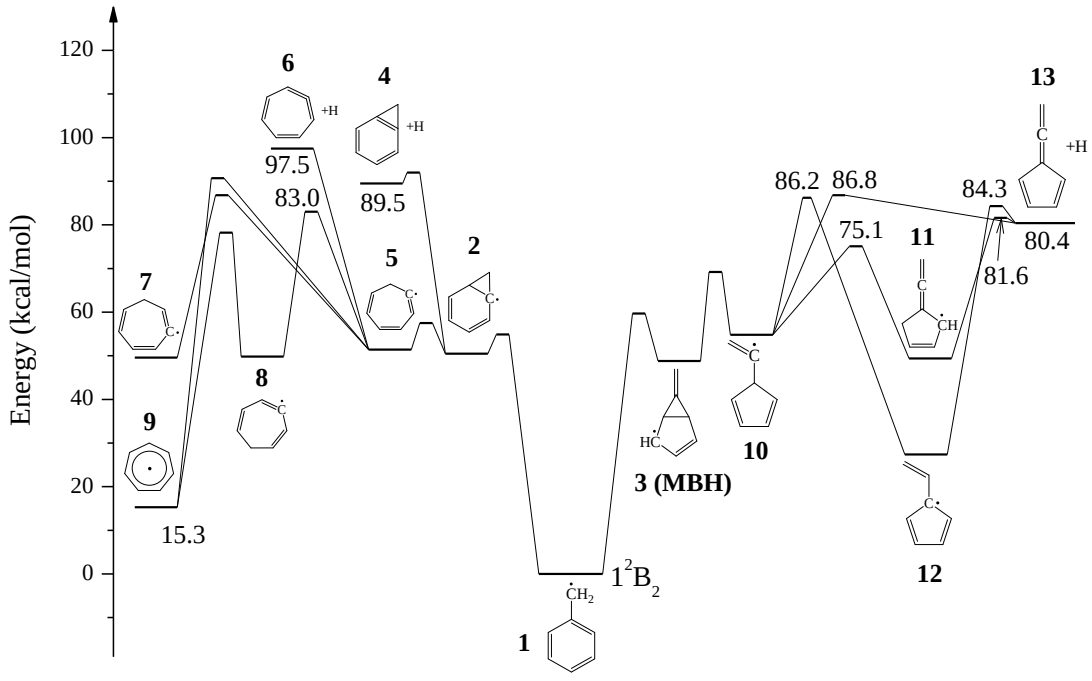

Figure 3.1 Potential Energy diagram of the C_7H_7 system showing 3 potential H- atom dissociation channels based on the theoretical work of Cavalotti et. al. in reference 9. Diagram is based on a diagram by Song et. al. in reference 6.

The initial isomerization in the Cavalotti mechanism to MBH was inspired by the theoretical work of Jones et al. in 1997, although Jones predicted the ultimate formation of cyclopentadienyl radical and acetylene from this pathway. For the formation of C_7H_6 and H atom, Jones invoked a ring opening mechanism with subsequent C-H bond fission. However, Cavalotti later rejected this ring opening pathway in their 2009 ab intio theoretical study because of a probitively high overall reaction barrier of 121.4 kcal mol^{-1}. Da Silva et al. also investigated the reactions shown in Scheme 3.1 and calculated the overall energy barriers of reactions (a), (b), and (c) to be 88.3, 86.1, and 84.9 kcal mol^{-1}, respectively.[10]

In this study, we have used flash pyrolysis vacuum ultraviolet photoionization time-of-flight mass spectrometry (VUV-PI-TOFMS) to pyrolyze benzyl chloride, benzyl bromide, and partially deuterated benzyl chlorides, $C_6H_5CD_2Cl$ and $C_6D_5CH_2Cl$, in order to observe the early stages of benzyl radical thermal decomposition. The flash pyrolysis VUV-PI-TOFMS technique has several features that allow for direct observation of reactive intermediates. Pyrolysis is carried out on a very short (~ 20 to 100 μs) time scale followed by supersonic expansion into vacuum that effectively provides vibrational and rotational cooling and quenches the reaction. The resulting cooling also reduces fragmentation upon laser ionization prior to detection, simplifying spectra interpretation. Photoionization fragmentation is further reduced by the use of "soft" 118 nm (10.45 eV) ionization, which provides sufficient energy to ionize most molecules without significant fragmentation.

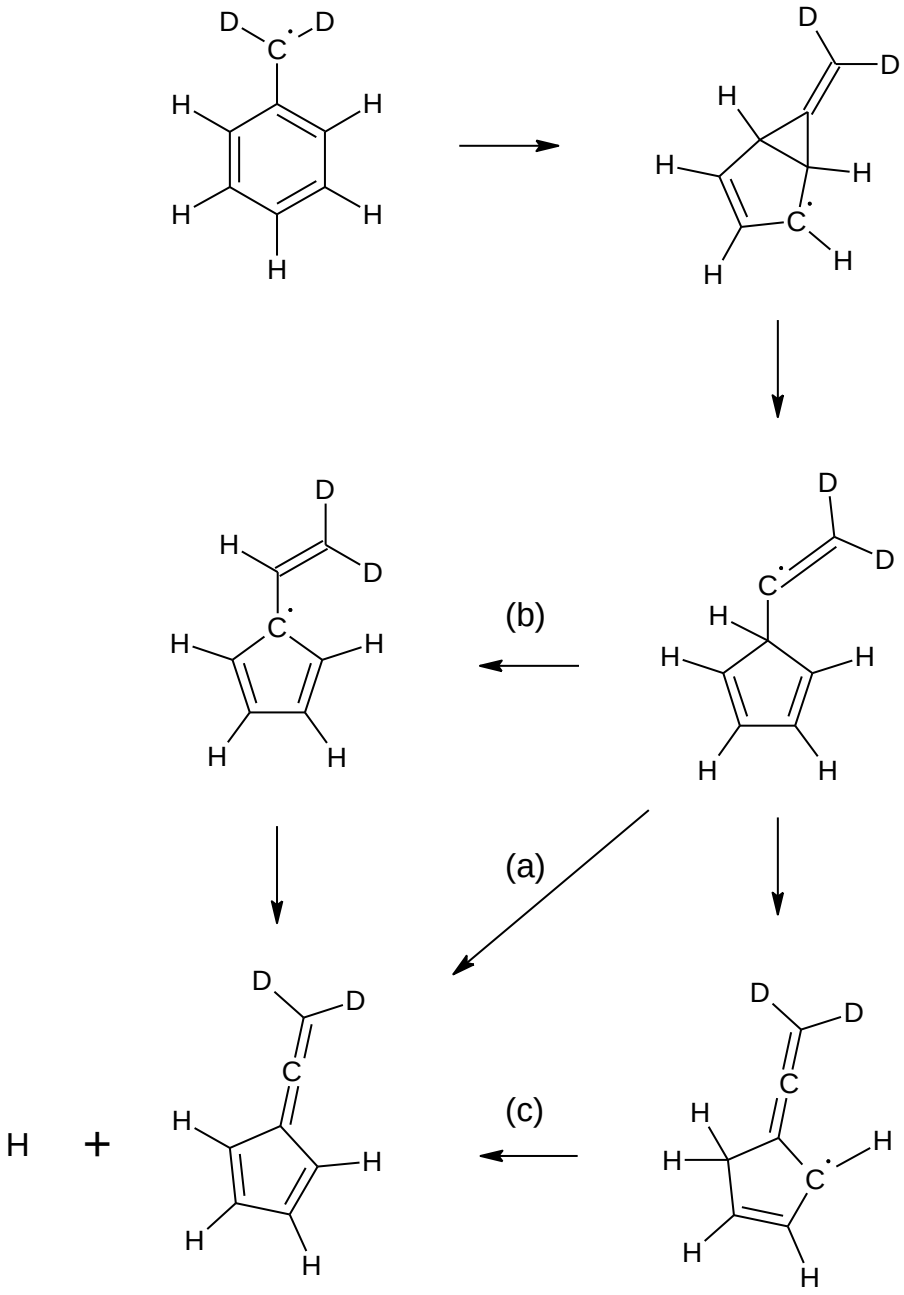

Scheme 3.1 Decomposition of side-chain-deuterated benzyl to fulvenallene and hydrogen atom as proposed by Cavalotti et al. Side-chain H atoms are labeled as D for clarity.

3.2 Experimental

Benzyl radical was obtained by the pyrolysis of benzyl chloride, benzyl bromide, and deuterated benzyl chlorides, $C_6H_5CD_2Cl$ and $C_6D_5CH_2Cl$, using a home-built flash pyrolysis TOFMS apparatus that has been previously described.[12,13] Benzyl chloride (99.9%) and benzyl bromide (99.9%) were obtained from Sigma-Aldrich. Deuterated benzyl chloride samples, $C_6H_5CD_2Cl$ and $C_6D_5CH_2Cl$, were obtained from CDN Isotopes (98% D). Samples were used directly without further purification and were diluted to approximately 1% molar concentration in Ar or He by bubbling the carrier gas through the liquid samples held in a reservoir at approximately 70 ^{0}C.

3.3 Results

(a) Benzyl Chloride, $C_6H_5CH_2Cl$

Mass spectra for the pyrolysis of benzyl chloride, $C_6H_5CH_2Cl$, seeded in He and Ar were taken for temperatures of approximately 900 K to 1500 K. Results of the pyrolysis of benzyl chloride in He are shown in Figures 3.2, 3.3, and 3.4. Pyrolysis of benzyl chloride seeded in Ar is shown in Figure 3.5.

Figure 3.2 shows the results of the flash pyrolysis of benzyl chloride seeded in He at room temperature and temperatures 870 K to 1160 K. At room temperature, 295 K, the prominent peaks are those at m/e 126 and 128 with an intensity ratio of approximately 3 to 1. These peaks represent the parent, benzyl chloride, the 3 to 1 intensity ratio

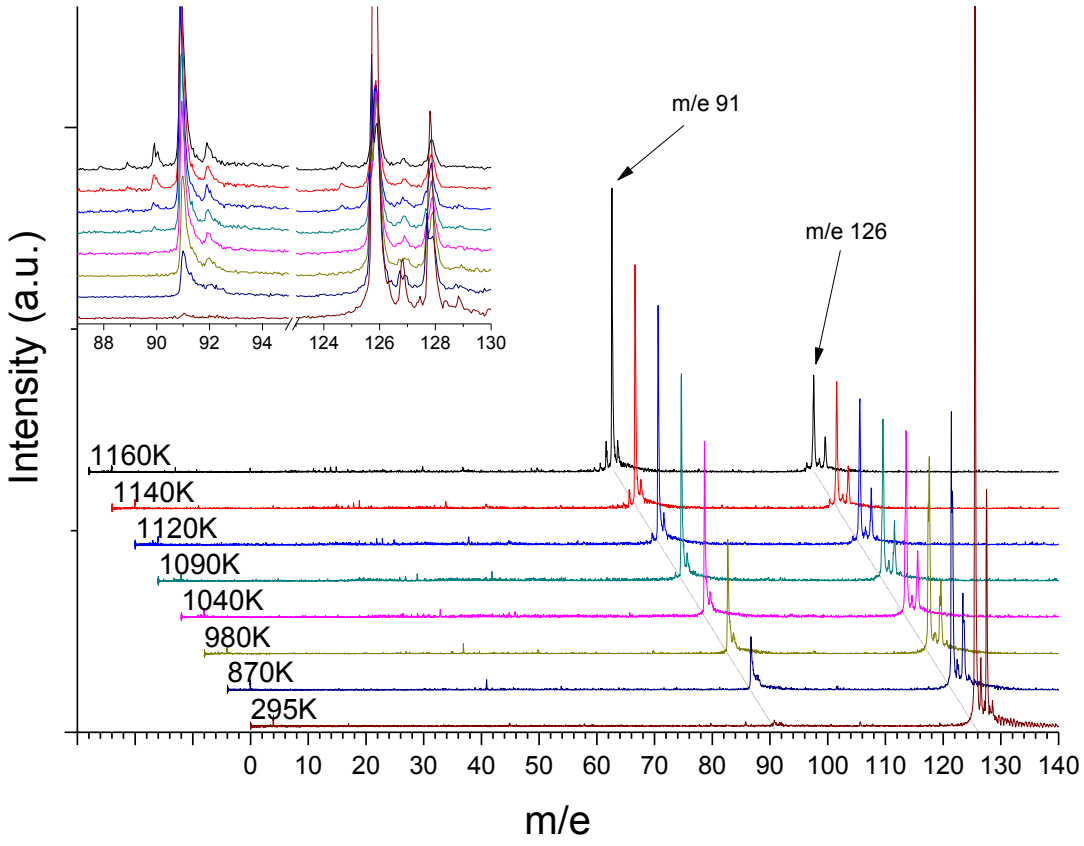

Figure 3.2 Stack plot of mass spectra for pyrolysis of $C_6H_5CH_2Cl$ (~1%) in He at room temperature and pyrolysis temperatures 870 K to 1160 K. Mass spectra are offset for clarity. Inset shows an enlarged view of product peaks in the m/e 88 to 95 and m/e 123 to 130 mass regions.

indicating the natural abundances of ^{35}Cl and ^{37}Cl isotopes that are 0.758 and 0.242, respectively. Small peaks at m/e 127 and 129 are also observed due to a small fraction of ^{13}C isotopes (natural abundance 0.011) among the 7 carbon atoms in the molecule. A very small peak at m/e 91 due to benzyl cation, $C_7H_7^+$, can be seen. A benzyl peak is expected here due to the fact the appearance energy of benzyl from benzyl chloride ionization has been measured to be between 9.85 eV and 10.4 eV, less than the 10.45 eV energy of the photons from our ionization source.[14–16]

Increasing the pyrolysis nozzle temperature leads to the facile production of benzyl radicals. At 870 K, the m/e 91, benzyl, peak grows significantly. There is a noticeable shoulder to the peak indicating a small background due to electron impact (EI) ionization of benzyl chloride. EI occurs with lower spatial resolution than laser ionization causing the peak shoulder. However, the shoulder gradually disappears as the pyrolysis temperature is increased and the thermal decomposition of benzyl chloride to benzyl radical and chlorine atom increasingly dominates. The parent benzyl chloride peaks at 870 K decrease in intensity by more than 50% relative to the room temperature spectrum. This is due to decomposition of the parent molecules and also due to their decreased number density resulting from the large temperature increase. Very small peaks at m/e 58 and m/e 45 are also seen due to a small amount of contaminant in the nozzle from a prior experiment.

As the pyrolysis temperature is raised to 980 K, 1040 K, and 1090 K, production of benzyl radical increases as the m/e 91 peak continues to grow while the parent m/e 126

and 128 peaks decrease in intensity. The intensity of the m/e 91 peak at 1040 K is approximately the same as the intensity of the parent peak and surpasses it at 1090 K. In addition, a small peak at m/e 92 is also visible, again likely due to the natural abundance of ^{13}C isotopes.

At 1090 K and 1120 K, the first signs of benzyl radical decomposition are observed. A small peak at m/e 90 indicates the loss of H atom from benzyl, producing C_7H_6. Molecular elimination of HCl from benzyl chloride could also produce C_7H_6 but this would require 1,1-HCl elimination because there are no H atoms bonded to the neighboring carbon atom. This would ultimately produce an unstable carbene. The unfavorable energetics make HCl elimination unlikely. Also, the m/e 90 peak is not observed at lower temperatures when m/e 91 appears. Peaks at m/e 91 and m/e 90 continue to increase in intensity as the temperature increases to 1140 K and 1160 K. Meanwhile, there is a concomitant decrease in the intensity of the m/e 126/128 parent peaks.

Pyrolysis of benzyl chloride at higher temperatures, 1180 K to 1420 K, is depicted in Figure 3.3. Figure 3.4 shows an enlarged view of the m/e 10 to m/e 87 mass regions at temperatures 1040 K to 1300 K so that early production of pyrolysis products can be more easily seen. Again, the peaks at m/e 58 and m/e 45 are due to a small amount of contaminant that could not be removed. Peaks at m/e 43 and 42 appear at 1120 K as m/e 45 simultaneously decreases in intensity. These peaks do not change in intensity as the

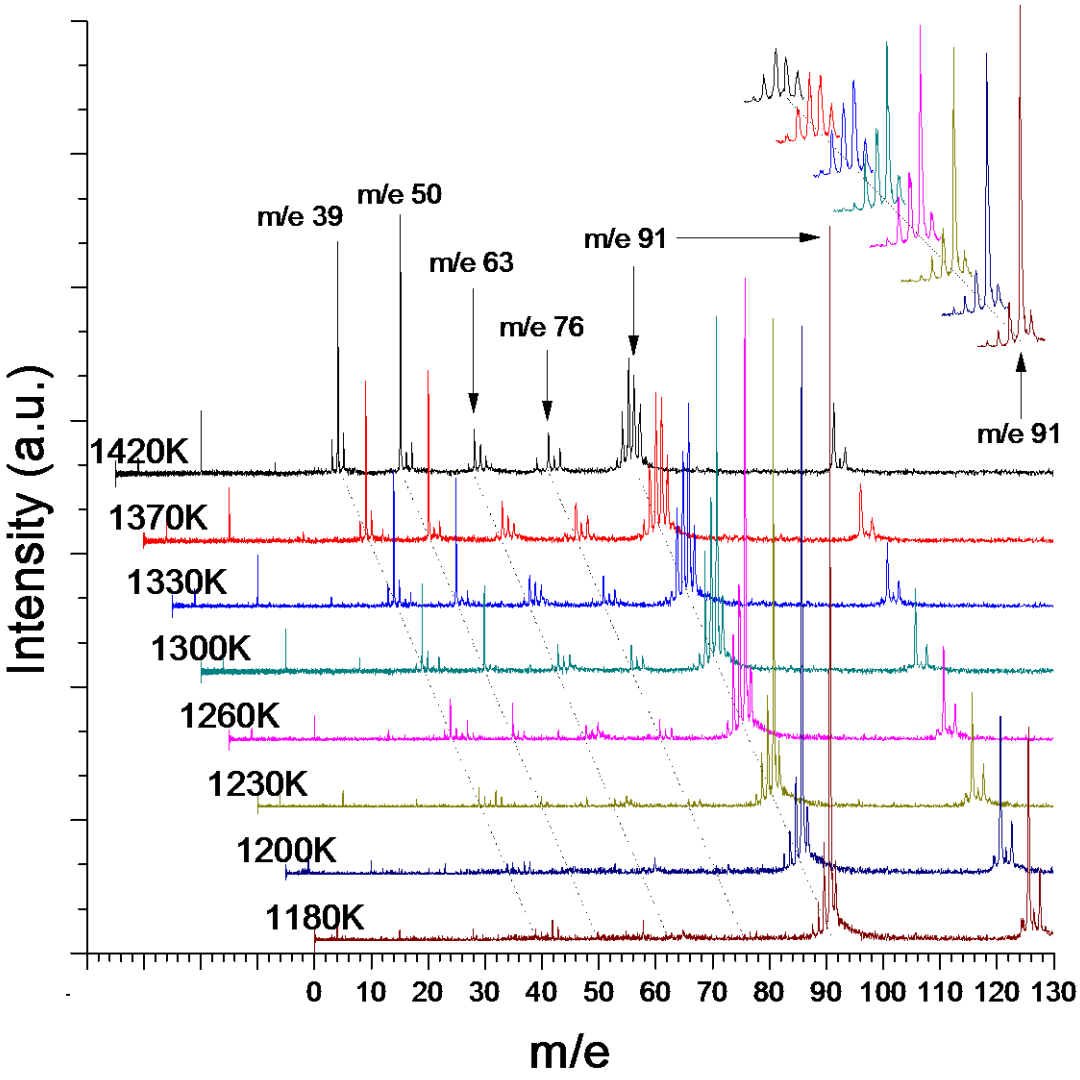

Figure 3.3 Stack plot of mass spectra for pyrolysis of $C_6H_5CH_2Cl$ (~1%) in He at temperatures 1180 K to 1420 K. Mass spectra are offset for clarity. Inset shows enlarged view of m/e 88 through 92 peaks.

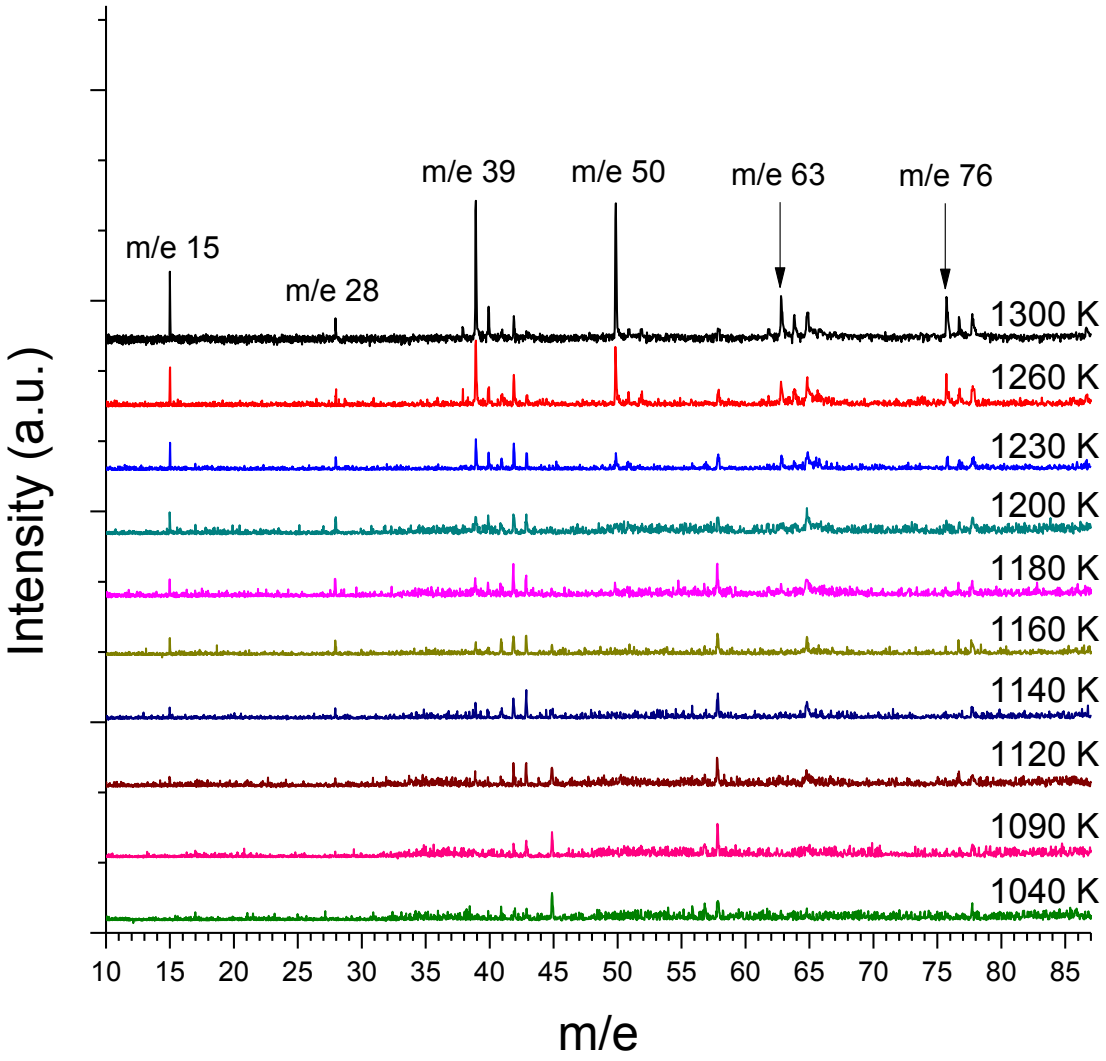

Figure 3.4 Stack plot of mass spectra for pyrolysis of $C_6H_5CH_2Cl$ (~1%) in He at temperatures 1040 K to 1300 K enlarged to show mass range m/e 10 through 87.

temperature is increased and do not appear in the pyrolysis mass spectra of $C_6H_5CD_2Cl$ (see Figure 3.8). Thus, they are not a result of benzyl thermal decomposition.

At 1180 K, the m/e 91 peak reaches its maximum intensity while m/e 126/128 peaks are further attenuated. A small m/e 89 peak appears indicating the loss of 2 hydrogen atoms or H_2 from benzyl. Smaller pyrolysis fragments also begin to be produced. Peaks at m/e 39-43 indicate the production of $C_3H_{3\text{-}7}$. Small peaks at m/e 15 and m/e 28 are due to methyl radical and ethene, respectively. It is important to note the ionization energy of ethene is 10.51eV.[17] This is slightly higher than the energy provided by the ionization source in this experiment. A small amount of thermal energy remaining in the molecule following supersonic expansion may be sufficient to allow the ionization of ethene as seen in the spectra. However, due to the fact that the ionization energy of ethene is higher than 10.45eV, the extent of its production cannot be reliably predicted.

At 1200 K, further production of benzyl radical occurs as indicated by the decreased intensity of the m/e 126/128 peaks. The m/e 91 peak begins to decrease in intensity indicating further decomposition of benzyl radical. Peaks at m/e 89 and 90 maintain a similar intensity relative to the m/e 91 peaks. However, a very small peak at m/e 88 is observed indicating the loss of a third H atom from benzyl radical. A small peak also appears at m/e 65 providing the first indication of $C_5H_5^{\bullet}$ production. Based on previous studies, this is presumed to be the cyclopentadienyl radical.[1,3] The counter fragment of $C_5H_5^{\bullet}$ is C_2H_2 and is assumed, based on the aforementioned studies, to be acetylene. Because of the high, 11.41eV, ionization energy of acetylene, it cannot be

directly observed in this experiment.[18] Peaks at m/e 28 and m/e 39-43 remain essentially constant with the m/e 42 peak shrinking slightly. The m/e 15, methyl, peak grows in intensity by about 20%.

Raising the pyrolysis temperature to 1230 K results in the first definitive production of C_6H_{4-6} peaks as evidenced by the appearance of very small peaks at m/e 76, 77, and 78 all approximately equal in intensity. The m/e 76 peak corresponds to C_6H_4, resulting from the loss of methyl radical from benzyl.

$$C_6H_5CH_2^{\bullet} \rightarrow C_6H_4 + CH_3^{\bullet} \qquad (3.3)$$

As the pyrolysis temperature is increased to 1260 K and 1300K the m/e 76 and m/e 15 peaks each approximately triple in intensity indicating the simultaneous production of C_6H_4 and CH_3. The m/e 63 peak also grows by a factor of 3 as the temperature is increased from 1230K to 1300 K. The counter fragment at m/e 28, indicating ethene, does not grow significantly in this region. Again, this is due to the fact that ethene has an IE slightly above that of the ionization source and is not readily ionized and detected in this system. However, the progress of this decomposition channel can be determined by monitoring the m/e 63 signal.

A peak at m/e 50 also appears at 1230 K, and grows rapidly from 1230 K to 1300 K along with the peak at m/e 39. These represent pyrolysis product fragments C_4H_2 and C_3H_3, respectively indicating decomposition into 3 and 4 carbon containing complementary fragments from benzyl, although 2 H atoms also appear to be lost in the

process. In addition, peaks at m/e 40 and 42 are observed at 1230 K, and peaks at m/e 51 and 52 are observed at 1260 K. Unlike the m/e 39, and m/e 50 peaks, these do not grow significantly at higher temperatures. At 1300 K the m/e 40 peak has approximately 15% of the intensity of the m/e 39 peak and the m/e 51 and 52 peaks have less than 2% of the intensity of the m/e 50 peak.

At the highest pyrolysis temperatures in this experiment, 1330K, 1370 K and 1420 K, the m/e 39 and m/e 50 peaks become dominant. At 1330 K, the m/e 91 peak decreases in intensity by 40% indicating the further decomposition of the benzyl radical. Meanwhile, the m/e 39 and m/e 50 peaks are approximately 80% of the intensity of the m/e 91 peak. The loss of one and two hydrogen atoms from benzyl indicated by m/e 89 and 90, continues to be important at 1330 K up to 1420 K as the m/e 91 intensity continues to fall ultimately becoming slightly less than that of the m/e 90 peak. Peaks at m/e 39 and m/e 50 continue to grow from 1300 K to 1330K. A small peak at m/e 38 is observed at 1330 K, indicating the loss of an H atom from C_3H_3 and grows proportionally to m/e 39 from 1330 K up to 1420K. Peaks at m/e 76, 77 and 78 also increase in intensity as the temperature increases from 1330 K to 1420 K, nearly doubling in intensity. There is also a concomitant increase in the size of the complementary m/e 15 peak. Peaks at m/e 63, 64 and 65 increase to approximately the same extent as the m/e 76, 77, and 78 group between 1330 K and 1420 K.

Pyrolysis of benzyl chloride was also performed using Ar to explore the increased cooling effects and longer reaction times that result from the use of a heavier carrier gas.

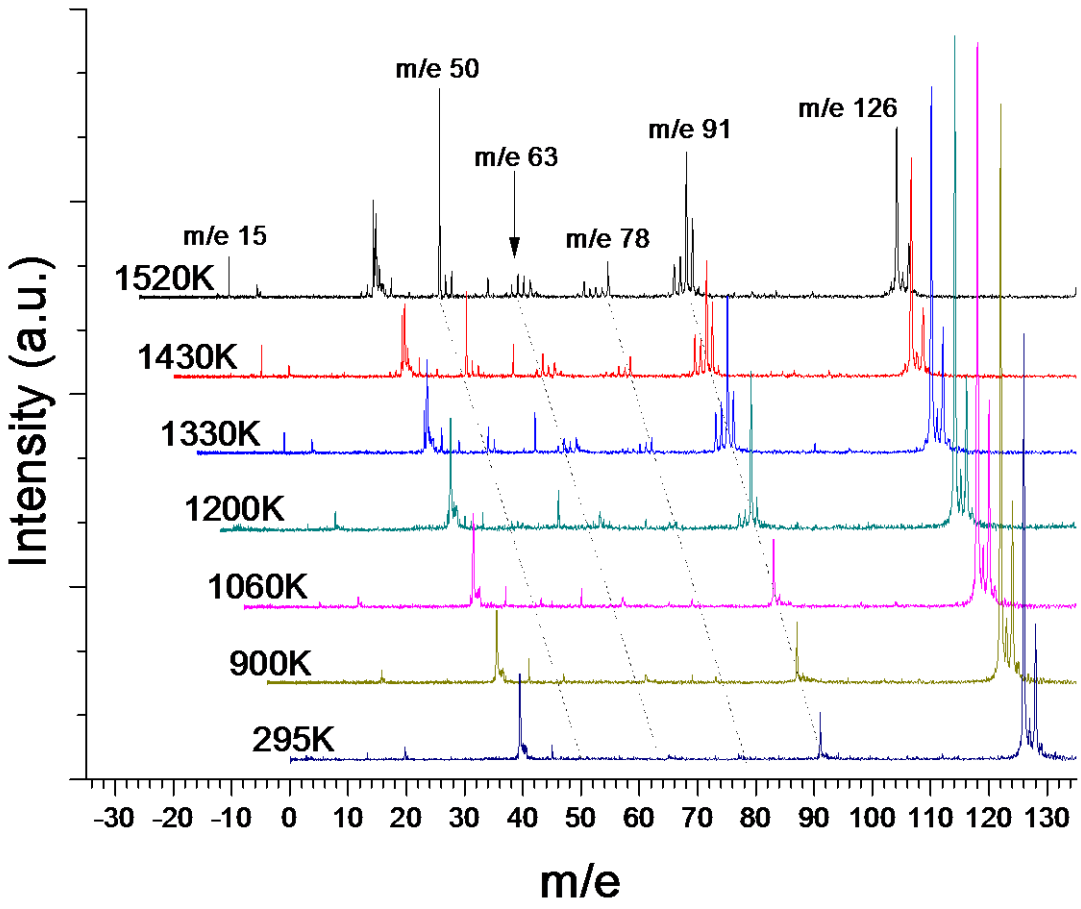

Figure 3.5 Stack plot of mass spectra for pyrolysis of $C_6H_5CH_2Cl$ (~1%) in Ar at room temperature and pyrolysis temperatures 900 K to 1520 K. Mass spectra are offset for clarity.

Results of the thermal decomposition of benzyl chloride seeded in Ar at temperatures between 900 K and 1520 K are shown in Figure 3.5. Results were essentially analogous to those in the He spectra but specifics will be mentioned here briefly. A room temperature background spectrum was taken. The largest peak was the benzyl chloride parent peak at masses 126 and 128. They appear as a pair of peaks with a 3:1 ratio due to ^{35}Cl and ^{37}Cl isotopes. Some electron impact fragmentation of the parent molecule, benzyl chloride, is observed resulting in a peak at 91 corresponding to benzyl radical cation. A very small m/e 65 (C_5H_5) fragment is also observed in the background spectrum. The broad peak at m/e 40 is due to the carrier gas, argon. Argon has an IE of approximately 15.8 eV and is, thus, not readily ionized by the photoionization source in this system.[19] The broad shape of the peak is an indication of electron impact ionization. A small peak at m/e 20 is also observed due to doubly ionized Ar.

Benzyl pyrolysis products are observed at pyrolysis temperatures of 1200 K and above. At 1200 K, the m/e 91, benzyl, peak grows and small peaks appear at m/e 90 and 89, representing loss of one and two hydrogen atoms, respectively, from the benzyl radical. The m/e 65 peak increases slightly in intensity indicating pyrolysis production of C_5H_5. Peaks and m/e 64 and m/e 63 are also present either as a result of secondary reactions or representing loss of hydrogen from C_5H_5.The counter fragment of C_5H_5, C_2H_2, is not observed in the spectra. Because of its high ionization energy, acetylene is not ionized by our ionization source and is, thus, not detected. A small mass 78 peak is

also observed indicating C_6H_6 production. The contaminant m/e 58 peak is observed in these spectra as it was in the He spectra.

At 1330 K, m/e 90 and 89 peaks increase in intensity indicating further H atom loss from benzyl. The m/e 65 C_5H_5 peaks drop slightly with a concomitant increase in the mass 63 peak indicating significant secondary processes or loss of H_2 from C_5H_5. The mass 78 peak does not change significantly. Peaks at m/e 50, 51, and 52 appear at this temperature corresponding to $C_4H_{2\text{-}4}$. Unfortunately, the mass 39, C_3H_3, counter fragment is obscured by the Ar peak. However, the mass 39 peak grows larger at higher temperatures and is observed as a spike on the left side of the broad Ar peak. At 1410 K, all product peaks increase slightly in intensity with the exception of the m/e 50, 51, and 52, $C_4H_{2\text{-}4}$, peaks which increase significantly. Mass 50, 51, and 52 peak intensities increase further at 1500 K. Presumably, the peak at m/e 39 peak increases significantly in intensity as well. However, this cannot be well seen due to the overlap with the broad m/e 40, Ar peak.

The most important difference between the results of the benzyl chloride pyrolysis seeded in Ar and He is the dominance of the m/e 78 peak in the Ar spectra versus the m/e 76 peak in the He spectra. The smaller mass of the He carrier gas results in a shorter reaction time of ~20 μs prior to supersonic expansion of the gases while that for Ar is approximately 3 times longer. The longer time scale in the Ar carrier gas allowed for secondary reactions which ultimately produced the thermodynamically stable benzene

species indicated by the m/e 78 peak. By contrast in the He spectra, there is direct observation of decomposition by reaction 3.3 to produce C_6H_4 and methyl radical.

To summarize, the results of benzyl decomposition in He and Ar, at lower temperatures (~1160 K to ~1320 K) indicate that C_7H_6 is the primary product of benzyl decomposition providing evidence for reaction 3.2 as the lowest energy benzyl decomposition channel. C_5H_5 is also a minor product at lower temperatures indicating some contribution from reaction 3.1. At the highest temperatures (1410 K and 1500 K), C_4H_2 and C_3H_3 are the dominant products. C_4H_3 and C_4H_4 are also observed indicating ultimate decomposition to fragments containing 3 and 4 carbon atoms. These results could indicate benzyl decomposition to C_3H_3 and C_4H_4 fragments, a decomposition channel that has not been well considered in the recent literature.

$$C_6H_5CH_2^{\bullet} \rightarrow C_4H_4 + C_3H_3^{\bullet} \qquad (3.4)$$

Because m/e 39 and 52 peaks appear largely at elevated temperatures, secondary decomposition of other pyrolysis products may also contribute significantly C_3H_3 and C_4H_2 production.

(b) Benzyl Chloride – d_2, $C_6H_5CD_2Cl$

In order to gain greater insight into the benzyl pyrolysis mechanism, pyrolysis of partially deuterated benzyl chloride, $C_6H_5CD_2Cl$, was also performed. The results of the

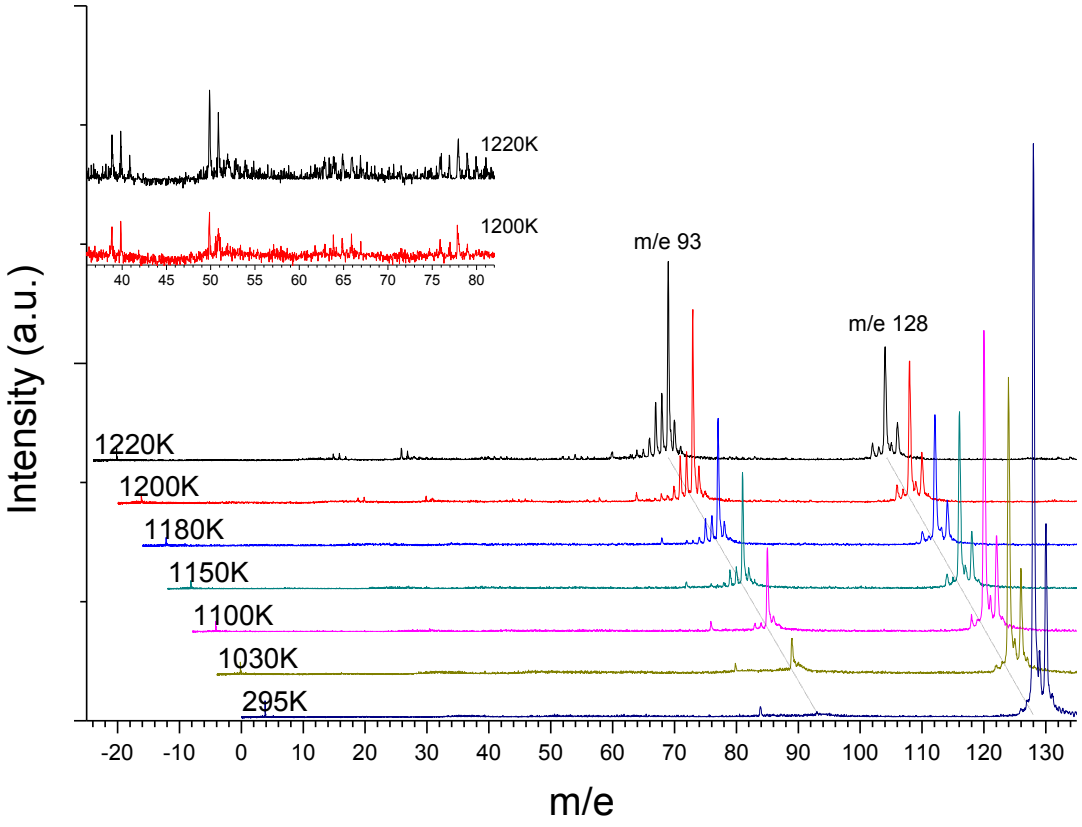

Figure 3.6 Stack plot of mass spectra for pyrolysis of $C_6H_5CD_2Cl$ (~1%) in He at room temperature and pyrolysis temperatures 1030 K to 1220 K. Mass spectra are offset for clarity. Inset shows enlarged view of spectra at 1200 K and 1220 K in the m/e 36 to m/e 82 mass region.

pyrolysis of $C_6H_5CD_2Cl$ seeded in He are shown in Figures 3.6, 3.7, and 3.8. Mass spectra for pyrolysis temperatures 1030 K through 1220 K are shown in Figure 3.6. A peak is seen at m/e 84 at all pyrolysis temperatures due to a very small amount of C_4H_4S contamination left from a previous experiment. Generally, the results were similar to those for the undeuterated sample. The room temperature spectrum contains only the parent in a 3 to 1 ratio doublet at m/e 128 and 130 due to the ^{35}Cl and ^{37}Cl isotope abundances.

A large mass 93 peak appears at pyrolysis temperature 1030 K indicating loss of Cl atom form the parent to form partially deuterated benzyl radical, $C_6H_5CD_2^{\bullet}$. At 1100 to 1150 K, peaks appear at mass 91 and 92 indicating loss of H and D atoms from $C_6H_5CD_2^{\bullet}$. At 1200 K, peaks m/e 92 and 91 increase in intensity. The m/e 91 and 92 peaks are analogous to the m/e 89 and 90 peaks in the pyrolysis of undeuterated benzyl chloride shown in Figure 3.2. Again, HCl/DCl elimination from the parent, $C_6H_5CD_2Cl$, to produce these peaks is unlikely due to the lack of H/D atoms on the carbon atom next to that bonded to the chlorine atom. Notably, the ratio of the m/e 90 peak to that of the m/e 89 peak is approximately 4:1 at 1180 K for the undeuterated sample whereas the ratio of m/e 92 to m/e 91 is about 6:5 for $C_6H_5CD_2Cl$. This indicates significant loss of the deuterium atoms rather than loss of 2 hydrogen atoms located on the ring. Statistically, D atoms are only present in a 2:5 ratio in $C_6H_5CD_2Cl$. Loss of D atom versus H atom is significantly greater at a nearly 5:6 ratio. Potential decomposition pathways responsible for preferential loss of side-chain D atoms in $C_6H_5CD_2Cl$ are considered in the discussion section and shown Scheme 3.2 (see discussion).

At 1200 K, benzyl production increases with the m/e 93 peak surpassing the intensity of the m/e 128 peak by about 20%. Loss of H and D atoms from benzyl continues, the intensity of m/e 92 and 91 being approximately equal at 20% of the intensity of the m/e 93, benzyl, peak. A small peak at m/e 90 appears indicating the loss of 3 H atoms or 1D and 1 H from $C_6H_5CD_2^{\bullet}$ to produce $C_7H_2D_2$ or $C_7H_4D^{\bullet}$, respectively. Loss of 3 H atoms at 1200K in the undeuterated sample, indicated by a very small m/e 88 peak seen in Figure 3.3, is very minimal. Therefore, $C_7H_4D^{\bullet}$ is largely responsible for the m/e 90 peak in the deuterated sample. The H and D atoms lost could be lost sequentially or by HD molecular elimination but 1,2 HD elimination is not possible without isomerization such as that shown in Scheme 3.2. Also, the lowest energy decomposition pathways proposed by Cavolotti et al. depicted in Figure 3.1 and Scheme 3.1 do not allow for 1,2 HD elimination. HD elimination from $C_6H_5CD_2^{\bullet}$ appears to be energetically unfavorable. Very small peaks can also be seen at m/e 88 and 89, m/e 88 primarily representing C_7H_4 production, while m/e 89 corresponds to a mixture of C_7H_3D and C_7H_5 produced by secondary $C_6H_5CD_2^{\bullet}$ decomposition after loss of H or D atom.

Very small peaks at m/e 39 and 40 of approximately equal intensities also appear at 1200K representing C_3H_3 and C_3HD fragments. Both have mass 39 amu, but C_3HD can essentially be ruled out because of the lack of an m/e 38, C_3H_2, peak at 1200K in the pyrolysis of $C_6H_5CH_2Cl$ (Figure 3.4) and the relatively low intensity of m/e 38 at higher temperatures. Both C_3H_4 and C_3H_2D contribute to the presence of the peak at m/e 40. Very small peaks at m/e 50 and 51 are also observed. The m/e 50 peak could correspond to either C_4H_2 or C_4D, however the noticeable absence of an m/e C_4H peak in both the

$C_6H_5CD_2Cl$ and $C_6H_5CH_2Cl$ pyrolysis mass spectra indicate that the peak at m/e 50 is solely due to C_4H_2. The peak at m/e 51 likely has some contribution from both C_4H_3 and C_4HD.

A very small series of peaks also appear at m/e 63 to 67 at 1200K. The m/e 67 peak corresponds to a doubly deuterated cyclopentadienyl radical, $C_5H_3D_2$ analogous to the m/e 65, C_5H_5 peak in the $C_6H_5CH_2Cl$ pyrolysis spectra. Recent theoretical studies have suggested that formation of C_5H_5 occurs via a cycloheptatrienyl radical which dissociates to cyclopentadienyl and acetylene.[8,9] Formation of cycloheptatrienyl would provide effective isotopic mixing allowing for the formation of $C_5H_3D_2$. Thus, our results appear to support the theory in this respect. Very small peaks also appear at m/e 76 to 79 at 1200 K pyrolysis temperature representing production of partially deuterated $C_6H_{4\text{-}6}$ species whose analogs were also observed in the pyrolysis of the undeuterated sample.

Raising the pyrolysis temperature to 1220 K results in a small, proportional, increase in production of all of the pyrolysis products observed at 1200 K. The m/e 128 and 130 parent peaks decrease in intensity by about 15% with a concomitant increase in the intensity of the m/e 93 peak. One new peak is observed at m/e 41 potentially corresponding to C_3H_5, C_3H_3D or C_3HD_2. C_3H_5 does not appear in the pyrolysis of $C_6H_5CH_2Cl$ so it can be ruled out, but the latter two species may both contribute to the m/e 41 peak.

Mass spectra for the pyrolysis of $C_6H_5CD_2Cl$ seeded in He in the temperature range 1250 K to 1480 K can be seen in Figures 3.7 and 3.8. Figure 3.8 contains an

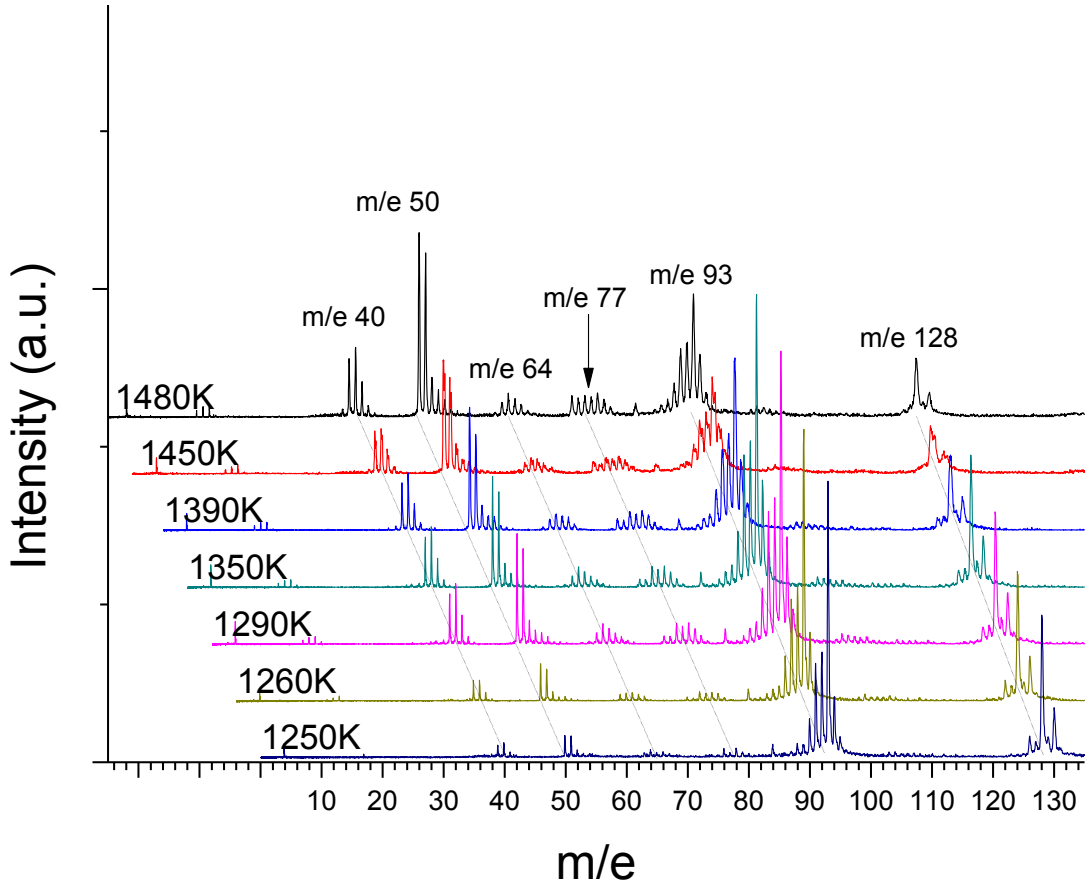

Figure 3.7 Stack plot of mass spectra for pyrolysis of $C_6H_5CD_2Cl$ (~1%) in He at pyrolysis temperatures 1250 K to 1480 K. Mass spectra are offset for clarity.

enlarged view depicting mass spectra in the mass regions m/e 12 to m/e 20 and m/e 37 to m/e 92. At 1250 K and 1260 K, all of the prior product peaks increase slightly in intensity. The peaks that are most obviously different from the $C_6H_5CH_2Cl$ pyrolysis

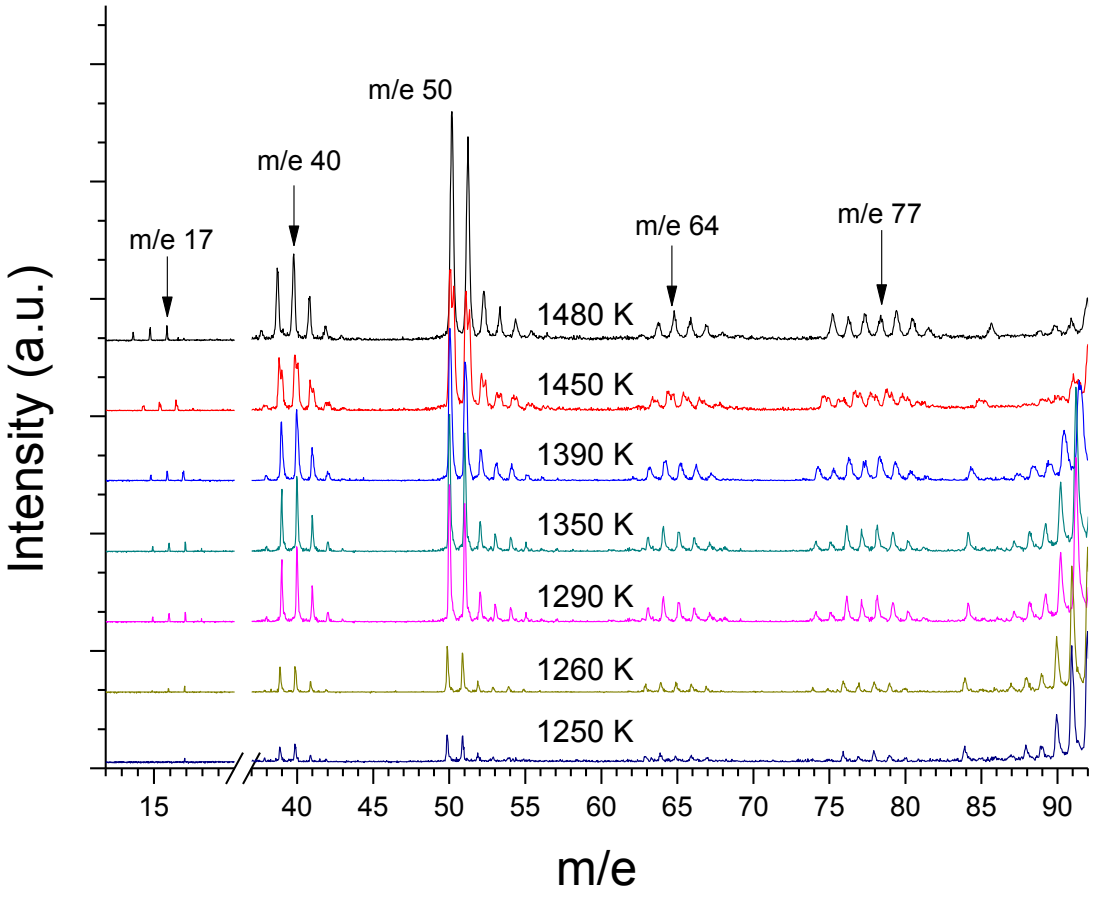

Figure 3.8 Stack plot of mass spectra for pyrolysis of $C_6H_5CD_2Cl$ (~1%) in He at room temperature and pyrolysis temperatures 1250 K to 1480 K enlarged to show mass region m/e 12 to m/e 20 and m/e 37 to m/e 92.

spectra are the m/e 40 and m/e 51 peaks. Although, they are very small peaks in the $C_6H_5CH_2Cl$ spectra, these peaks have intensities that are comparable to m/e 39 and m/e 50, respectively in the $C_6H_5CD_2Cl$ spectra. For the m/e 40 peak, this indicates a significant production of C_3H_2D rather than C_3H_4 since the C_3H_4 production was minimal in the pyrolysis of the undeuterated sample. By the same reasoning, m/e 51 represents primarily C_4HD in the pyrolysis spectra of $C_6H_5CD_2Cl$ with minimal production of C_4H_3. At 1260 K, very small peaks at m/e 41 and m/e 52 appear, representing the production of C_3H_3D and C_4H_2D, respectively.

Peaks at m/e 63 to 67 continue to grow as the pyrolysis temperature is raised from 1220 K up through 1290K, though to a lesser extent than the 3 carbon and 4 carbon containing fragments. In the pyrolysis spectra of $C_6H_5CH_2Cl$, the m/e 63 peak corresponding to C_5H_3 has approximately twice the intensity of the m/e 64 peak. The opposite is observed in the $C_6H_5CD_2Cl$ pyrolysis spectra indicating a large contribution of C_5H_2D to the intensity of the m/e 64 peak and C_5H_3D to m/e 65. The extent of the contribution of C_5H_4D and $C_5H_2D_2$ to the intensity of the m/e 66 peak intensity is not immediately clear, however the very small m/e 67 peak is likely due solely to $C_5H_3D_2$ production as a C_5H_6 analog at m/e 66 does not appear in the pyrolysis of the undeuterated sample in this temperature region.

Peaks at m/e 74 to 80 exhibit similar intensities to those in the m/e 63 to m/e 67 mass region as the pyrolysis temperature increases from 1220K through 1290K. These peaks are analogous to the m/e 74 to m/e 78 peaks seen in the pyrolysis of the

undeuterated sample seeded in He corresponding to C_6H_{2-6}. Because there are a multitude of peaks, the extent of deuteration is difficult to state with certainty, but several observations can be made. The lowest mass peak in the set, in both the pyrolysis of the deuterated and the undeuterated samples, is m/e 74 so this peak can be attributed to C_6H_2. The m/e 75 peak is slightly more prominent in the $C_6H_5CD_2Cl$ pyrolysis but only by about 20% indicating that it is primarily due to C_6H_3. The biggest difference in the two spectra is the m/e 76, C_6H_4 peak, which is the prominent peak in the set at 1300 K in the pyrolysis of $C_6H_5CH_2Cl$, but is only about 10% larger than m/e 77 in the pyrolysis of $C_6H_5CD_2Cl$ at 1290 K. This indicates significant production of C_6H_4D relative to C_6H_4. The largest mass peak in the pyrolysis of $C_6H_5CH_2Cl$ is at m/e 78. In the pyrolysis of $C_6H_5CD_2Cl$, peaks are observed at m/e 78, 79, and 80, suggesting significant deuteration of C_6H_6. The small m/e 80 peak corresponds to $C_6H_4D_2$. This is analogous to C_6H_6 in the undeuterated benzyl chloride spectra but the m/e 80 peak in the $C_6H_5CD_2Cl$ spectra is small compared to the mass 78 and 79 peaks suggesting a loss of D atoms from the side chain is important in its formation. The formation of all of the species in this set arises due to the loss of fragments containing one carbon atom from benzyl. Peaks appear at m/e 17, 16, and 15 indicating CHD_2, CH_2D, and CH_3, respectively, CHD_2 being the dominant product of this process.

Intensities of all product peaks continue to increase at 1290 K up through 1480 K. At higher temperatures, m/e 39, 40, 50, and 51 dominate in a fashion directly analogous to the benzyl chloride pyrolysis again highlighting the importance of reaction 3.4 or other secondary processes at higher temperatures. Several new peaks appear at the highest

temperatures including m/e 41, 42, 53, and 54. These peaks do not appear in the $C_6H_5CH_2Cl$ spectra and are, thus, deuterated analogs of the C_3H_4 and C_4H_4.

Pyrolysis of $C_6H_5CD_2Cl$ seeded in Ar was also performed to investigate pyrolysis of $C_6H_5CD_2Cl$ under a slightly longer time scale. Results of the pyrolysis of $C_6H_5CD_2Cl$ seeded in Ar are shown in Figures 3.9 and 3.10. As with the He spectra, a small amount of contamination from prior C_4H_4S pyrolysis remained but did not appear to obscure any important results. A room temperature spectrum and pyrolysis spectra at 970 K to 1290 K appear in Figure 3.9. The results are essentially identical to those for the He spectra at the lower temperatures although the S/N ratio is slightly less favorable. Production of benzyl, $C_6H_5CD_2^{\bullet}$, is observed at 1050 K. Between 1110 K and 1180 K, loss of H and D atoms is observed indicated by growth of peaks at m/e 91 and m/e 92. At 1240 K, peaks at m/e 50 and 51, m/e 63 to 67, and m/e 76 to 80 begin to appear while peaks at m/e 91 and 92 continue to grow in intensity. Presumably, C_3H_3 production is also occurring, as it did in the pyrolysis of $C_6H_5CD_2Cl$ seeded in He. Unfortunately, the m/e 39 peak is obscured by the broad m/e 40 peak caused by EI of Ar. Doubly ionized Ar can also be seen as a very small peak at m/e 20 at all temperatures. All of the aforementioned product peaks continue to grow form 1240 K to 1290 K while the parent m/e 128/130 peaks gradually decrease in intensity indicating the decomposition of $C_6H_5CD_2Cl$.

Pyrolysis mass spectra of $C_6H_5CD_2Cl$ seeded in Ar from temperatures 1320 K to 1420 K are shown in Figure 3.10. Results, again, are very similar to those in the He spectra. At 1320 K, product peaks continue to grow. A peak appears at m/e 90 indicating

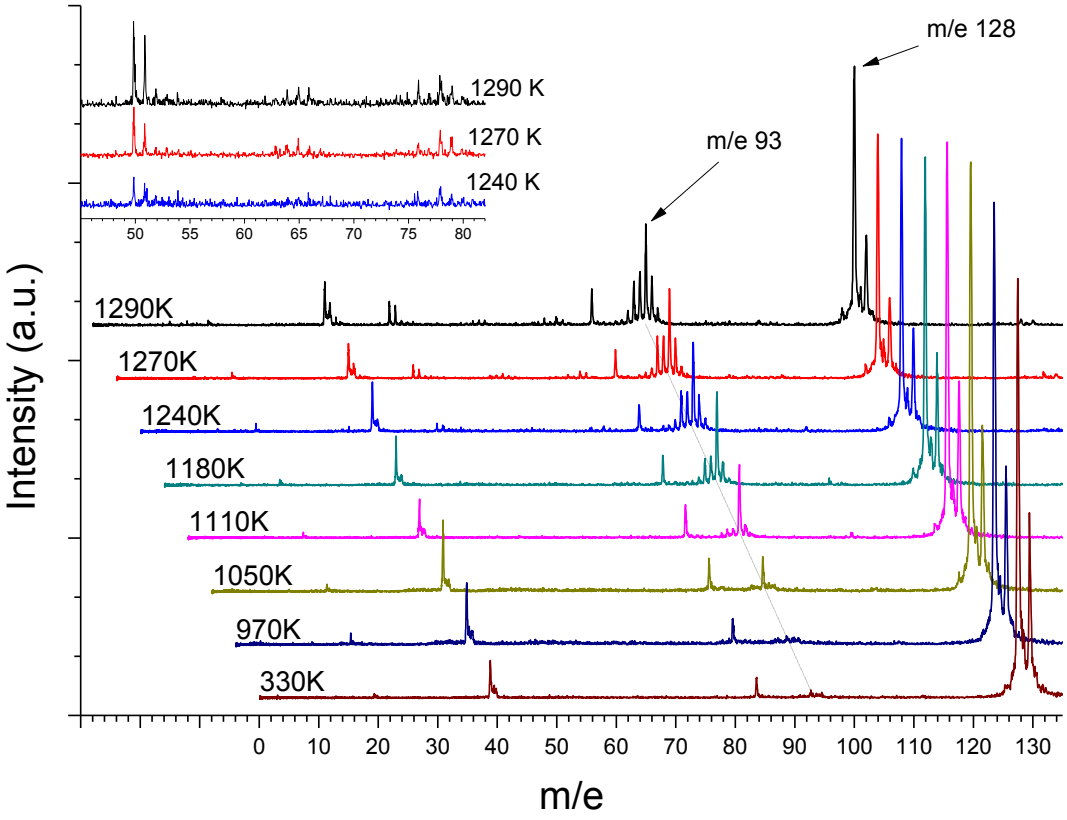

Figure 3.9 Stack plot of mass spectra for pyrolysis of $C_6H_5CD_2Cl$ (~1%) in Ar at temperatures 330 K to 1290 K. Mass spectra are offset for clarity. Inset shows an enlarged view of mass regions m/e 45 to m/e 82 at pyrolysis temperatures 1240 K, 1270 K, and 1290 K.

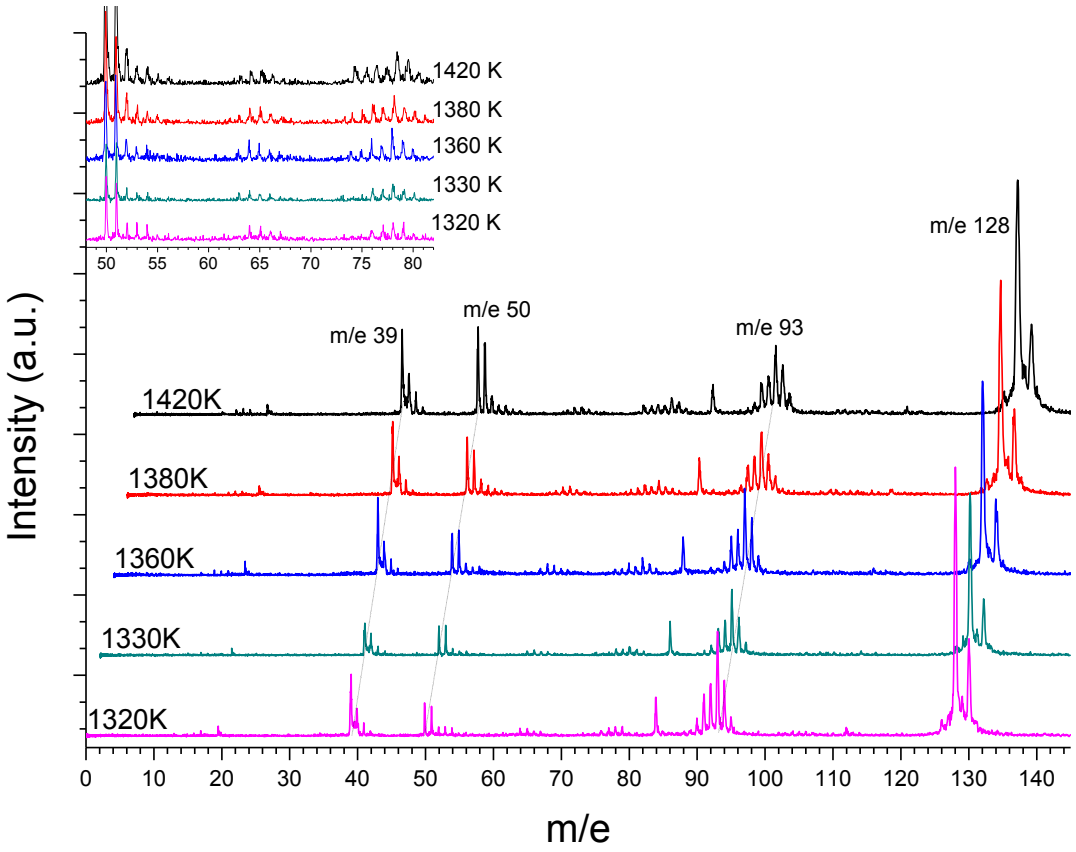

Figure 3.10 Stack plot of mass spectra for pyrolysis of $C_6H_5CD_2Cl$ (~1%) in Ar at temperatures 1320 K to 1420 K. Mass spectra are offset for clarity. Inset shows an enlarged view of mass region m/e 48 to m/e 82 at pyrolysis temperatures 1320 K, 1330 K, 1360 K, 1380 K, and 1420 K.

loss of 3H atoms or 1H atom and 1 D atoms from benzyl. Product peaks continue to grow as the pyrolysis temperature is raised to 1380 K while m/e 93 gradually decreases in intensity. At this temperature the m/e 39 and 40 peaks are clearly visible despite being partially obscured by the Ar peak. Peaks also appear at m/e 41, 52, 53, 54, 74, and 75 as they did in the He spectra. One noticeable difference between the He and Ar $C_6H_5CD_2Cl$ spectra is the prominence of the m/e 78 peak at the highest temperatures. A similar effect was also observed in the pyrolysis of $C_6H_5CH_2Cl$ and is further evidence of the formation of benzene as a result of secondary reactions due to the longer pyrolysis time scale in Ar.

(c) Benzyl Chloride – d_5, $C_6D_5CH_2Cl$

Pyrolysis of another deuterated form of benzyl chloride, $C_6D_5CH_2Cl$, was also performed to gain greater insight into the details of the benzyl chloride pyrolysis mechanism. The results of the pyrolysis of $C_6D_5CH_2Cl$ seeded in He are shown in Figure 3.11. Small peaks are observed at m/e 112/114. These peaks are due to a small amount of chlorobenzene contamination from a prior experiment. In the room temperature spectrum, large peaks are observed at m/e 131 and 133 due to the parent, $C_6D_5CH_2Cl$. Photoionization fragmentation of $C_6D_5CH_2Cl$, is also observed, the peak at m/e 96 representing $C_6D_5CH_2^{\bullet+}$. This is expected due to the modest appearance energy of benzyl from benzyl chloride. The m/e 96 peak maintains a consistent intensity as the nozzle temperature is raised to 1100K, however, based on the fact that the m/e 131/133 undergo small decreases in intensity, and that thermal production of benzyl from benzyl chloride

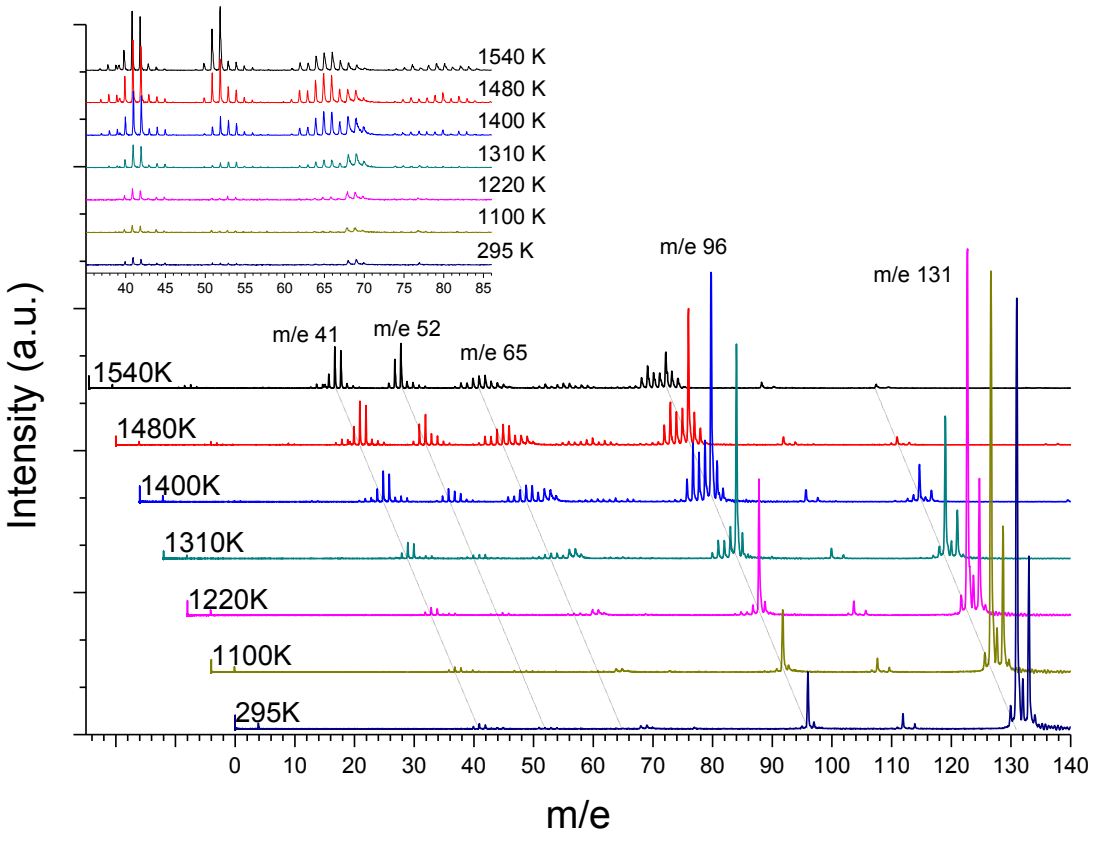

Figure 3.11 Stack plot of mass spectra for pyrolysis of $C_6D_5CH_2Cl$ (~1%) in He at room temperature and temperatures 1100 K to 1540 K. Mass spectra are offset for clarity. Inset shows an enlarged view of mass region m/e 35 to m/e 86.

was observed in prior pyrolysis spectra, we can conclude that the photoionization fragmentation contribution to the peak intensity is decreasing as thermal decomposition $C_6D_5CH_2Cl$ to $C_6D_5CH_2^{\bullet}$ is becoming dominant.

Further $C_6D_5CH_2^{\bullet}$ production is observed as the pyrolysis temperature is raised to 1220K, exhibited by the small decrease in m/e 131/133 peak intensities and the simultaneous increase in the intensity of m/e 96. Loss of H atom from benzyl is also observed as indicated by a small m/e 95 peak providing evidence that a majority of the H atoms lost by benzyl at the early stages of pyrolysis come from the side chain and not from the ring. As noted for $C_6H_5CH_2Cl$ and $C_6H_5CD_2Cl$ pyrolysis, HCl elimination could also occur but would require 1,1-HCl elimination and result in the formation of a carbene and is, thus, not likely. Small peaks can also be seen at m/e 41 and 42. These represent deuterated analogs of the m/e 39, C_3H_3, and m/e 40, C_3H_2D, peaks observed at the same temperature in the $C_6H_5CD_2Cl$ spectra. Thus, the most likely assignments for m/e 41 and 42 are C_3D_2H and C_3D_3, respectively. Very small peaks are also observed at m/e 68 and 69. Possible assignments for the m/e 69 peak include C_5HD_4 and $C_5H_3D_3$. No C_5H_6 species are observed at any temperature in the pyrolysis of $C_6H_5CH_2Cl$ so m/e 69 can be confidently assigned as C_5HD_4. Given the assignment of m/e 69, m/e 68 is most likely due to C_5D_4 rather than $C_5H_2D_3$. This assignment is further supported by the prominence of the m/e 64, C_4H_4 peak in the $C_6H_5CD_2Cl$ pyrolysis spectra. Nevertheless, there is likely to be some contribution from $C_5H_2D_3$ to the m/e 68 peak as a small m/e 67, $C_5H_3D_2$, is observed for $C_6H_5CD_2Cl$ pyrolysis.

At 1310 K, benzyl production increases significantly with the m/e 96 peak doubling in intensity with a concomitant 50% decrease in the intensity of m/e 131/133. The size of the m/e 95 peak increases in intensity by about 5 times indicating significant loss of H atom from the side chain of the ring-deuterated benzyl radical. Peaks also appear at m/e 93 and 94 both having an intensity approximately half that of the m/e 95 peak. The peak at m/e 94 is due to the loss of either 2 H atoms or one D atom from benzyl forming C_7D_5 and $C_7D_4H_2$ respectively and, given the mixture of products of the $C_6H_5CH_2Cl$ and $C_6H_5CD_2Cl$, there is likely a mixture of both products.

The production of C_3D_2H, C_3D_3, C_5D_4, C_5HD_4 all increase significantly upon an increase in temperature from 1220 K to 1310 K, indicated by the approximate doubling of intensity of peaks at m/e 41, 42, 68, and 69. A small peak also appears at m/e 40 corresponding to C_3D_2. A series of peaks also can be seen from m/e 62 to 67, perhaps due to the loss of D atoms from C_5D_4 and C_5HD_4 or other secondary decomposition processes. Very small peaks are also observed in the mass range m/e 51 to m/e 54 corresponding to C_4HD, C_4D_2, C_4HD_2, and $C_4D_3/C_4H_2D_2$, respectively.

At 1400 K to 1540 K, all of the aforementioned product peaks increase significantly in intensity. In addition small peaks at m/e 43, 44, and 45 rise above the baseline due to C_3HD_3, C_3D_4, and C_3HD_4, respectively. The peak at m/e 93 rises sharply indicating significant loss of HD from benzyl. The m/e 92 peak also rises quite significantly, likely due to $C_7D_3H_2$ production as the loss of 3 H atoms is not significant in the pyrolysis of the undeuterated sample. C_3D_2H and C_3D_3 are the dominant products

among those containing 3 carbon atoms with the m/e 41 and 42 peaks significantly increasing in intensity. Among the 4 carbon atom products, C_4HD and C_4D_2 are produced in the highest quantities as shown by the relatively large m/e 51 and 52 peaks that appear with an intensity ratio of approximately 2 to 3. Peaks also grow in the broad mass range m/e 62 to 70 representing highly deuterated analogs of the $C_5H_{2\text{-}5}$ species observed in the pyrolysis of the undeuterated sample, with m/e 62 being C_5H_2 and m/e 70 being C_5D_5. At 1480 K, very small peaks in the mass range m/e 75 to 83 can be seen, with m/e 75 corresponding to C_6HD, m/e 83 corresponding to C_6HD_5, and all others being heavily deuterated forms of $C_6H_{2\text{-}6}$ also observed in the pyrolysis of $C_6H_5CH_2Cl$.

Pyrolysis mass spectra for $C_6D_5CH_2Cl$ seeded in Ar are shown in Figure 3.12. Results of the pyrolysis are nearly identical to those for the He entrained $C_6D_5CH_2Cl$ sample with a slightly reduced S/N ratio and a few small differences at the highest temperatures. Photoionization fragmentation of the parent $C_6D_5CH_2Cl$, to form benzyl at room temperature is again observed. Thermal decomposition of $C_6D_5CH_2Cl$ to benzyl begins at 1090K and rapidly increases as the pyrolysis temperature is raised. At 1220 K, a small peak at m/e 95 indicates loss of H atom. At 1320 K, peaks appear at m/e 41, 42, 68, 69, 93, and 94 just as they did at 1310 K in the He spectra. A 1400 K and 1480 K, peaks are observed in the m/e 41 to 45, m/e 51 to 55, m/e 62 to 70, m/e 75 to 83, and m/e 92 to 96 mass regions with profiles nearly identical to those in the He spectra. One exception is the m/e 52, C_4D_2, peak which is approximately 15% grater in intensity relative to the m/e 51 peak in the Ar spectrum relative to the He spectrum. The increase of time scale from

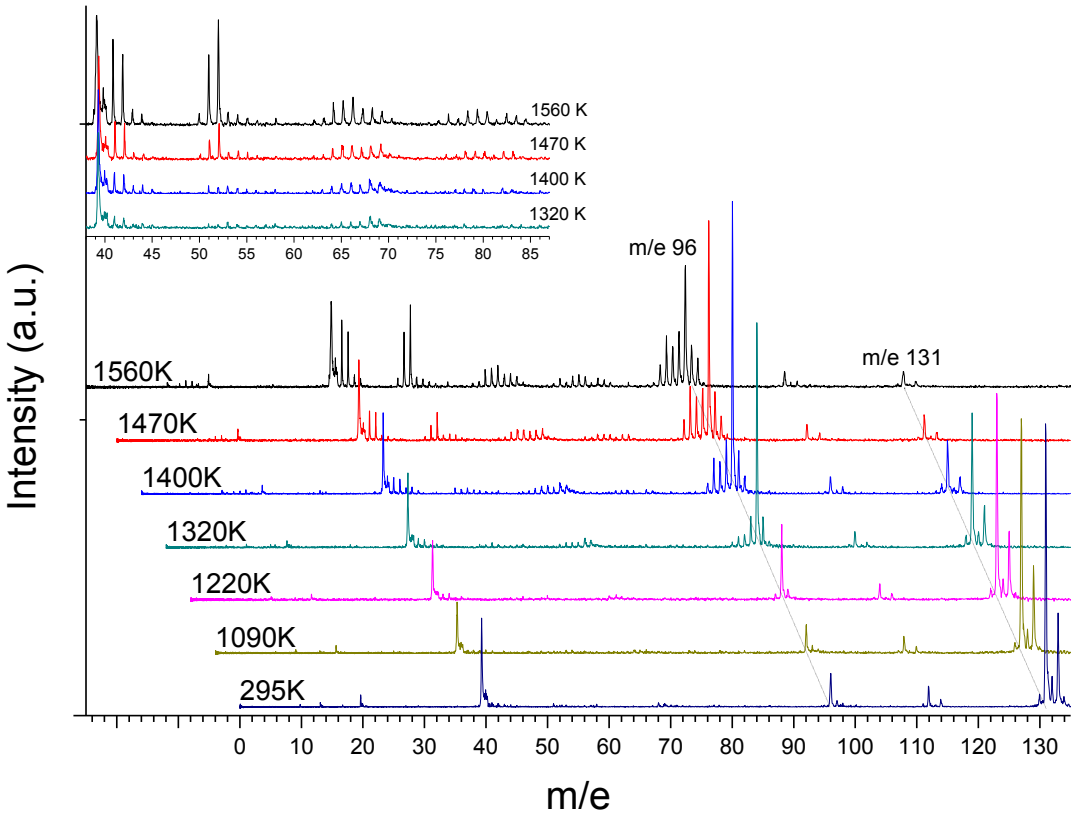

Figure 3.12 Stack plot of mass spectra for pyrolysis of $C_6D_5CH_2Cl$ (~1%) in Ar at room temperature and temperatures 1090 K to 1560 K. Mass spectra are offset for clarity. Inset shows and enlarged view of mass region m/e 38 to m/e 87 at pyrolysis temperatures 1320 K, 1400 K, 1470 K, and 1560 K.

~20μs to ~60μs does not appear to affect the results of the pyrolysis significantly except in the case of benzene production by secondary reactions as previously mentioned.

(d) Benzyl Bromide, $C_6H_5CH_2Br$

Benzyl bromide was also used as a potential source of benzyl radicals. The C-Br bond is weaker than that of C-Cl so it can make a potentially better source for benzyl radicals due to more facile homolytic bond cleavage of the C-Br bond. However, benzyl bromide also has a significantly lower vapor pressure than that of benzyl chloride. That property makes it difficult to get detectable concentration of benzyl bromide pyrolysis products. Mass spectra of the high temperature pyrolysis of benzyl bromide, $C_6H_5CH_2Br$ seeded in argon are shown in Figure 3.13. Peaks at 170 and 172 are due to the benzyl bromide parent and appear as a doublet with similar intensities due to the approximately 1 to 1 natural abundance of ^{79}Br to ^{81}Br. The m/e 91, benzyl, peak is prominent with a shoulder m/e 92 peak due to ^{13}C isotopes among the carbon atoms in the molecule. At 1180 K, C_5H_5 production is observed indicated by a small m/e 65 peak. At 1290 K, loss of one and two H atoms from benzyl occurs with peaks at m/e 89 and 90 corresponding to, C_7H_5 and C_7H_6, respectively. The intensity of the m/e 65 peak increases, indicating further production of C_5H_5. Small peaks at m/e 62, 63, and 64 are also observed suggesting secondary decomposition processes or loss of H from C_5H_5. The most prominent peak at 1290 K, is m/e 50 corresponding to C_4H_2. Small m/e 51 and 52 peaks

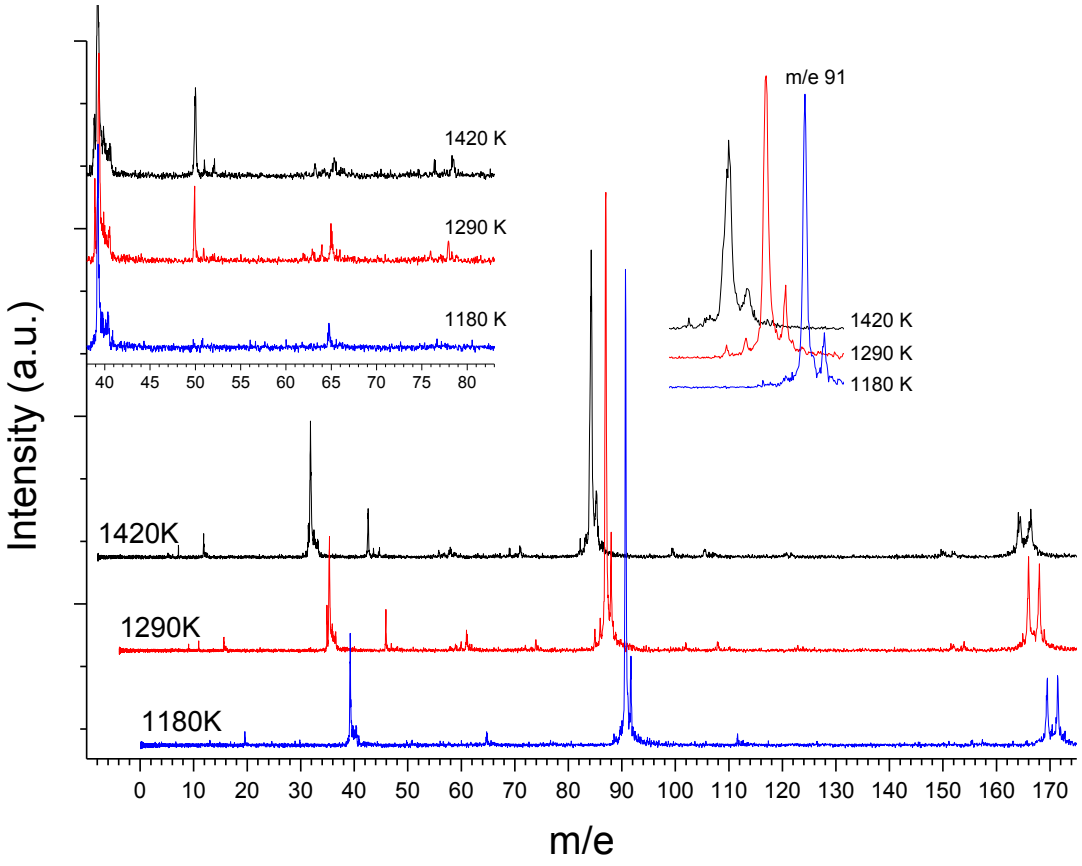

Figure 3.13 Stack plot of mass spectra for pyrolysis of $C_6H_5CH_2Br$ (~0.25%) in Ar at room temperature and temperatures 1180 K, 1290 K, and 1420 K. Mass spectra are offset for clarity. Left inset shows an enlarged view of spectra in the mass region m/e 38 to m/e 84. Right inset shows an enlarged view of peaks at m/e 89 to m/e 92.

can also be seen at 1290 K and 1420 K corresponding to C_4H_3 and C_4H_4. Minor production of benzene is seen as it was in prior spectra as evidenced by the m/e 78 peak.

3.4 Discussion

(a) C_7H_7 decomposition to C_7H_6 and H atom

Pyrolysis mass spectra taken in this set of experiments provide direct observations of several pyrolysis pathways for the benzyl radical. In all of the pyrolysis experiments, loss of H atoms (labeled reaction 3.2) from benzyl radical to produce C_7H_6 and H atoms is clearly observed to be the dominant thermal decomposition pathway at the lowest temperatures that benzyl pyrolysis is observed, approximately 1100 to 1200 K.

$$C_6H_5CH_2^{\bullet} \rightarrow C_7H_6 + H^{\bullet} \qquad (3.2)$$

This is in agreement with recent theoretical data from the Cavalotti group[9], da Silva et. al[10], and recent photolysis experiments from our group.[6] The structure of the C_7H_6 species and the mechanism of reaction 3.2 is still uncertain although, theoretical studies by Cavalotti et al. and da Silva et. al suggest formation of fullvenallene to be the lowest energy pathway with an energy barrier of about 82 kcal mol^{-1}.

Given the agreement of the most theoretical studies, the photolysis experiments from our group, and these pyrolysis results, dissociation of benzyl radical to lose an H atom and form C_7H_6, presumably in the form of fulvenallene, is well supported, but the

mechanism for the formation of C_7H_6 from benzyl and the identity of the product as fullvenallene, are still not certain. The ability to determine location of the H atom lost, either on the benzene ring or on the CH_2 side chain could give significant insight into the mechanism of C_7H_6 formation from benzyl decomposition. Comparison of the thermal decomposition of deuterated benzyl chlorides, $C_6D_5CH_2Cl$ and $C_6H_5CD_2Cl$, to that of the undeuterated sample can provide some insight into the nature of mechanism of benzyl decomposition to fulvenallene or another potential species.

Several simple models for the H-atom dissociation from benzyl radical can be considered. These include (i) loss of H atom from benzyl ring from which 5 potential H atoms could be lost, (ii) loss of H atom from the benzyl side-chain of which there are 2, and (iii) statistical loss of H atoms from the ring and side-chain due to extensive isomerization prior to dissociation. The statistical analysis of these potential H-atom dissociation channels for the pyrolysis of $C_6H_5CD_2^{\bullet}$ and $C_6D_5CH_2^{\bullet}$ (from $C_6H_5CD_2Cl$ and $C_6D_5CH_2Cl$, respectively) is summarized in Table 3.1.

In the pyrolysis mass spectra, loss of H atom from benzyl first appears at approximately 1100 K and continues with subsequent loss of H atom at higher temperatures. For the deuterated samples, either H or D atom could be the first one lost. Figure 3.14 features a comparison of the ratio of peak intensities for peaks corresponding products with mass to 1 amu less than undeuterated or partially deuterated benzyl radical to those corresponding products with mass 2 amu less than undeuterated or partially deuterated benzyl radical as a function of temperature in K for benzyl chloride pyrolysis

experiments using He carrier gas. Particularly relevant are the lower temperature ranges where, as shown in the figure, loss of 1 H atom from undeuterated benzyl chloride (denoted as Benzyl D-0) is dominant with 5 times the production of C_7H_6 relative to C_7H_5 at 1100 K. Even up to 1200K, secondary loss of a second H atom and/or H_2 loss from C_7H_7 only occurs to a relatively modest extent. Thus, for the deuterated samples, in the 1100K to 1200K temperature region, the peak intensity ratios shown in Figure 3.14 represent primarily ratios of the loss of H atom versus D atom for each species, with limited contribution from processes involving the loss of 2 H or D atoms.

	H/D Branching Ratios		
Sample	(i) Ring model	(ii) Side-chain model	(iii) Statistical Model
$C_6H_5CD_2$	5 : 0	0 : 2	2.5 : 1
$C_6D_5CH_2$	0 : 5	2 : 0	0.4 : 1

Table 3.1 Statistical analysis of expected H/D atom product ratios from the pyrolysis of $C_6H_5CD_2$ and $C_6D_5CH_2$ assuming three simple decomposition models, (i) loss of H/D atom from benzyl ring, (ii) loss of H/D atom from the benzyl side-chain, and (iii) statistical loss of H/D atoms from the ring and side-chain due to extensive isomerization prior to dissociation.

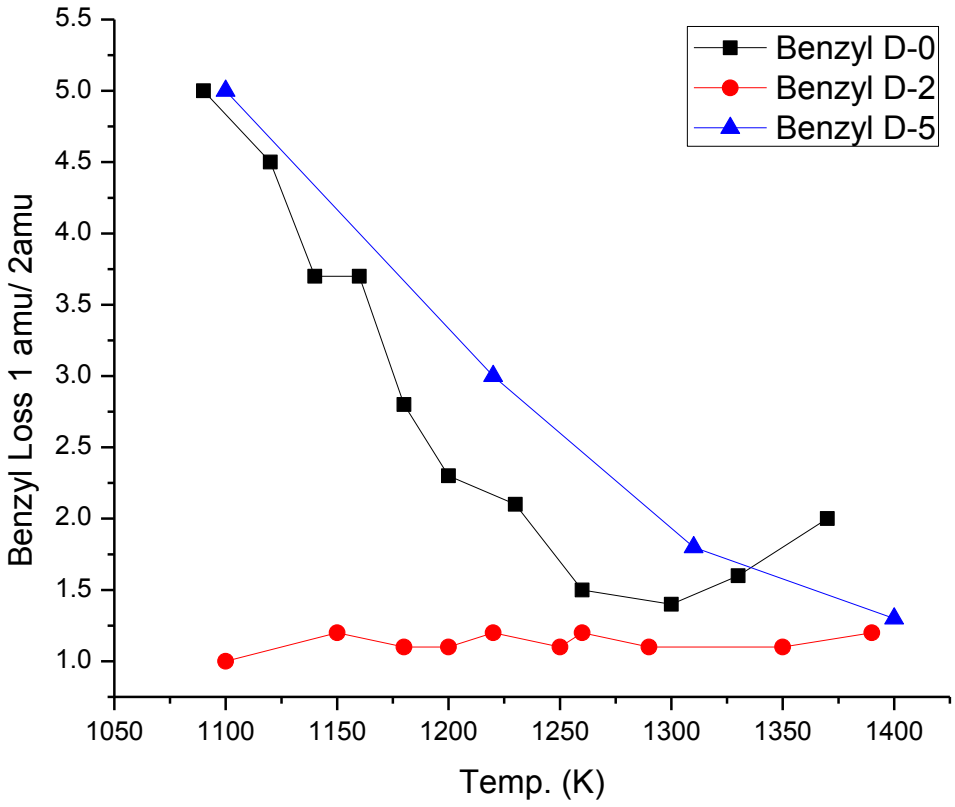

Figure 3.14 Ratio of peak intensities for peaks corresponding to products with mass 1 amu less than undeuterated or partially deuterated benzyl radical to those corresponding to products with mass 2 amu less than undeuterated or partially deuterated benzyl radical as a function of temperature in K for benzyl chloride pyrolysis experiments using He carrier gas. In the key, "Benzyl D-0" refers to $C_6H_5CH_2Cl$ pyrolysis, "Benzyl D-2" refers to $C_6H_5CD_2Cl$ pyrolysis, and "Benzyl D-5" refers to $C_6D_5CH_2Cl$ pyrolysis.

In the case of $C_6H_5CD_2Cl$ pyrolysis (denoted Benzyl D-2), the H/D loss ratio is approximately 1 to 1 indicating loss of D atom from the CD_2 side-chain occurs with approximately equivalent frequency relative to the loss of H atom form the ring despite the 2.5:1 statistical ratio of H:D atoms in the compound. For $C_6D_5CH_2Cl$ pyrolysis (denoted Benzyl D-5), loss of H atom dominates at lower temperatures and remains higher than the statistical 2 to 5 H/D ratio throughout the temperature range studied. Based on this evidence, loss of H atom from the benzyl side-chain is clearly an important path in benzyl thermal decomposition although loss of H from the ring also proceeds to a significant extent.

Notably, the most energetically favorable pathways determined by Cavalotti et al. and da Silva et al., involving decomposition to fullvenallene, require the loss of H from the ring and not from the side chain. Proposed pathways for decomposition of benzyl to fullvenallene are outlined in Scheme 3.1 where the side-chain H atoms are labeled as deuterium. Each of the three proposed pathways involves isomerization of benzyl to methylenebicyclo[3.1.0]hex-3-en-2-yl (MBH) and subsequent loss of an H atom that originated from the benzene ring. Thus, the proposed mechanism in Figure 3.1 and Scheme 3.1 is not consistent with the data in this study unless there is an intermediate isomerization step or series of steps to allow the side-chain H atoms to somehow be incorporated into the ring or lost in another way.

Isomerization to the bicyclic norcaradienyl radical (NCDE) and cycloheptatriene radical with subsequent loss of H atom as shown in Scheme 3.2 also were considered by

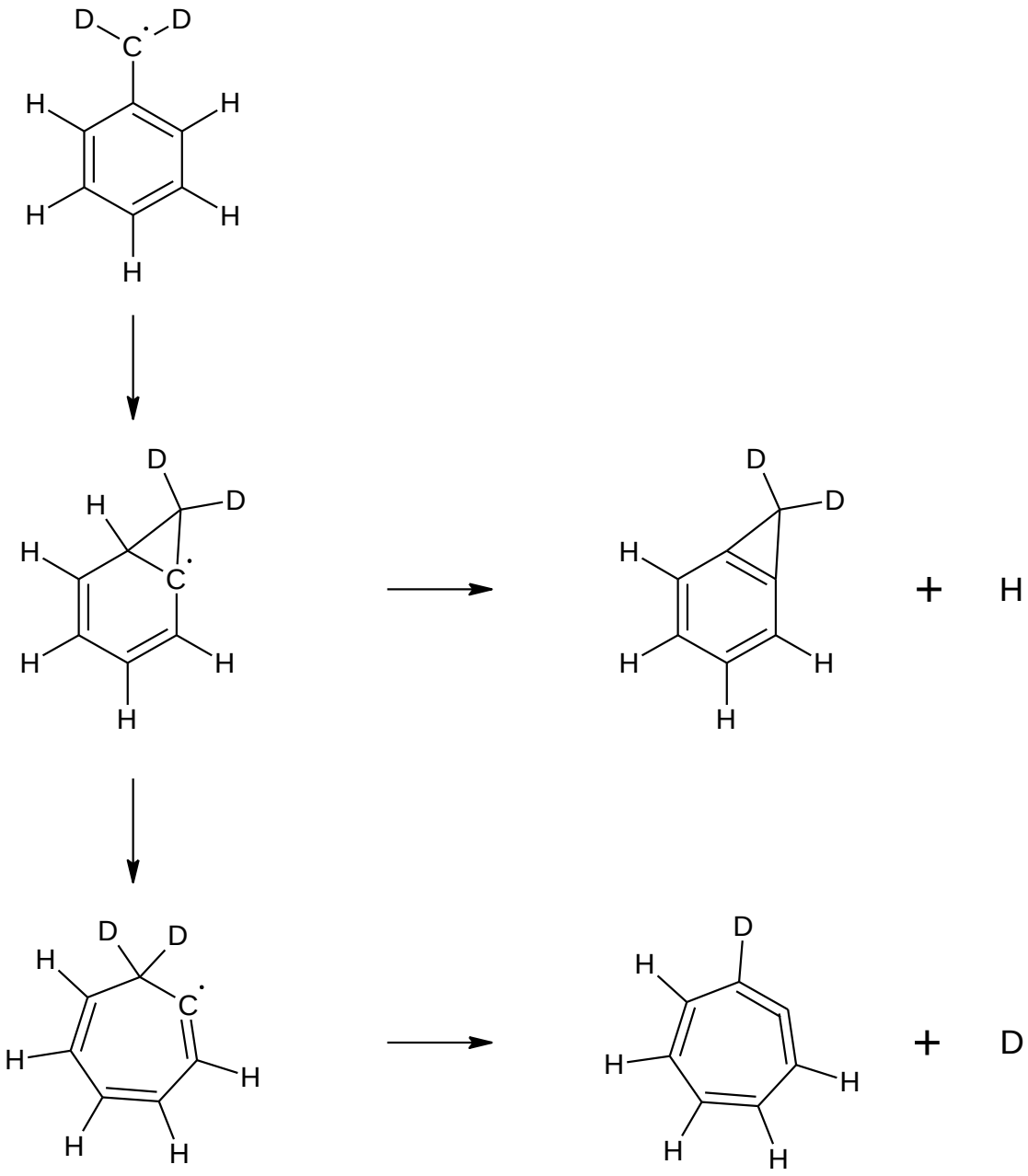

Scheme 3.2 Isomerization of partially deuterated benyzyl radical to norcaradienyl radical (NCDE) and cycloheptatriene radical with subsequent loss of H/D atom.

Cavalotti et al. and da Silva et al. as, less favorable higher energy pathways. Loss of H atom from NCDE is also expected to follow the ring model as seen by the loss of H atom rather than D from isomerized $C_6H_5CD_2^{\bullet}$ in Scheme 3.2. Isomerization to cycloheptatriene radical however is expected to result in the loss of an atom originally located on the side-chain to form 1,2,4,6- cycloheptatetraene as depicted by in Scheme 3.2 where D atom is ejected from isomerized $C_6H_5CD_2^{\bullet}$. Sivaramakrishnan et. al observed D atom formation during shock tube, ARAS studies of $C_6H_5CD_2Br$ as a minor fraction of approximately 0.2 and speculated that this occurred through the cycloheptatriene pathway. Further isomerization of cycloheptatriene with a potential return to a more isotopically scrambled, stable benzyl radical could also contribute to H/D ratios that are closer to those that would be expected by the fully statistical H loss model.

H/D product ratios for pyrolysis of deuterated benzyl chlorides in this experiment cannot be computed with absolute certainty due to the fact many mass peaks result from a combination of potential products with the same mass. However, fairly accurate estimates of different deuterium labeled products can be made by performing a deconvolution of peak intensities via comparison of products fractions in the pyrolysis of undeuterated benzyl chloride to those of its deuterated counterparts. Product fractions for benzyl pyrolysis products due to sequential loss of hydrogen atoms in the pyrolysis of $C_6H_5CH_2Cl$, $C_6H_5CD_2Cl$, and $C_6D_5CH_2Cl$ seeded in helium are listed in Tables 3.2, 3.3, and 3.4, respectively.

Temp (K)	C_7H_6	C_7H_5	C_7H_4	C_7H_3	C_7H_2
1090	0.83	0.17	0.00	0.00	0.00
1120	0.82	0.18	0.00	0.00	0.00
1140	0.71	0.19	0.10	0.00	0.00
1160	0.72	0.20	0.08	0.00	0.00
1180	0.67	0.23	0.10	0.00	0.00
1200	0.61	0.27	0.11	0.00	0.00
1230	0.62	0.29	0.07	0.02	0.00
1260	0.55	0.37	0.06	0.02	0.00
1300	0.55	0.38	0.05	0.01	0.00
1330	0.57	0.36	0.05	0.02	0.00
1370	0.60	0.30	0.08	0.02	0.00

Table 3.2 Product fractions for benzyl pyrolysis products due to loss of hydrogen atoms in the pyrolysis of $C_6H_5CH_2Cl$ seeded in helium.

At 1090 K to 1120 K, in the undeuterated sample, C_7H_6 and C_7H_5 are produced in fractions 0.82 to 0.83 and 0.17 to 0.18, respectively. No further loss of H atoms is observed at this modest temperature. For $C_6H_5CD_2Cl$ pyrolysis, the m/e 92 peak is due to loss of H from $C_6H_5CD_2^{\bullet}$, producing $C_7H_4D_2$, however the peak at m/e 91 may be due to loss of one D or two H atoms, producing either C_7H_5D or $C_7H_3D_2$. Loss of fragments with mass greater than 2 mass units is not observed at this temperature so an upper bound contribution of 18% can be placed on the fraction contribution of $C_7H_3D_2$ to the intensity of the m/e 91 peak. Thus the total product fraction of $C_7H_3D_2$ is at most 18% of the 0.50 fraction attributed to m/e 91, or 0.09. By this approximation, product fractions of $C_7H_4D_2$,

Temp	$C_7H_4D_2$	C_7H_5D $C_7H_3D_2$	C_7H_4D $C_7H_2D_2$	C_7H_5 C_7H_3D C_7HD_2	C_7H_4 C_7H_2D
1100	0.50	0.50	0.00	0.00	0.00
1150	0.42	0.35	0.10	0.06	0.07
1180	0.42	0.38	0.10	0.05	0.06
1200	0.40	0.37	0.12	0.05	0.06
1220	0.41	0.35	0.13	0.06	0.06
1250	0.41	0.37	0.14	0.04	0.04
1260	0.40	0.35	0.15	0.05	0.04
1290	0.39	0.36	0.15	0.06	0.04
1350	0.40	0.36	0.15	0.06	0.04
1390	0.41	0.33	0.17	0.05	0.04

Table 3.3 Product fractions for benzyl pyrolysis products due to loss of hydrogen atoms in the pyrolysis of $C_6H_5CD_2Cl$ seeded in helium.

Temp	C_7D_5H	$C_7D_4H_2$ C_7D_5	C_7D_4H	$C_7D_3H_2$ C_7D_4	C_7D_3H
1100	0.83	0.17	0.00	0.00	0.00
1220	0.56	0.19	0.17	0.09	0.00
1310	0.43	0.24	0.25	0.08	0.00
1400	0.32	0.25	0.30	0.12	0.01
1480	0.27	0.24	0.32	0.15	0.02

Table 3.4 Product fractions for benzyl pyrolysis products due to loss of hydrogen atoms in the pyrolysis of $C_6D_5CH_2Cl$ seeded in helium.

C_7H_5D, and $C_7H_3D_2$, are 0.50, 0.41, and 0.09, respectively indicating that D atom loss from the side-chain is a significant process. The same reasoning can be applied to the $C_6D_5CH_2Cl$ pyrolysis results at 1100 K yielding C_7D_5H, $C_7D_4H_2$, and C_7D_5 product fractions of 0.83, 0.14, and 0.03, respectively. Admittedly, S/N for m/e 95 and 94 peaks for this particular measurement was small so the side-chain effect appears to be exaggerated here, but loss of H atoms from the benzyl side-chain is clearly a significant process in benzyl pyrolysis.

The number of different possible product fragments produced upon sequential H/D loss or H_2/HD/D_2 elimination from the deuterated benzyl radicals increases significantly at higher temperatures complicating deconvolution attempts like the one just used, but several observations can be made that further support the prominence of side-chain H/D loss from benzyl. At 1180 K, C_7H_4 is produced in $C_6H_5CH_2Cl$ pyrolysis indicating loss of 3 H atoms from benzyl constituting 10% of the H loss products with no loss of 4 H atoms observed. Loss of 2 D atoms and 1 H atom in $C_6H_5CD_2Cl$ pyrolysis makes up a significant portion of the H/D loss products at 1180 K at 6% again implying the importance of loss of D from the side-chain. By contrast, loss of 2 D atoms and 1 H atom is hardly observed in $C_6D_5CH_2Cl$ pyrolysis, even at elevated temperatures, despite the statistically high presence of D atoms in the $C_6D_5CH_2Cl$ molecule.

It is also useful to compare the product ratios of the analogous m/e 91 and m/e 94 peaks in $C_6H_5CD_2Cl$ and $C_6D_5CH_2Cl$ pyrolysis, respectively, that indicate loss of D atom or 2H at higher temperatures. Loss of D atom does appear to be quite important in

$C_6H_5CD_2Cl$ pyrolysis with m/e 91 product fractions being 0.35 – 0.37 for $C_6H_5CD_2Cl$ pyrolysis versus 0.24 – 0.25 fractions for m/e 94 for $C_6D_5CH_2Cl$ pyrolysis, although loss of 2 H is much more probable statistically in $C_6H_5CD_2Cl$ than in $C_6D_5CH_2Cl$ which may account for a significant part of this difference.

In summary, loss of H from benzyl is the most significant benzyl thermal decomposition pathway but, neither the ring H loss model, nor the side-chain H loss model, nor the statistical H loss model can effectively describe the thermal decomposition of benzyl radical completely. Although theoretical support of benzyl decomposition to fulvenallene and H atom is strong, significant loss of side chain H atoms at a fraction somewhere between 0.4 and 0.7 observed in this experiment, is not consistent with direct decomposition of benzyl to fulvenallene and H atom. Loss of side-chain H atoms via isomerization to cycloheptatriene or another species with subsequent loss of H atom may be responsible for significant loss of side-chain H atoms. Extensive isomerization of benzyl prior to decomposition may also contribute to side-chain H atom loss.

(b) Other benzyl decomposition processes

Besides loss of H from benzyl, several other, previously mentioned potential decomposition pathways exist as listed below.

$$C_6H_5CH_2^{\bullet} \rightarrow C_6H_4 + CH_3^{\bullet} \qquad (3.3)$$

$$C_6H_5CH_2^{\bullet} \rightarrow C_5H_5^{\bullet} + C_2H_2 \quad (3.1)$$

$$C_6H_5CH_2^{\bullet} \rightarrow C_4H_4 + C_3H_3^{\bullet} \quad (3.4)$$

Reaction 3.1 has long been used to account for the production of ethylene in benzyl pyrolysis in kinetic models. This pathway has been supported as the main benzyl decomposition process by theoretical and experimental studies,[1,3,20] but recently has been regarded as secondary to reaction 3.2.[9,10,21,22] The $C_5H_5^{\bullet}$ species is fairly well established to be the resonance stabilized cyclopentadienyl radical. In this pyrolysis study, ethylene production cannot be monitored directly due to the high ionization potential of ethylene. However, cyclopentadienyl radical is easily monitored via the m/e 65, C_5H_5 peak in the mass spectra. Figures 3.3 and 3.4 clearly show that, although small amounts of cyclopentadienyl are produced at low temperatures 1180 K to 1230 K, reaction 3.2 proceeds much more quickly with sequential loss of H atoms proceeding at least an order of magnitude more quickly. High concentrations of C_5H_5 are never observed in benzyl flash pyrolysis even at the highest temperatures where the m/e 63, C_5H_3, peak has twice the intensity of m/e 65. C_5H_3 may be produced due to the secondary decomposition of C_5H_5 via the elimination of H_2, but given the abundance of other large fragments such at C_7H_5, production of C_5H_3 from larger fragments appears to be more likely.

Pathway 3.3, methyl loss from benzyl, although not considered significant historically, has received very recent support from kinetic simulations published by Derudi et al.[23] They propose decomposition of benzyl to form methyl radical and benzyne as a somewhat significant pathway relative to decomposition via reaction 3.2 to

fulvenallene and H atom and state rate constants k = (5.495 x10^{89} cm mol s K) ($T^{-20.82\ K}$) exp (-141.7 kcal mol^{-1}/RT) and k = (2.951 x10^{97} cm mol s K) ($T^{-22.95\ K}$) exp (-148.3 kcal mol^{-1}/RT), for each process, respectively with a branching ratio for benzyne and methyl stated as high as 49%. Decomposition via reaction 3.1 is excluded from their model which is in accordance with observations of limited C_5H_5 production in this pyrolysis study.

The Derudi et al. benzyne/ methyl decomposition model is supported by the results of this pyrolysis experiment, particularly at the higher temperature ranges, but production of benzyne and methyl is significantly less than predicted in their model. In the pyrolysis of $C_6H_5CH_2Cl$ seeded in He, a concomitant increase in intensity of m/e 15, methyl, and m/e 76, C_6H_4, is clearly observed and, at temperatures 1300 K and above, the intensity of the m/e 76 peak is over 3 times that of the m/e 55, C_5H_5 peak. The presumption of benzyne as the C_6H_4 moiety is supported by results for the pyrolysis of $C_6H_5CH_2Cl$ seeded in Ar. The longer reaction time afforded by Ar results in the secondary addition of H_2 to benzyne to produce highly resonantly stabilized benzene as indicated by the prevalence of m/e 78 in Figure 3.5 relative m/e 76. The branching ratio, however, for reaction 3.3 relative to reaction 3.2 is significantly lower than that predicted by the Derudi et al. theoretical model. C_7H_6 and C_7H_5 production together are greater than that for C_6H_4 by approximately at least 5 times. Derudi et al. predict significant decomposition of C_6H_4 to C_5H_3 and acetylene C_2H_2 which could account for its limited abundance under our pyrolysis conditions, but increased CH_3 production would be

expected if this were the case, and it is not observed. Instead, the contribution of reaction 3.2 to benzyl pyrolysis is appears to be roughly 10%.

Pathway 3.4 has also been proposed historically based on experimental studies by Smith[1] and theoretical studies by Jones[8], but has not received much recent attention. In this study, Reaction 3.4 would be indicated by simultaneous growth of m/e 39 and m/e 52 peaks indicating C_3H_3 and C_4H_4, respectively. Reaction 3.4 does not appear to proceed to any significant extent in this pyrolysis study. Although C_3H_3 production is prominent at temperatures above 1230 K, m/e 39 having very high intensity as the pyrolysis temperature increases, m/e 52 is never a dominant peak. The m/e 50 peak, indicating C_4H_2, does grow rapidly with temperature, being the largest peak at temperatures above 1300 K. C_4H_2 could arise from secondary elimination of H_2 from C_4H_4, however, it is more likely that C_4H_2 results from the decomposition of larger molecules such as C_7H_5, which is already present at much higher concentrations at 1200 K. Peaks at m/e 39, m/e 50, and m/e 52 are not significant until pyrolysis temperatures are increased above 1260 K so formation of C_3H_3 and C_4H_2 from C_7H_5 appears likely.

(c) Secondary decomposition of C_7H_6 to C_7H_5 and H

Significant loss of a second H atom from benzyl radical occurs extensively in this study even at modest pyrolysis temperatures of approximately 1200 K as clearly seen in Figures 3.2 and 3.3. Other benzyl decomposition pathways are relatively minor at these temperatures where C_7H_5 production dominates over production of all other product fragments by at least a factor of 3. The importance of C_7H_5 in combustion and soot

formation processes was first proposed by da Siva and Bozelli based on ab intio calculations published in 2009 where they identified the fulvenallenyl radical as having particularly strong resonance stabilization due to the presence of allenic (CH_2=C=C$^{\bullet}$H) and acetylenic (C$^{\bullet}H_2$─C≡CH) resonance forms combined with electron delocalization on the C_5 ring as in cyclopentadienyl radical as shown in Scheme 3.3.[24,25] They proposed the formation of fulvenallenyl by loss of hydrogen from fulvenallene or 1,3-ethynylcyclopentadiene favoring the more stable fulvenallene.

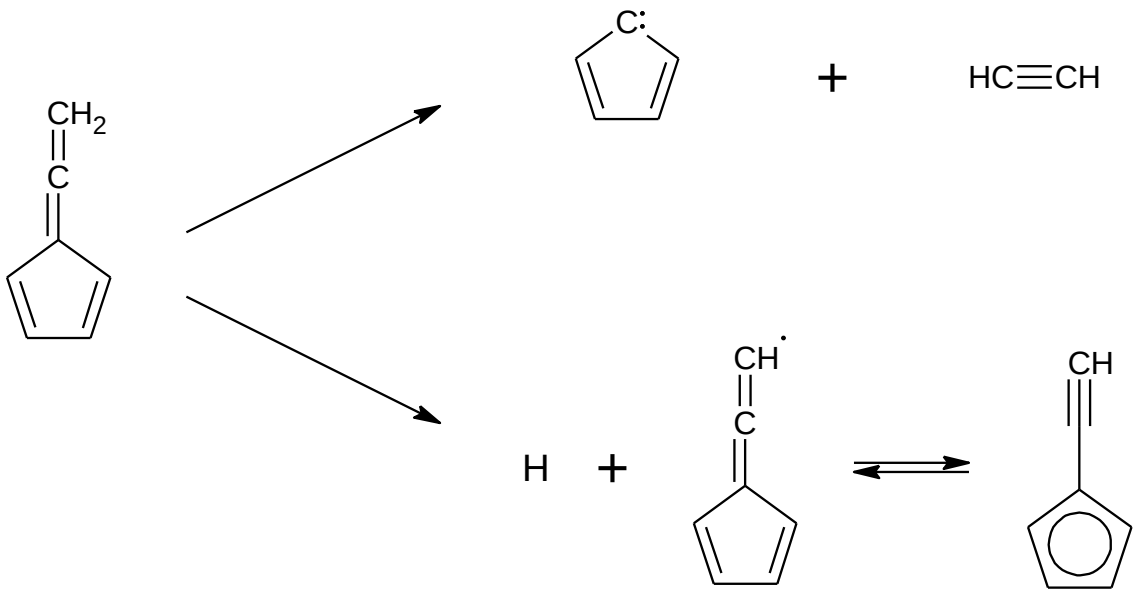

Scheme 3.3 Decomposition of fulvenallene to cyclopentadienylidene and acetylene or H atom and fulvenallenyl radical. Two resonance forms of fulvenallenyl radical are shown to emphasize resonance stability.

The Cavalotti group has also recently suspected the importance of secondary decomposition of C_7H_6 to C_7H_5 and H atom, and has released two companion theoretical studies investigating this process, one investigating the C_7H_6 potential energy surface[26], and one focusing on the decomposition of the fulvenallene C_7H_6 species specifically.[27] They concluded that the fastest decomposition channel for C_7H_6 species, particularly fulvenallene, was to C_5H_4, clyclopentadienylidene, and C_2H_2, acetylene, with the condition that this decomposition requires a spin forbidden intersystem crossing from the singlet to triplet state which could potentially slow this decomposition process considerably. They also identified decomposition to fulvenallenyl radical and H atom that, although slower than the clyclopentadienylidene/ acetylene channel by a factor of 2 to 3, has a lower activation energy of 82 kcal mol^{-1} versus 96 kcal mol^{-1} for clyclopentadienylidene/ acetylene and does not require an intersystem crossing.

The flash pyrolysis results in this study clearly show that H loss from C_7H_6 is the dominant C_7H_6 decomposition channel. Although acetylene cannot be monitored in this study due to its high IE, clyclopentadienylidene production can be determined by tracking the growth of the m/e 64 peak in the $C_6H_5CH_2Cl$ mass spectra. At low pyrolysis temperatures in the range of 1180 to 1230 K m/e 64 is not observed at all while m/e 89 corresponding to C_7H_5, is the second largest product peak next to m/e 90, C_7H_6. The peak at m/e 64 appears at temperatures 1260 K and above but only after m/e 63, indicating C_5H_3 production, becomes significant. The peak at m/e 64 at high temperatures may be due to direct decomposition of C_7H_6 but is likely also partly due to secondary H abstraction by C_5H_3. In addition, m/e 64 is significantly lower in intensity than m/e 89 in

the temperature range 1260 to 1420 K by at least a factor of 5. Subsequent decomposition of C_7H_5 to smaller fragments such at C_7H_4, C_3H_3, and C_4H_2 also appears likely. Therefore, decomposition of C_7H_6 to C_5H_4 and C_2H_2 appears to be insignificant relative to loss of H atom forming C_7H_5.

The process $C_7H_7 \rightarrow C_7H_6 + H \rightarrow C_7H_5 + 2\ H$ appears to be dominant in our observations which indicates significant production of H atom. This is at odds with a shock tube H atom ARAS study published recently in 2011 by Sivaramakrishnan et al.[21] who observed production of only 0.8 H atoms per benzyl molecule upon benzyl decomposition which is significantly less than what is observed in this pyrolysis study. Derudi et al.[23] invoked the benzyne/ methyl decomposition pathway (reaction 3.3) to account for the difference in H atom production, but reaction 3.3 does not appear to be as significant as would be required to account for the difference. Further investigation may be required to resolve this discrepancy.

(d) Further decomposition of C_7H_5

Due to its high resonance stability, C_7H_5, in the form of fulvenallenyl radical has recently been suspected to be present in significant concentrations in toluene and benzyl decomposition as well as other combustion processes. It has also been implicated as a potentially significant reactant in the formation of polyaromatic hydrocarbons and soot in combustion. Data from this pyrolysis study confirm the importance of C_7H_5 as an product of benzyl decomposition, particularly at the onset of pyrolysis at low temperatures 1100

K to 1200 K where it is second in concentration only to C_7H_6 from which it is almost certainly produced by loss of H atom.

The potential energy surface of C_7H_5 was recently investigated theoretically by da Silva and Trevitt who analyzed 22 potential C_7H_5 structures and found the fulvenallenyl radical to be the most thermodynamically stable with a calculated ΔH_f of 115.7 kcal mol^{-1}.[28] This was somewhat expected due to its previously mentioned high resonance stabilization. Three other resonantly stabilized structures were found to have enthalpies of formation 15 to 25 kcal mol^{-1} larger than that of fulvenallenyl and all others were significantly less stable. For these reasons, the C_7H_5 product observed in this pyrolysis study is expected to be fulvenallenyl radical.

Inspired by the work of da Silva and Trevitt, Derudi et al. performed ab initio and RRKM calculations to analyze the decomposition kinetics of fulvenallenyl radical.[23] They predicted the following decomposition pathways each having comparable energetics and kinetics.

$$C_7H_5^{\bullet} \rightarrow C_4H_2 + C_3H_3^{\bullet} \qquad (3.5)$$

$$C_7H_5^{\bullet} \rightarrow C_5H_3^{\bullet} + C_2H_2 \qquad (3.6)$$

According to the calculations of Derudi et al., reaction 3.5 proceeds via two mechanisms with overall energy barriers of 84.4 and 86.4 kcal mol^{-1} while reaction 3.6 has an overall energy barrier of 86.2 kcal mol^{-1}. Low pressure (0.013 bar) rate constants

for Pathways 3.5 and 3.6 are (8.710×10^{92} s^{-1}) ($T^{-23.08}$) exp (-117.07 kcal mol^{-1} / RT) and (3.162×10^{83} s^{-1})($T^{-20.81}$) exp(-109.41 kcal mol^{-1} / RT), respectively.

C_4H_2 and $C_3H_3^{\bullet}$ are produced in significant concentrations in this benzyl pyrolysis study as indicated by the prominence of m/e 33 and m/e 50 peaks in the pyrolysis mass spectra for $C_6H_5CH_2Cl$. Due to the significant production of C_7H_5 at the early stages of pyrolysis it appears likely that C_4H_2 and $C_3H_3^{\bullet}$ are produced due to reaction 3.5. $C_5H_3^{\bullet}$ is also produced to a lesser extent as indicated by the m/e 63 peak indicating that reaction 3.6 is also important. The prevalence of reaction 3.5 may be due to the somewhat lower activation barrier as calculated by Derudi et al.

3.5 Conclusion

The pyrolysis of the benzyl radical was studied by flash pyrolysis of $C_6H_5CH_2Cl$, $C_6H_5CH_2Br$, $C_6H_5CD_2Cl$, and $C_6D_5CH_2Cl$ with VUV-PI-TOFMS detection. Decomposition of benzyl by loss of hydrogen atom (reaction 3.2) was observed as the dominant pathway in the low temperature region (1100 K - 1300 K). Based on a comparison of the pyrolysis of undeuterated forms of benzyl chloride with the two partially deuterated forms, it is observed that an H atom is lost both from the side-chain and the ring portion of the benzyl radical, but not in a fully statistical manner. Loss of an H atom from the side-chain observed in this study is not consistent with direct formation of fulvenallene as the C_7H_6 product, suggesting significant isomerization of benzyl prior

to dissociation to fulvenallene and H atom or potential, but less likely, formation of alternative C_7H_6 products.

Secondary decomposition of C_7H_6 by the loss of H atoms occurs very rapidly after loss of the first H atom from benzyl in this study. Notably, decomposition of C_7H_6 to C_5H_4 and C_2H_2 is not observed to be significant. Instead, significant production of C_7H_5 is observed which appears to further decompose primarily to C_3H_3 and C_4H_2. Some decomposition or C_7H_5 to C_5H_3 and C_2H_2 is also observed.

Loss of methyl from benzyl radical (reaction 3.4) is observed to be the second most significant benzyl decomposition channel as recently predicted theoretically by Derudi et al. Decomposition of benzyl to C_5H_5 and acetylene (reaction 3.2) was observed as a minor channel. Decomposition of benzyl to C_3H_3 and C_4H_4 (reaction 3.3), although historically expected to be another benzyl decomposition pathway, did not appear to occur in this study.

References

(1) Smith, R. D. *The Journal of Physical Chemistry* **1979**, *83*, 1553–1563.

(2) Rao, V.; Skinner, G. B. *Symposium (International) on Combustion* **1986**, 809–814.

(3) Sivaramakrishnan, R.; Tranter, R. S.; Brezinsky, K. *The Journal of Physical Chemistry. A* **2006**, *110*, 9400–9404.

(4) Frochtenicht, R.; Hippler, H.; Troe, J.; Toennie, J. P.; Hipplerb, H.; Troeb, J.; Toennies, J. P. *J. Photochem Photobiol. A* **1994**, *80*, 33–37.

(5) Hippler, H.; Riehn, C.; Troe, J.; Weitzel, K. M.; H. Hippler, C. Riehn, J. Troe, K. M. W. *Journal of Physical Chemistry* **1990**, *94*, 6321–6326.

(6) Song, Y.; Zheng, X.; Lucas, M.; Zhang, J. *Physical Chemistry Chemical Physics : PCCP* **2011**, *13*, 8296–305.

(7) Oehlschlaeger, M. a; Davidson, D. F.; Hanson, R. K. *The Journal of Physical Chemistry. A* **2006**, *110*, 6649–53.

(8) Jones, J.; Bacskay, G. B.; Mackie, J. C. *Journal of Physical Chemistry* **2006**, *97*, 7105–7113.

(9) Cavallotti, C.; Derudi, M.; Rota, R. *Proceedings of the Combustion Institute* **2009**, *32*, 115–121.

(10) Da Silva, G.; Cole, J. a; Bozzelli, J. W. *The Journal of Physical Chemistry A* **2009**, *113*, 6111–20.

(11) Wong, M. W.; Wentrup, C. *The Journal of Organic Chemistry* **1996**, *61*, 7022–7029.

(12) Chambreau, S. D.; Zhang, J.; Traeger, J. C.; Morton, T. H. *International Journal of Mass Spectrometry* **2000**, *199*, 17–27.

(13) Kohn, D. W.; Clauberg, H.; Chen, P. *Review of Scientific Instruments* **1992**, *63*, 4003–4005.

(14) Traeger, J. C.; Kompe, B. M. *International Journal of Mass Spectrometry and Ion Processes* **1990**, *101*, 111–120.

(15) Akopyan, M. E.; Vilesov, F. I.; Lopatin, S. N. *Khim. Vys. Energ* **1972**, *6*, 110.

(16) Akopyan, M. E.; Vilesov, F. I. *Zh. Fiz. Khim.* **1966**, *40*, 125.

(17) Ohno, K.; Okamura, K. *Journal of Physical Chemistry* **1995**, *99*, 14247–14253.

(18) Plessis, P.; Marmet, P. *International Journal of Mass Spectrometry and Ion Processes* **1986**, *70*, 23–44.

(19) Weitzel, K.; Mähnert, J.; Penno, M. *Chemical Physics Letters* **1994**, *2614*, 371–380.

(20) Colket, M. B.; Seery, D. J. *Symposium (International) on Combustion* **1994**, *25*, 883–891.

(21) Sivaramakrishnan, R.; Su, M.-C.; Michael, J. V. *Proceedings of the Combustion Institute* **2011**, *33*, 243–250.

(22) Detilleux, V.; Vandooren, J. *The journal of physical chemistry. A* **2009**, *113*, 10913–22.

(23) Derudi, M.; Polino, D.; Cavallotti, C. *Physical chemistry chemical physics : PCCP* **2011**, *13*, 21308–18.

(24) Da Silva, G.; Bozzelli, J. W. *The Journal of Physical Chemistry A* **2009**, *113*, 12045–8.

(25) Da Silva, G.; Cole, J. a; Bozzelli, J. W. *The Journal of Physical Chemistry. A* **2010**, *114*, 2275–83.

(26) Polino, D.; Famulari, A.; Cavallotti, C. *The Journal of Physical Chemistry A* **2011**, *115*, 7928–36.

(27) Polino, D.; Cavallotti, C. *The Journal of Physical Chemistry A* **2011**, *115*, 10281–9.

(28) Da Silva, G.; Trevitt, A. J. *Physical Chemistry Chemical Physics : PCCP* **2011**, *13*, 8940–52.

CHAPTER 4

Pyrolysis of 1-Butyl Radical and 1-Pentyl Radical

4.1 Introduction

Alkyl radicals have long been known to be significant intermediates in the processing and combustion of hydrocarbon fuels.[1–4] Due to the importance of their thermal decomposition reactions in these processes, alkyl radicals have been the subject of experimental and theoretical studies for some time.[5–9] However, due to their unstable nature and the complexity of their decomposition reactions, pyrolysis of alkyl radicals continues to be an area of active experimental and theoretical research interest.

The pyrolysis of small alkyl bromides, such as 1-bromobutane and 1-bromopentane, is known to proceed through competitive C-Br bond homolysis and HBr 1,2- molecular elimination. Due to the relatively weak C-Br bond, pyrolysis of $C_nH_{n+1}Br$ ($n \geq 4$) primarily produces an alkyl radical, making alkyl bromides a potential source of alkyl radicals for study.[10]

$$C_4H_9Br \rightarrow {}^{\bullet}C_4H_9 + {}^{\bullet}Br \qquad (4.1)$$

$$C_4H_9Br \rightarrow C_4H_8 + HBr \qquad (4.2)$$

The importance of alkyl radicals in the thermal decomposition of alkanes was first suggested by Rice and Herzfeld in seminal papers in the 1930s.[1,2] Based on the (at the

time) recent discovery of the existence of alkyl radicals and theoretical arguments, they proposed cleavage of C-C bonds to create two free radicals which subsequently undergo secondary C-C bond cleavage at the radical β-position.

$$C_nH_{n+2} \rightarrow {}^{\bullet}C_iH_{2i+1} + {}^{\bullet}C_jH2_{j+1} \qquad (i + j = n) \qquad (4.3)$$

$${}^{\bullet}CH_2CH_2{-}CH_2{-}R \rightarrow CH_2{=}CH_2 + {}^{\bullet}CH_2{-}R \qquad (4.4)$$

It was later determined that the Rice-Herzfeld model over-predicted the production of ethene, particularly for large alkyl radicals. Kossiakoff and Rice later adjusted the model to include isomerization reactions for alkyl radicals containing 6 or more carbon atoms involving 1,5 - H atom transfer through six membered cyclic intermediates to produce secondary radicals whose β-scission products could include olefins other than ethene.[4]

Since the pioneering works of Rice and coworkers, significant efforts have been devoted to evaluating the energetics and relative rates of alkyl isomerization and β-scission reactions under a variety of experimental conditions.[5–8,10–18] The experimental determination of accurate kinetic parameters and branching ratios for alkyl decomposition has proven difficult since the intermediates are short lived and have many potential decomposition pathways. Prior pyrolysis experiments have had sampling times significantly longer than lifetimes of the intermediates, thus their relative concentrations in the initial stages of decomposition have been estimated based on end product analysis. Over the last decade, theoretical calculations have become an increasingly important tool to study alkyl radical decomposition and address some of the experimental difficulties[19–

[23] although the large number of potential decomposition pathways still make these studies challenging.

1-Butyl and 1-propyl decomposition are of particular interest. First, they are significant products from initial C-C bond cleavage reactions in C_7 to C_{10} alkanes that are abundant in liquid petroleum fuels. Thus, their thermal decomposition reactions are of prime importance in fuel combustion. Second, due to their small chain length, their cyclic H migration isomerizations necessarily involve more strained ring structures giving them higher reaction barriers than isomerization reactions of larger alkyl radicals. H migration and β-scission reactions are summarized for 1-butyl and 1-propyl in Schemes 4.1 and 4.2.

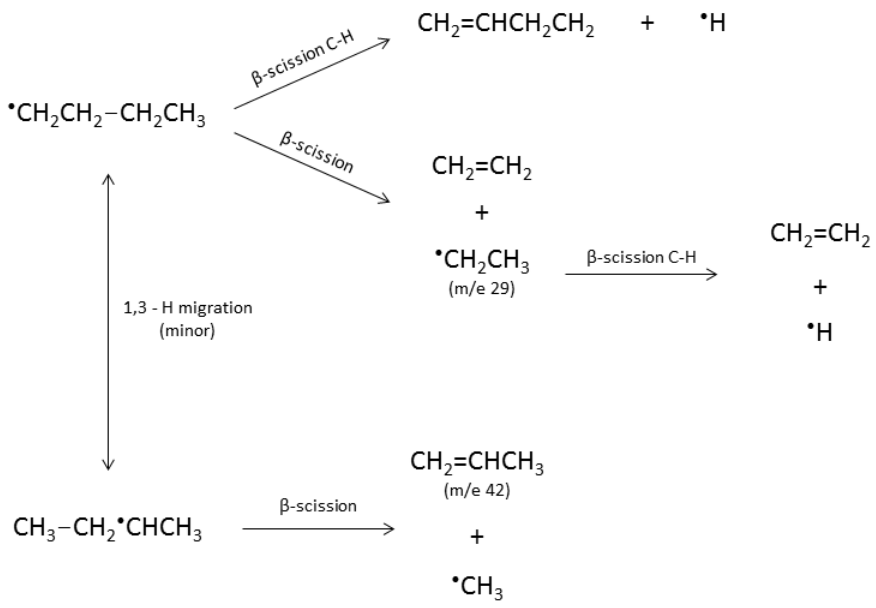

Scheme 4.1 H- migration and β-scission pathways for 1-butyl radical.

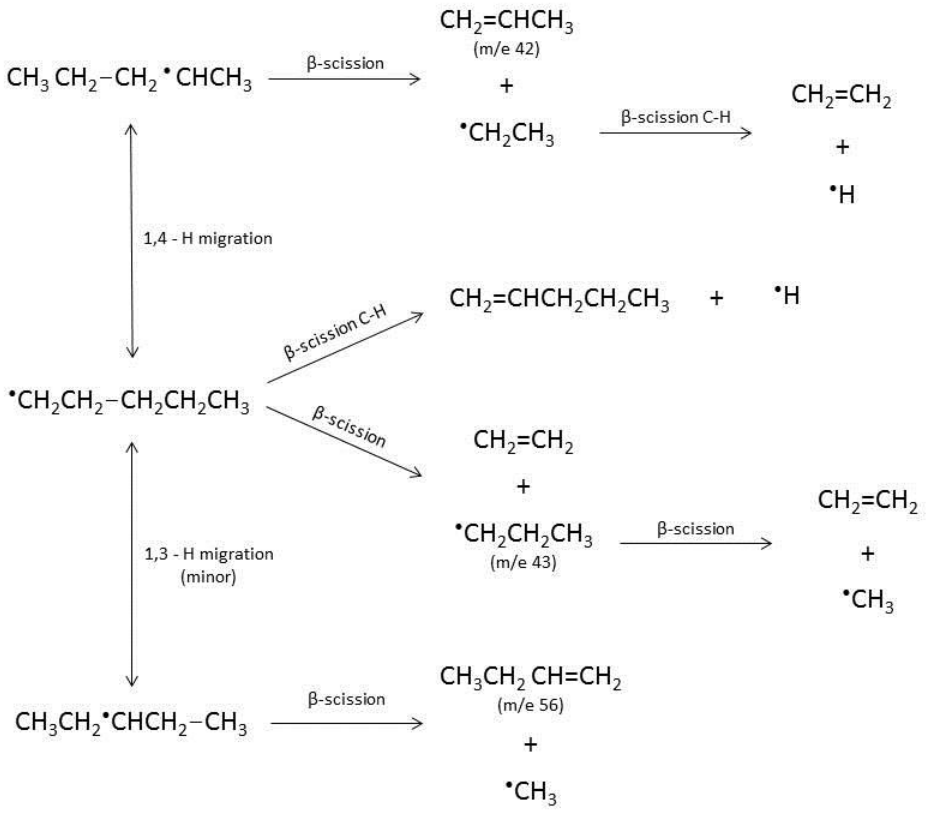

Scheme 4.2 H- migration and β-scission pathways for 1-pentyl radical.

The thermal decomposition and isomerization of 1-butyl and 1-propyl radicals was studied by Yamauchi et. al. in 1999 using a shock tube coupled with atomic resonance absorption spectroscopy.[15] They estimated activation energies of 29.2 kcal mol^{-1} for β-scission reactions, 38.1 kcal mol^{-1} for 1,3 H atom migration in 1-butyl, and 21.5 kcal mol^{-1} for 1,4 H atom migration in 1-pentyl with pre-exponential factors of $1.8x10^{14}$, $3.6x10^{12}$, and $3.0x10^{11}$ s^{-1}, respectively, in the temperature range 1000K to 1300K. In a 2010, Zheng et. al. used ab initio theoretical calculations to determine the

activation energy of the β-scission of 1-butyl reported as 28.62 kcal $mole^{-1}$ which was in reasonable agreement with that obtained by Knayazev et. al. in 1996 at 27.82 kcal mol^{-1} obtained in a flow reactor experiment. Based on these data, 1-butyl 1,3 - H migration followed by β-scission has been considered a minor decomposition channel relative to direct β-scission of the 1-butyl radical.

Tsang et. al. reported shock tube decomposition of 1-pentyl radical in the temperature range 850 K to 1000 K in 1998. Their results indicated that isomerization of 1-pentyl to 2-pentyl followed by β-scission of 2-pentyl was the primary decomposition channel in that temperature range and observed increased direct β-scission of 1-pentyl with increased temperature. They also observed isomerization of 1-pentyl to 3-pentyl followed by β-scission produce 1-butene with an approximate product fraction of 10% despite the apparently high energetic barrier of 1,3 H -migration. Awan et. al., from the same group at NIST, reported new shock tube experiments in 2012. They changed their prior conclusion and adjusted their 3-pentyl decomposition product fraction to less than 1 %, also concluding that decomposition through 2-pentyl occurred preferentially below 900 K above which decomposition of 1-pentyl without isomerization was dominant. A recent theoretical study by Davis et. al. on H migration across 1-alkyl radicals reported isomerization barriers of 38.7 kcal mol^{-1} for 1,3 H-migration for 1-butyl and 1-pentyl and 23.2 kcal mol^{-1} for 1,4 H-migration in 1-pentyl.

In this study, flash pyrolysis vacuum-ultraviolet mass spectrometry (VUV-TOFMS) is used to directly observe reactive intermediates in the pyrolysis of 1-

bromobutane and 1-bromopentane and the pyrolysis of 1-butyl and 1-pentyl radicals generated upon C-Br bond fission in the 20 - 100 μs time scale. Products of 1-butyl and 1-pentyl pyrolysis are directly observed and the extent of H migration prior to decomposition is estimated.

4.2 Experimental

1-bromobutane and 1-bromopentane pyrolysis experiments were conducted on a home-built vacuum ultraviolet (VUV) photoionization time-of-flight mass spectrometer (TOFMS) apparatus that has been previously described.[24] C_4H_9Br (99 %) and $C_5H_{11}Br$ (99 %) were obtained from Sigma-Aldrich and used without further purification. Samples were diluted to approximately 1% concentration in He carrier gas by passing He through liquid C_4H_9Br or $C_5H_{11}Br$ contained in glass bubblers maintained at 0 ^{0}C for C_4H_9Br and 20 ^{0}C for $C_5H_{11}Br$.

4.3 Results

(a) 1-bromobutane pyrolysis

Flash pyrolysis of C_4H_9Br was performed in the temperature range 500 K to 1430 K. Results of the pyrolysis of C_4H_9Br in He are shown in Figures 4.1 and 4.2. Mass spectra for the pyrolysis of C_4H_9Br from 500 K to 1090 K are shown in Figure 4.1. Also included is a room temperature mass spectrum in which a doublet at m/e 136 and 138 is

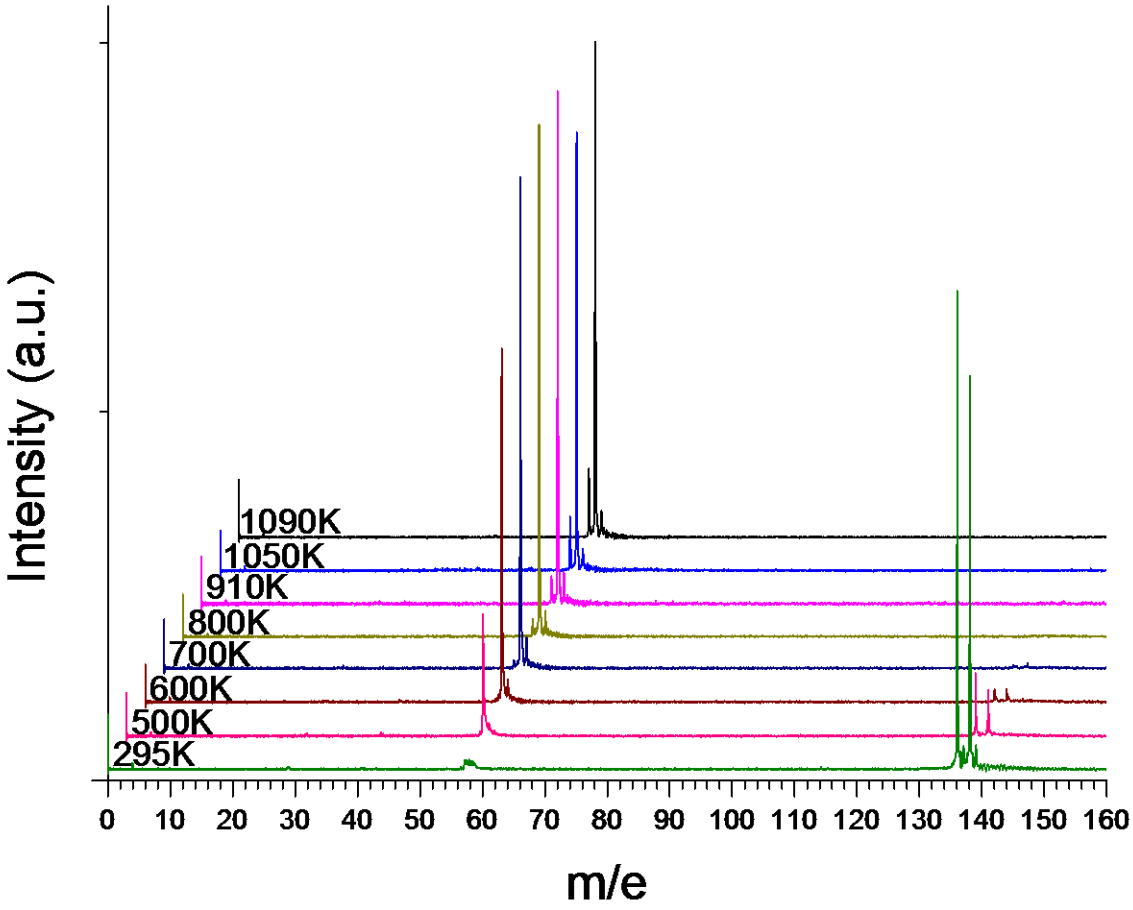

Figure 4.1 Stack plot of mass spectra for pyrolysis of C_4H_9Br (~1%) in He at room temperature and pyrolysis temperatures 500 K to 1090 K. Mass spectra are offset for clarity.

observed. These peaks are due to the parent, C_4H_9Br, and appear as a doublet due to the presence of both ^{79}Br and ^{81}Br isotopes which have natural abundances of 0.507 and 0.4931, respectively. A small, broad peak at m/e 57 is also observed due to a small amount of photoionization fragmentation (PIF) of C_4H_9Br to yield $C_4H_9^{\bullet+}$. The appearance energy (AE) of $C_4H_9^{\bullet+}$ from C_4H_9Br has not been measured but it appears to be slightly higher than the 10.45eV imparted by photons from the ionization source.

Upon modest heating to 500 K, decomposition of C_4H_9Br is observed. The intensity of the m/e 136 and 138 doublet drops dramatically with a concomitant appearance of a peak at m/e 57 due to $C_4H_9^{\bullet}$ produced by C-Br bond fission. At 600 K, further decomposition of C_4H_9Br is observed with m/e 136 and 138 continuing to drop in intensity while the intensity of m/e 57 increases significantly. A small peak is also observed at m/e 58 due to the presence of ^{13}C isotopes with natural abundance 0.011 among the four carbon atoms in $C_4H_9^{\bullet}$. At 700 K, C_4H_9Br decomposes further. Peaks at m/e 136 and 138 fall into the baseline while m/e 57 increases significantly in intensity.

At 800 K, a small peak at m/e 56 appears with intensity approximately 3% that of m/e 57. Intensity of the m/e 56 increases as the pyrolysis temperature is raised, reaching 4 %, 10 %, and 15 % of the intensity of m/e 57 at 910 K, 1050 K, and 1090 K, respectively. The peak at m/e 56 may be due to C_4H_8 produced via reaction 4.2. Secondary loss of H atom from $^{\bullet}C_4H_9$ is also a likely source for C_4H_8 particularly as the pyrolysis temperature is increased.

$$^{\bullet}C_4H_9 \rightarrow H^{\bullet} + C_4H_8 \qquad (4.5)$$

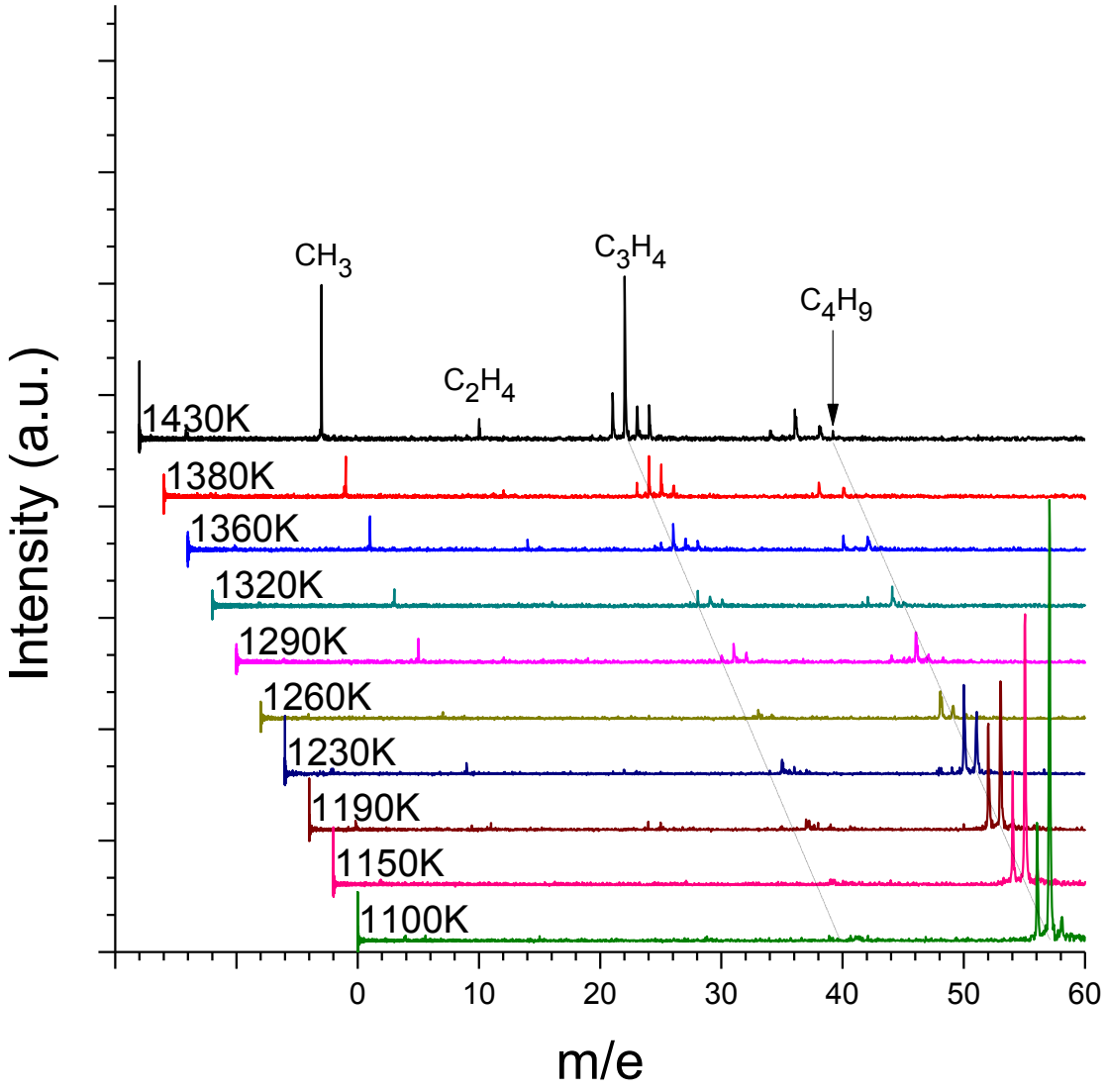

Figure 4.2 Stack plot of mass spectra for pyrolysis of C_4H_9Br (~1%) in He at pyrolysis temperatures 1100 K to 1430 K. Mass spectra are offset for clarity.

Mass spectra for the pyrolysis of C_4H_9Br from 1100 K to 1430 K are shown in Figure 4.2. A decrease in the intensity of the m/e 57 peak is observed at 1100K with a further decrease at 1150 K indicating the consumption of $^{\bullet}C_4H_9$ by secondary decomposition processes. A likely product of this decomposition is C_2H_4. The IE of C_2H_4 is 10.51eV, thus cold C_2H_4 molecules are not ionized by the 10.45 eV ionization photons at modest pyrolysis temperatures where C_2H_4 molecules are efficiently cooled by supersonic expansion prior to detection. However, small peaks at m/e 28 due to C_2H_4 are observed at pyrolysis temperatures 1360 K and above, where cooling of the product molecules is less efficient, indicating that C_2H_4 is likely produced at lower temperatures as well. The pyrolysis complement to C_2H_4 from $^{\bullet}C_4H_9$ is $^{\bullet}C_2H_5$, ethyl radical, which is readily ionized in this experiment but a peak at m/e 29 is not observed. The ethyl radical is known to rapidly eject a hydrogen atom to produce ethene which may explain why a peak at m/e 29 is not observed.[25]

$$^{\bullet}C_2H_5 \rightarrow {}^{\bullet}H + C_2H_4 \qquad (4.6)$$

Further decomposition of $^{\bullet}C_4H_9$ occurs at 1190 K indicated by the continued drop in intensity of m/e 57. The intensity of m/e 56 also drops slightly indicating decomposition of C_4H_8. Small peaks also appear at m/e 15 and m/e 41, corresponding to $^{\bullet}CH_3$ and $^{\bullet}C_3H_5$ suggesting decomposition of C_4H_8 by loss of methyl radical. Further decomposition of C_4H_8 is observed at 1260 and 1290 K.

$$C_4H_8 \rightarrow {}^{\bullet}CH_3 + {}^{\bullet}C_3H_5 \qquad (4.7)$$

At 1290 K a small peak appears at m/e 54 indicating production of C_4H_6 suggesting hydrogen elimination from C_4H_8. The peak at m/e 56 drops in intensity as C_4H_8 is consumed by H_2 elimination and methyl loss processes. Intensity of m/e 56 drops by 50% from 1290 K to 1320 K. Peaks at m/e 41 and 54 increase slightly in intensity indicating continued H_2 elimination and methyl loss. A peak at m/e 40 corresponding to C_3H_4, is also observed. The intensity of m/e 40 is slightly larger than m/e 41 likely due to rapid H atoms loss from $^{\bullet}C_3H_5$ analogous to the situation with $^{\bullet}C_2H_5$ and C_2H_4.

At 1360 and 1380 K, secondary methyl loss from C_4H_8 becomes more prominent with peaks at m/e 15, 40, and 41 increasing in intensity. The peak at m/e 54 does not grow significantly indicating the preference of methyl loss versus H_2 elimination. Elimination of H_2 from C_3H_5 results in the production of C_3H_3, propargyl radical, as indicated by the peak at m/e 39. A small peak is also observed at m/e 42 due to C_3H_6 produced via loss of methyl from $^{\bullet}C_4H_9$.

$$^{\bullet}C_4H_9 \rightarrow {}^{\bullet}CH_3 + C_3H_6 \qquad (4.8)$$

At 1430 K, methyl production increases significantly with the m/e 15 peak growing to four times the intensity of m/e 15 at 1380 K. Methyl loss from $^{\bullet}C_4H_9$ is significantly greater as indicated by the significant growth of m/e 42. The peak at m/e 40, C_3H_4 also increases significantly in intensity indicating further loss of methyl from C_4H_8.

(b) 1-bromopentane pyrolysis

Flash pyrolysis of $C_5H_{11}Br$ was performed in the temperature range 630 K to 1480 K. Results of the pyrolysis of $C_5H_{11}Br$ in He are shown in Figures 4.3, 4.4, and 4.5. Mass spectra for the pyrolysis of $C_5H_{11}Br$ from 630 K to 1120 K are shown in Figures 4.3 and 4.4. Figure 4.4 is enlarged in the m/e 0 to m/e 80 mass region to more clearly show the pyrolysis product peaks. Peaks at m/e 150 and 152 in the room temperature spectrum in Figure 4.3 are due to the parent, $C_5H_{11}Br$. Significant photoionization fragmentation of $C_5H_{11}Br$ is observed. Peaks can clearly be seen at m/e 29, 41, 42, 43, 55, 57, 71, and 72 due to $C_2H_5^{\bullet+}$, $C_3H_5^{\bullet+}$, $C_3H_6^{\bullet+}$, $C_3H_7^{\bullet+}$, $C_4H_7^{\bullet+}$, $C_4H_9^{\bullet+}$, $C_5H_{11}^{\bullet+}$, and, $C_5H_{12}^{\bullet+}$, respectively. Appearance energies for these PI fragments from $C_5H_{11}Br$ have not been measured but they appear to be lower than the 10.45 eV supplied by photons from the photoionization source used in this experiment. Unfortunately, the appearance of $C_5H_{12}^{\bullet+}$ is not easily explained. Secondary reactions such as H abstraction should be unlikely at this temperature. Condensation of smaller fragments in the ionization region, although also unlikely due to mutual positive charges, may be responsible for $C_5H_{12}^{\bullet+}$. Regardless, m/e 72 quickly diminishes as the temperature of the pyrolysis nozzle is increases and pyrolysis results otherwise appear sensible. Despite the presence of PIF, production of pyrolysis products can be relatively accurately judged by increases in peak in intensities at elevated temperatures.

Significant thermal decomposition of $C_5H_{11}Br$ is observed at 630 K as indicated by marked decreases in the intensity of the m/e 150 and 152 peaks. There is a simultaneous large increase in the intensity of m/e 71 indicating $^{\bullet}C_5H_{11}$ production by

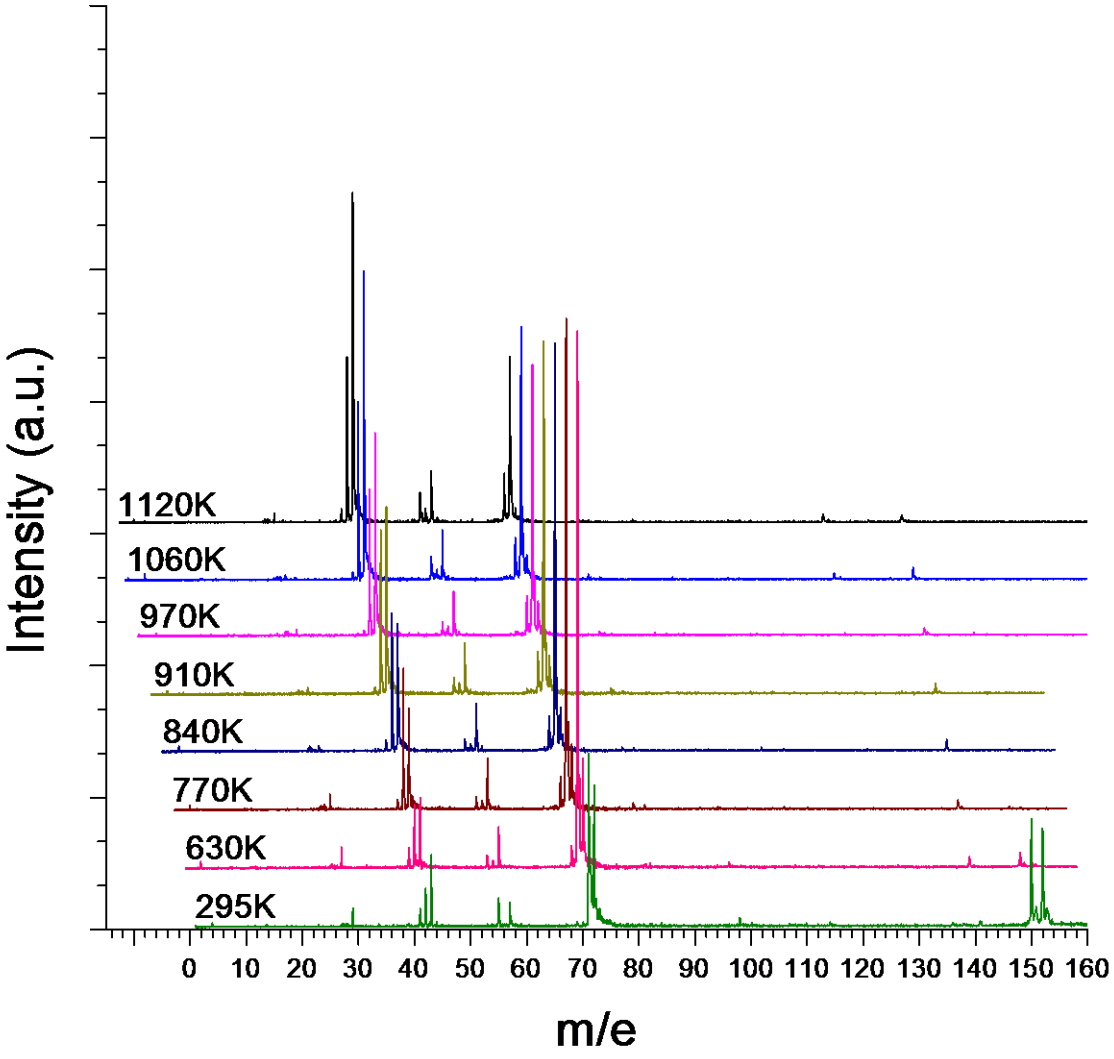

Figure 4.3 Stack plot of mass spectra for pyrolysis of $C_5H_{11}Br$ (~1%) in He at room temperature and pyrolysis temperatures 630 K to 1120 K. Mass spectra are offset for clarity.

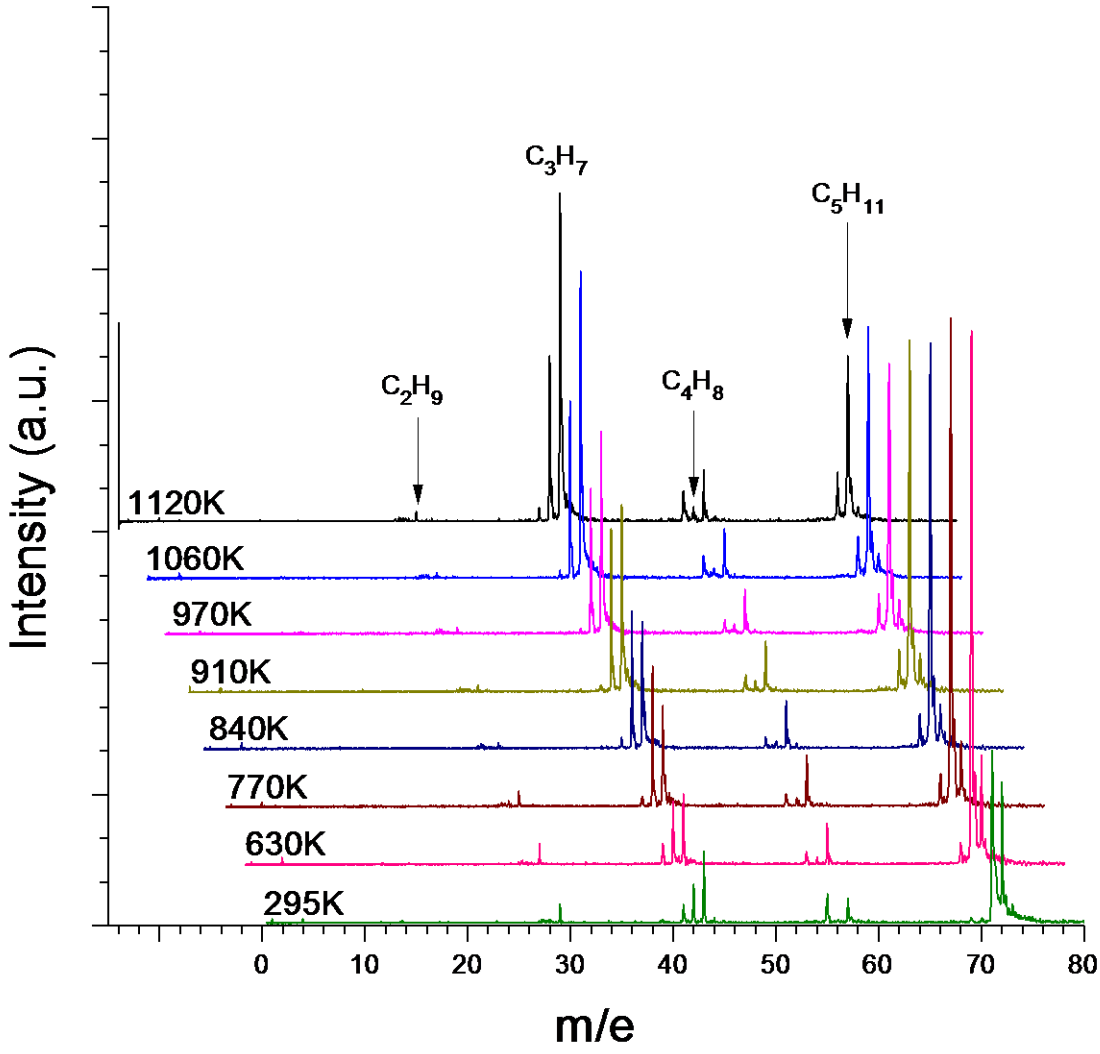

Figure 4.4 Stack plot of mass spectra for pyrolysis of $C_5H_{11}Br$ (~1%) in He at room temperature and pyrolysis temperatures 630 K to 1120 K enlarged in the m/e 0 to 80 mass region. Mass spectra are offset for clarity.

C-Br bond homolysis (reaction 4.9). A small peak of approximately 2% of the intensity of m/e 71 also appears at m/e 70. This peak is due to C_5H_{10} produced by the elimination of HBr from $C_5H_{11}Br$ (reaction 4.10) and, increasingly by ejection of H atom from $^{\bullet}C_5H_{11}$ as the pyrolysis temperature is increased.

$$C_5H_{11}Br \rightarrow {}^{\bullet}C_5H_{11} + {}^{\bullet}Br \qquad (4.9)$$

$$C_5H_{11}Br \rightarrow C_5H_{10} + HBr \qquad (4.10)$$

There is also an increase in the intensity of the peak at m/e 57. Although this could be due to the thermal decomposition of $C_5H_{11}Br$, this process would also produce CH_2Br which would certainly be ionized and detected in this system but is not observed. Alternatively, if the AE of $C_4H_9^{\bullet+}$ is close to the 10.45 eV energy provided by the ionization source, m/e 57 could be due to increased PIF producing $C_4H_9^{\bullet+}$ due to less efficient cooling of $C_5H_{11}Br$ at the elevated temperature. Given that the intensity of m/e 57 stays constant at higher temperatures, this situation appears to be more likely.

The intensity of m/e 42 also increases at 630 K. This could also be due to increased PIF but, given that the intensity of m/e 42 increases sharply at 770 K, there is also likely to be a contribution from pyrolytic generation of C_3H_6 and $^{\bullet}C_2H_5$ from the decomposition of $^{\bullet}C_5H_{11}$ as shown below.

$$^{\bullet}C_5H_{11} \rightarrow C_3H_6 + {}^{\bullet}C_2H_5 \qquad (4.11)$$

As mentioned previously, $^{\bullet}C_2H_5$ quickly decomposes to H atoms and C_2H_4 which cannot be detected at modest temperatures. This explains why the intensity of m/e 29 does not increase significantly at 630 K.

At 770 K, peaks at m/e 150 and 152 fall into the baseline indicating further decomposition of $C_5H_{11}Br$. The intensity of m/e 71 falls slightly due to further decomposition of $^{\bullet}C_5H_{11.}$ The peak at m/e 70 increases in intensity to 4% of that of m/e 71 indicating increased HBr elimination although C_5H_{10} is likely also produced by loss of H atom from $^{\bullet}C_5H_{11.}$ The peak at m/e 42 roughly doubles in intensity, indicating the prevalence of reaction 4.11. The peak at m/e 43 increases in intensity by about 70% indicating the production of $^{\bullet}C_3H_7$ by decomposition of $^{\bullet}C_5H_{11}$. The complementary product is C_2H_4 which is not detected at this temperature.

$$^{\bullet}C_5H_{11} \rightarrow {}^{\bullet}C_3H_7 + C_2H_4 \qquad (4.12)$$

A small peak also appears at m/e 56 at 770K due to C_4H_8 produced by loss of methyl from $^{\bullet}C_5H_{11}$. A very small peak at m/e 15 is also present but is smaller than that at m/e 56 likely due to its smaller ionization cross section. Other peaks have unchanged intensities from 630 K to 770 K.

$$^{\bullet}C_5H_{11} \rightarrow C_4H_8 + {}^{\bullet}CH_3 \qquad (4.13)$$

As the temperature is raised from 770 K to 1120 K, m/e 43 steadily grows having slightly larger intensity than m/e 42 at 910 K and, ultimately, having 4 times the intensity at 1120 K than at 770 K. The peak at m/e 42 grows less significantly, becoming 30%

more intense at 1120 K than at 770 K. At 1120 K, intensity of m/e 42 is 50% of that of m/e 43. There is a simultaneous steady decrease in the intensity of m/e 71 over this temperature range indicating the consumption of $^{\bullet}C_5H_{11}$ by reactions 4.11 and 4.12. At 1060 K and 1120 K, intensities of m/e 55 and m/e 56 increase slightly indicating a small amount of methyl loss from C_5H_{10} and C_5H_{11}, producing C_4H_7 and C_4H_8, respectively.

$$C_5H_{10} \rightarrow C_4H_7 + {}^{\bullet}CH_3 \qquad (4.14)$$

Mass spectra for the pyrolysis of $C_5H_{11}Br$ from 1160 K to 1480 K are shown in Figure 4.5. At 1160 K and 1220 K, further decomposition of $^{\bullet}C_5H_{11}$ is observed as m/e 71 decreases significantly in intensity. Peaks at m/ 42 and 43 grow proportionally indicating further production of C_3H_6 and $^{\bullet}C_3H_7$ by the dominant decomposition channels, reactions 4.11 and 4.12. A small peak at m/e 29 is also observed, verifying the production of $^{\bullet}C_2H_5$ by reaction 4.9 despite rapid loss of H atom. Secondary elimination of H_2 from C_3H_7 is also observed at 1220 K resulting in a small peak at m/e 41 due to C_3H_5. All other peaks have approximately the same intensities as they did in the lower temperature spectra.

At 1290 K, the m/e 71 peak decreases in intensity by about 50% relative to that at 1220 K and becomes approximately equal in intensity to the m/e 70 peak. There is a small increase in the intensity of the peak at m/e 47 due to C_4H_7 production via reaction 4.12. Ethene is observed at m/e 28 as cooling becomes less efficient and a portion of ethene molecules are ionized and detected. All other peaks have unchanged intensities at 1290 K.

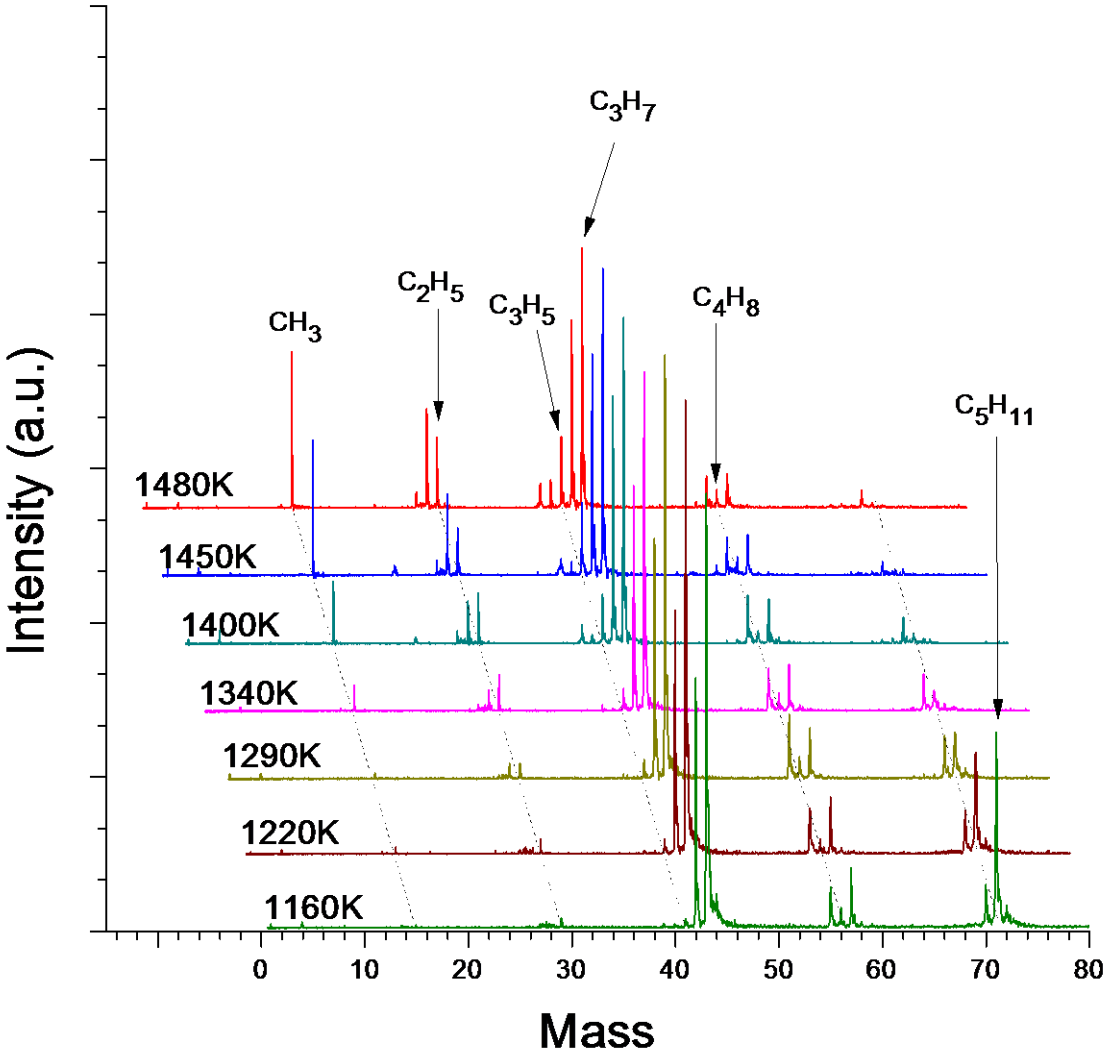

Figure 4.5 Stack plot of mass spectra for pyrolysis of $C_5H_{11}Br$ (~1%) in He at pyrolysis temperatures 1160 K to 1480 K. Mass spectra are offset for clarity.

$^{\bullet}C_5H_{11}$ decomposition continues at 1340 K as m/e 71 reduces in intensity by 60 %. The peak at m/e 29 grows in intensity by approximately three times although it is still relatively low due to rapid loss of H atom via reaction 4.6. The intensity m/e 41 decreases by about 20 % accompanied by a significant increase in the intensity of m/e 15 indicating loss of methyl from $^{\bullet}C_3H_7$ also producing ethene as was observed in prior propyl radical pyrolysis experiments in our lab by Weber et. al. [25]

$$^{\bullet}C_3H_7 \rightarrow {}^{\bullet}CH_3 + C_2H_4 \qquad (4.15)$$

Raising the pyrolysis temperature from 1340 K up to 1480 K results in significant methyl production due to reaction 4.15 as indicated by the significant growth of m/e 15. Peaks at m/e 28 and m/e 29 also increase significantly in intensity. The peak at m/e 71 falls into the baseline at 1400 K while there is a steady decrease in the intensity of m/e 70 from 1340 K to 1400K as C_5H_{10} is consumed by loss of methyl via reaction 4.14.

Significant H_2 elimination from C_3 products is also observed at 1340 K and above. $^{\bullet}C_3H_5$ becomes more significant, indicated by the steadily increasing intensity of m/e 41 reaching 15 % of the intensity of m/e 43 at 1400 K and 25% at 1450 K. A peak at m/e 39 indicating elimination of H_2 from $^{\bullet}C_3H_5$ to produce $^{\bullet}C_3H_3$, propargyl radical, is also observed at 1400 K. Intensity of m/e 39 is 25% that of m/e 41 at 1400 to 1480 K. A small peak appears at m/e 40 due to elimination of H_2 from C_3H_6 to form C_3H_4. The fraction of C_3H_4 grows slightly at 1450 K and becomes equivalent with that of $^{\bullet}C_3H_3$ at 1480 K.

4.4 Discussion

Decomposition of 1-bromobutane exhibits dominant formation of 1-butyl molecules allowing for the study of 1-butyl with minimal interference from 1-butene production. No peaks due to decomposition of 1-butyl are observed from 500 K up to1150 K although butyl radicals appear to be consumed by thermal decomposition processes. $^{\bullet}C_4H_9$ is likely to be consumed by a β-scission reaction as suggested by the Rice-Herzfeld mechanism.

$$CH_3CH_2{-}CH_2C^{\bullet}H_2 \rightarrow CH_3C^{\bullet}H_2 + CH_2{=}CH_2 \qquad (4.16)$$

As previously mentioned, ethene is not detected using this experiment except at high pyrolysis temperatures where less efficient cooling allows for the ionization of a fraction of ethene molecules. Ethyl radical also decomposes by losing H atom prior to detection. However the marked drop in the m/e 57 peak and the absence of m/z 15 methyl and peaks corresponding to C_3 products is good evidence of the decomposition of $^{\bullet}C_4H_9$ to ethene and ethyl radical and the speed with which these reactions occur.

C_4H_8 is produced partially by HBr elimination from C_4H_9Br but, given its relatively insignificant production at low pyrolysis temperatures, it appears to be primarily produced by loss of H atom from butyl radical. C_4H_8 undergoes secondary decomposition at temperatures 1270 K above by bond homolysis to produce methyl radical resulting in peaks at m/e 15 due to methyl and m/e 41 due to $^{\bullet}C_3H_5$.

$$CH_3{-}CH_2CH{=}CH_2 \rightarrow {}^{\bullet}CH_3 + {}^{\bullet}CH_2CH{=}CH_2 \qquad (4.17)$$

Secondary decomposition of propenyl radical by H_2 elimination results in the formation of the highly resonantly stabilized $^{\bullet}C_3H_3$, propargyl radical as evidenced by the m/e 39 peak that is observed at temperatures higher than 1270 K. This is further supported by the fact that the increase of intensity of m/e 39 is accompanied by a simultaneous decrease in m/e 41 intensity.

$$^{\bullet}CH_2CH{=}CH_2 \rightarrow {}^{\bullet}CH_2C{\equiv}CH + H_2 \qquad (4.18)$$

C_3H_6 production due to loss of methyl radical from $^{\bullet}C_4H_9$ is observed as a peak at m/e 42, but only at the highest temperatures of 1390 K and above. Production of methyl from the 1-butyl radical is unlikely as it would result in the formation of an unstable diradical as shown below.

$$CH_3{-}CH_2CH_2C^{\bullet}H_2 \rightarrow {}^{\bullet}CH_3 + {}^{\bullet}CH_2CH_2C^{\bullet}H_2 \qquad (4.19)$$

Instead, loss of methyl radical from $^{\bullet}C_4H_9$ likely occurs through the isomerization of 1-butyl to 2-butyl through a 1,3 - H shift that is kinetically unfavorable at lower pyrolysis temperatures followed by β-scission as in the Rice-Herzfeld mechanism.

$$CH_3CH_2CH_2C^{\bullet}H_2 \rightarrow CH_3{-}CH_2C^{\bullet}HCH_3 \rightarrow {}^{\bullet}CH_3 + CH_2{=}CHCH_3 \qquad (4.20)$$

Comparing the maximum m/e 42 peak intensity at 1430 K to the maximum 1-butyl peak intensity at 910 K, reaction 4.20 accounts for no more than a 3 % contribution to $^{\bullet}C_4H_9$ decomposition at the highest temperatures measured.

Pyrolysis of 1-bromopropane proceeds primarily via C-Br bond homolysis although there is minor (~3%) fraction of HBr elimination as well.

$$C_5H_{11}Br \rightarrow {}^{\bullet}C_5H_{11} + {}^{\bullet}Br \quad (4.21)$$

$$C_5H_{11}Br \rightarrow C_5H_{10} + HBr \quad (4.22)$$

At low pyrolysis temperatures of 630 K and 770 K, increases in the intensities of the m/e 29, 42, and 43 peaks represent the production of C_2H_5 (ethyl radical), C_3H_6 (propene), C_3H_7 (propyl radical), respectively. These are due to decomposition of pentyl radical through the two channels shown below. Decomposition to propyl radical and ethene likely occurs through β-scission of the 1-pentyl radical while decomposition to propene and ethyl radical requires isomerization of 1-propyl radical to 2-propyl radical.

$$^{\bullet}CH_2CH_2{-}CH_2CH_2CH_3 \rightarrow C_2H_4 + {}^{\bullet}C_3H_7 \quad (4.23)$$

$$^{\bullet}CH_2CH_2CH_2CH_2CH_3 \rightarrow CH_3{}^{\bullet}CHCH_2{-}CH_2CH_3 \rightarrow C_3H_6 + {}^{\bullet}C_2H_5 \quad (4.24)$$

It has been suggested that this isomerization occurs through a 1,4 H shift via a cyclic intermediate and that this isomerization occurs significantly more rapidly than the decomposition processes.[7,8] These data provide direct evidence of fast isomerization that results in the near 1 to 1 competition between the two decomposition channels. At moderate temperatures of 770 K and 840 K C_3H_6 production is slightly larger than that of C_3H_7 but loss of H atom from propyl radical may also contribute to the production of C_3H_6. At temperatures 910 K and above, the propyl radical product fraction exceeds that of propene, reaching double that of propene at 1120 K. These results are in agreement with conclusions by Awan et. al. based on shock tube decomposition of 1-iodopentane.

They observed propene to be the primary decomposition product at lower temperatures with increasing ethene production as the temperature was increased.[17]

A third, minor, pentyl radical decomposition channel is observed as indicated by the small peak at m/e 48 indicating C_4H_8 production which grows significantly at 1160 K due to loss of methyl from the pentyl radical. Assuming this is also a result of β-scission reaction, isomerization of 1-pentyl to 3-pentyl via 1,3 H atom migration, as shown below, would be required.

$$^{\bullet}CH_2CH_2CH_2CH_2CH_3 \rightarrow CH_3CH_2{}^{\bullet}CHCH_2{-}CH_3 \rightarrow CH_3CH_2CH{=}CH_2 + {}^{\bullet}CH_3 \qquad (4.25)$$

Decomposition of 3-pentyl produces 1-butene and methyl radical. 1,3-isomerization to produce 3-butyl radical requires a more strained cyclic arrangement than the 1,4-migration that produces the 2-butyl radical so the relatively low contribution of 3-butyl decomposition is expected. These results support the earlier conclusions of the NIST group reported by Tsang in 1998 as opposed to the recent conclusions by Awan et. al.

4.5 Conclusion

Isomerization and decomposition of 1-butyl and 1-pentyl radicals was observed by flash pyrolysis vacuum-ultra-violet time-of-flight mass spectrometry of 1-bromobutane and 1-bromopentane and detection on the 20 – 100 μs time scale. Reactive intermediates were directly observed. 1-butyl radical decomposed to ethene and ethyl

radical with ethyl radical rapidly ejecting an H atom to form a second ethene molecule. Loss of H atoms from butyl radical was also a significant decomposition channel. Isomerization of 1-butyl via 1,3 – H migration was observed as a minor channel at 1380 K and above with branching ratio of less than 3% at 1430 K.

1-pentyl radical was observed to decompose mainly by isomerization to 2-pentyl radical followed by β-scission to produce propene and ethyl radicals at temperatures approximately 900 K and below. Above 900 K, β-scission of 1-pentyl to produce ethene and 1-propyl radical became increasingly important. Isomerization to 3-pentyl as a minor channel was also verified. These results are in excellent agreement with shock tube studies by Tsang et. al.[5]

References

(1) Rice, F. *Journal of the American Chemical Society* **1931**, *53*, 1959.

(2) Rice, F.; Herzfeld, K. *Journal of the American Chemical Society* **1934**, *1262*, 284–289.

(3) Rice, F.; Teller, E. *The Journal of Chemical Physics* **1938**, *6*, 489–496.

(4) Kossiakoff, A.; Rice, F. *Journal of the American Chemical Society* **1943**, *65*, 590–595.

(5) Tsang, W.; Walker, J. *Proceedings of the Combustion Institute* **1998**, *27*, 135–142.

(6) Tsang, W.; Walker, J. A.; Manion, J. A. *Proceedings of the Combustion Institute* **2007**, *31*, 141–148.

(7) Watkins, K. W. *Canadian Journal of Chemistry* **1972**, *50*, 3738–3740.

(8) Marshall, R. M. *International Journal of Chemical Kinetics* **1990**, *22*, 935–950.

(9) Endrenyi, L.; Le Roy, D. J. *The Journal of Physical Chemistry* **1989**, *70*, 4081–4084.

(10) Knyazev, V. D.; Slagle, I. R. *The Journal of Physical Chemistry* **1996**, *100*, 5318–5328.

(11) Roothaan, C. C. J.; Pariser, R.; Parr, R. G.; Division, C.; Ordnance, U. S. N.; Slation, T.; Steacie, E. W. R. *The Journal of Chemical Physics* **1955**, *24*, 1260–1261.

(12) Green, J.; Maccoll, A.; Thomas, P. *Journal of the Chemical Society* **1960**, *1960*, 184–187.

(13) Morganroth, W.; Calvert, J. *Journal of the American Chemical Society* **1966**, *88*, 5387–5392.

(14) Watkins, K.; Ostreko, L. *The Journal of Physical Chemistry* **1969**, *73*, 2080–2083.

(15) Yamauchi, N.; Miyoshi, A.; Kosaka, K.; Koshi, M.; Matsui, H. *The Journal of Physical Chemistry A* **1999**, *103*, 2723–2733.

(16) Miyoshi, A.; Widjaja, J.; Yamauchi, N.; Koshi, M.; Matsui, H. *Proceedings of the Combustion Institute* **2002**, *29*, 1285–1293.

(17) Awan, I. A.; Burgess, D. R.; Manion, J. A. *The Journal of Physical Chemistry A* **2012**, *116*, 2895–910.

(18) Comandini, A.; Awan, I. A.; Manion, J. A. *Chemical Physics Letters* **2012**, *552*, 20–26.

(19) Jitariu, L. C.; Jones, L. D.; Robertson, S. H.; Pilling, M. J.; Hillier, I. H. *The Journal of Physical Chemistry A* **2003**, *107*, 8607–8617.

(20) Viskolcz, B.; Seres, L. *Reaction Kinetics and Catalysis Letters* **2009**, *96*, 245–262.

(21) Zheng, X.; Blowers, P. *Theoretical Chemistry Accounts* **2007**, *117*, 207–212.

(22) Wang, F.; Cao, D. B.; Liu, G.; Ren, J.; Li, Y. W. *Theoretical Chemistry Accounts* **2010**, *126*, 87–98.

(23) Davis, A. C.; Francisco, J. S. *The Journal of Physical Chemistry A* **2011**, *115*, 2966–77.

(24) Chambreau, S. *Chemical Physics Letters* **2001**, *343*, 482–488.

(25) Weber, K. H.; Lemieux, J. M.; Zhang, J. *The Journal of Physical Chemistry A* **2009**, *113*, 583–91.

CHAPTER 5

Pyrolysis of Linear Alkanes

5.1 Introduction

Unsaturated hydrocarbons occur in significant concentrations in liquid petroleum and their thermal decomposition reactions play an important role in the processing of crude oil and in the combustion of fossil fuels. The thermal decomposition of linear alkanes is of particular importance in gasoline combustion as high concentrations of linear hydrocarbons are known to result in auto-ignition of the fuel and engine knock. The octane rating scale is established as a measurement of the propensity of fuels for auto-ignition. In the octane scale n-heptane is defined to have an octane rating of 0 and 2,2,4-trimethylpentane is defined as 100 octane where a higher number corresponds to greater engine knock resistance. The octane ratings of selected hydrocarbon fuels are listed in Table 1.[1] Linear hydrocarbons such as, n-hexane, n-heptane, and n-octane contribute heavily to engine knock.

Due to the industrial and scientific importance of linear alkane thermal decomposition reactions, they have been studied extensively since the early 1930s when it was first suggested by Rice and Herzfeld, based on theoretical arguments, that alkanes decompose primarily by C-C bond fission to produce two free radicals.[2–4] Numerous experimental studies have since confirmed their hypothesis but the transient, highly

reactive nature of the radicals produced by initial C-C bond cleavage has made detailed study of alkane decomposition mechanisms difficult.[5–15]

Fuel	Octane Rating
n-octane	-10
n-heptane	0
2-methylheptane	23
n-hexane	25
2-methylhexane	44
1-heptene	60
n-pentane	62
n-butane	91
2,2,4-trimethylpentane	100
benzene	101
toluene	121

Table 5.1 Octane ratings of selected fuels obtained from ref. 1.

Although it is well established that alkane decomposition occurs mainly though C-C bond homolysis, the relative rates of bond homolysis among the several available C-C bonds in linear alkanes is still not certain. Recent efforts have been made to determine the primary site of C-C bond homolysis. Hunter et. al., in 2002, used B3LYP, MP2, CCSD(T), and G2 computational methods and concluded that the β C-C bond was the weakest in n-alkanes.[16] Calculations by Yuan et. al. published in 2011 yielded the following bond dissociation energies for n-heptane.[17]

$$C_7H_{16} \rightarrow {}^{\bullet}C_3H_7 + {}^{\bullet}C_4H_9 \qquad \Delta H = 87.8 \text{ kcal mol}^{-1}$$

$$C_7H_{16} \rightarrow {}^{\bullet}C_2H_5 + {}^{\bullet}C_5H_{11} \qquad \Delta H = 86.7 \text{ kcal mol}^{-1}$$

$$C_7H_{16} \rightarrow {}^{\bullet}CH_3 + {}^{\bullet}C_6H_{13} \qquad \Delta H = 86.8 \text{ kcal mol}^{-1}$$

Yuan et. al. concluded, based on these calculations and pyrolysis synchrotron vacuum ultraviolet photoionization mass spectrometry data that decomposition occurred by cleavage of the α and β C-C bonds. Very recent (2013) reactive molecular dynamics simulations performed by Ding et. al. yielded branching ratios of approximately 3:2:1.8 for the above n-hexane decomposition reactions, respectively, directly contrasting the results of the studies by Yuan et. al. and Hunter et. al.[18]

In this study flash pyrolysis vacuum ultraviolet photoionization time-of-flight mass spectrometry (VUV-PI-TOFMS) is used to directly observe reactive intermediates in the decomposition of n-pentane, n-hexane, n-heptane, n-octane, and n-decane on the 20-100 μs time scale. The pyrolysis results are interpreted along with results of the flash pyrolysis VUV-PI-TOFMS n-butyl and n-pentyl radicals to elucidate n-alkane pyrolysis mechanisms.

5.2 Experimental

n-Alkane pyrolysis experiments were conducted on a home-built vacuum ultraviolet (VUV) photoionization time-of-flight mass spectrometer (TOFMS) apparatus that has been previously described.[19] n-Pentane (99%), n-hexane (99%), n-heptane

(99%), n-octane (99%), and n-decane (99%) were obtained from Sigma-Aldrich and used without further purification. Samples were diluted to approximately 1% concentration in He or Ar by passing the carrier gas through liquid samples contained in glass bubblers immersed in a temperature bath to maintain a vapor pressure of approximately 12 torr.

5.3 Results

(a) Pyrolysis of n-pentane

Mass spectra for the pyrolysis of n-pentane at pyrolysis temperatures 550 K to 1420 K are shown in Figure 5.1. A room temperature mass spectrum is included which has a single peak at m/e 72 due to the parent n-pentane, C_5H_{12}. A small peak at m/e 73 is due to ^{13}C isotopes. The onset of pyrolysis is observed at 850 K. Peaks appear at m/e 42 and 43 corresponding to C_3H_6 and C_3H_7, respectively. The m/e 37 peak is approximately 10 % greater in intensity than m/e 42. Given the well supported Rice-Herzfeld radical mechanism and the fact C_3H_7 was observed to rapidly lose H atom and form C_3H_6 at these temperatures in the pyrolysis of n-butyl and n-pentyl in the previous chapter, the following reactions are primarily responsible for the m/e 42 and m/e 43 peaks.

$$C_5H_{12} \rightarrow {}^{\bullet}C_3H_7 + {}^{\bullet}C_2H_5 \qquad (5.1)$$

$${}^{\bullet}C_3H_7 \rightarrow C_3H_6 + {}^{\bullet}H \qquad (5.2)$$

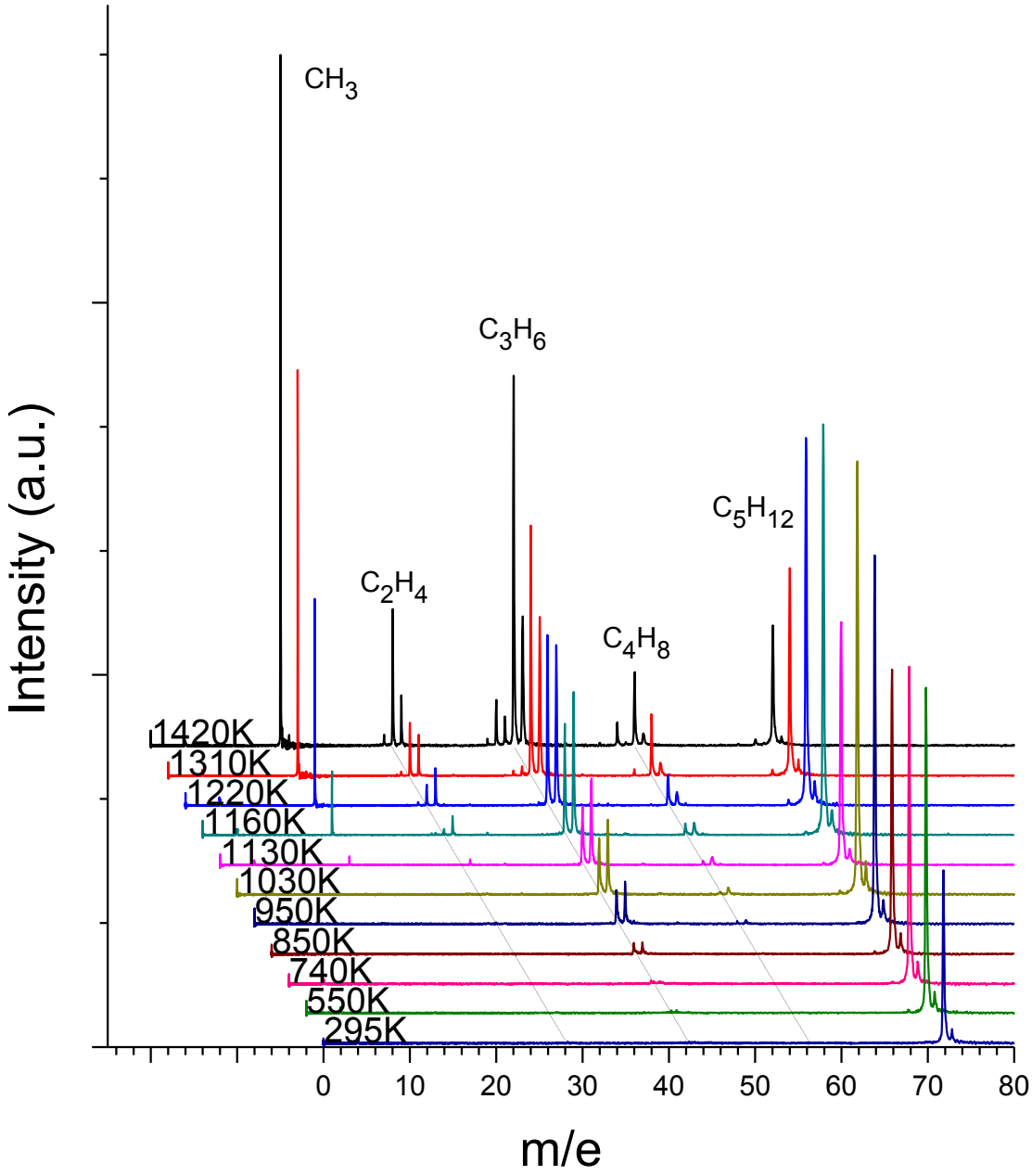

Figure 5.1 Stack plot of mass spectra for pyrolysis of n-pentane (~1%) in He at room temperature and pyrolysis temperatures 550 K to 1420 K. Mass spectra are offset for clarity.

Ethyl radicals also formed in reaction 5.1 also rapidly lose H atoms forming ethene which due to its 10.51 eV ionization potential (IP) is not ionized at 850 K and, thus not detected.

At 950 K, both m/e 42 and m/e 43 grow proportionally to 5 times their intensity as the temperature is raised from 850 K to 950 K. Increased production of $^{\bullet}C_3H_7$ is also observed at 1030 K indicated by increases in intensity of m/e 42 and 43 by 70% and 90%, respectively relative to 950 K. A peak also appears at m/e 57 just above the baseline at 1030 K indicating the production of $^{\bullet}C_4H_9$. This is the result of C-C bond homolysis at the first C-C bond in the n-pentane chain.

$$C_5H_{12} \rightarrow {}^{\bullet}C_4H_9 + {}^{\bullet}CH_3 \qquad (5.3)$$

The peak at m/e 57 approximately doubles in intensity as the temperature is raised to 1130 K. A peak at m/e 15 also becomes visible due to the methyl radical produced in reaction 5.3. A peak at m/e 56 approximately half the intensity of the m/e 57 peak is also observed indicating the ejection if H atoms from $^{\bullet}C_4H_9$. Peaks at m/e 42 and 43 also increase in intensity and a small peak can also be seen at m/e 29 due to $^{\bullet}C_2H_5$ produced by reaction 5.1.

Further decomposition via reactions 5.1 and 5.3 is observed at 1160 K as peaks at m/e 42, 43, 56, and 57 increase in intensity. Methyl and ethyl radical production increases significantly at 1060 K as indicated by the sharp increase in the intensity of m/e 15 and

m/e 29. This appears to be the onset of significant secondary decomposition of n-propyl and n-butyl radicals also observed in n-butyl and n-pentyl pyrolysis.

$$\dot{C}_4H_9 \rightarrow \dot{C}_2H_5 + C_2H_4 \qquad (5.4)$$

$$\dot{C}_3H_7 \rightarrow \dot{C}H_3 + C_2H_4 \qquad (5.5)$$

Methyl and ethyl radical production due to reaction 5.4 and 5.5 becomes increasingly significant at higher temperatures. The peak at m/e 15 doubles at each temperature increase from 1160 K to 1220 K, 1310 K, and 1420 K. Significant increases in the intensity of m/e 29 are also observed along with the appearance of m/e 28 at 1220 K as decreasing cooling efficiency leaves enough internal energy in C_2H_4 products to allow a fraction of them to become ionized and detected. The m/e 28 peak triples in intensity from 1220 K to 1310 K and again from 1310 K to 1420 K.

Peaks at m/e 43 and 57 stay approximately constant as the temperature is increased from 1160 K to 1310K and drop slightly at 1420 K as $\dot{C}_3H_7$ and $\dot{C}_4H_9$ and are produced in greater quantities by n-pentane decomposition and also consumed in secondary reactions. Peaks at m/e 42 and 56 increase significantly in intensity indicating significant loss of H atom from $\dot{C}_3H_7$ and $\dot{C}_4H_9$, respectively. At 1310 K, peaks at m/e 42 and 56 are significantly larger than the respective m/e 43 and 57 peaks and the peak intensity ratio of m/e 42 to m/e 56 is 4:1. H_2 elimination from C_3H_6 and C_4H_8 subsequent to loss of H atom from the propyl and butyl radicals is also observed at 1420 K resulting in peaks at m/e 40 and 54. H_2 elimination from $\dot{C}_3H_7$ to form of $\dot{C}_3H_5$, propenyl radical, is also observed at 1420K. Similarly, a very small fraction of ethenyl radical, $\dot{C}_2H_3$ is

formed from ethyl radical resulting in a small peak at m/e 27. H_2 elimination from the parent C_5H_{12} occurs to a very limited extent at 1310 K and 1420 K resulting in a very low intensity peak at m/e 70.

(b) Pyrolysis of n-hexane

Mass spectra for the pyrolysis of n-hexane at pyrolysis temperatures 610 K to 1410 K are shown in Figure 5.2. The parent, C_6H_{14} is indicated by the large peak at m/e 86. Peaks appear at m/e 29, 41, 42, 43, 56, and 57 with the m/e 43 peak being significantly larger than the others. These peaks are the results of photionization fragmentation (PIF) of C_6H_{14} producing $C_2H_5^{+\bullet}$, $C_3H_5^{+\bullet}$, $C_3H_6^{+\bullet}$, $C_3H_7^{+\bullet}$, $C_4H_8^{+\bullet}$, $C_4H_9^{+\bullet}$, respectively. PIF is noticeably reduced as the temperature is raised and thermal decomposition begins to occur.

The onset of pyrolysis appears between 870 K and 1020 K as the intensities of peaks at m/e 29, 42, 43 and 57 increase slightly. Increase in the intensity of m/e 43 is due to cleavage of the central C-C bond in hexane producing two propyl radicals. These undergo rapid loss of H atom via reaction 5.2, to form C_3H_6 which is responsible for m/e 42. Peaks at m/e 29 and 57 result from bond homolysis at the second C-C bond producing ethyl and butyl radicals.

$$C_6H_{14} \rightarrow {}^{\bullet}C_3H_7 + {}^{\bullet}C_3H_7 \qquad (5.6)$$

$$C_6H_{14} \rightarrow {}^{\bullet}C_2H_5 + {}^{\bullet}C_4H_9 \qquad (5.7)$$

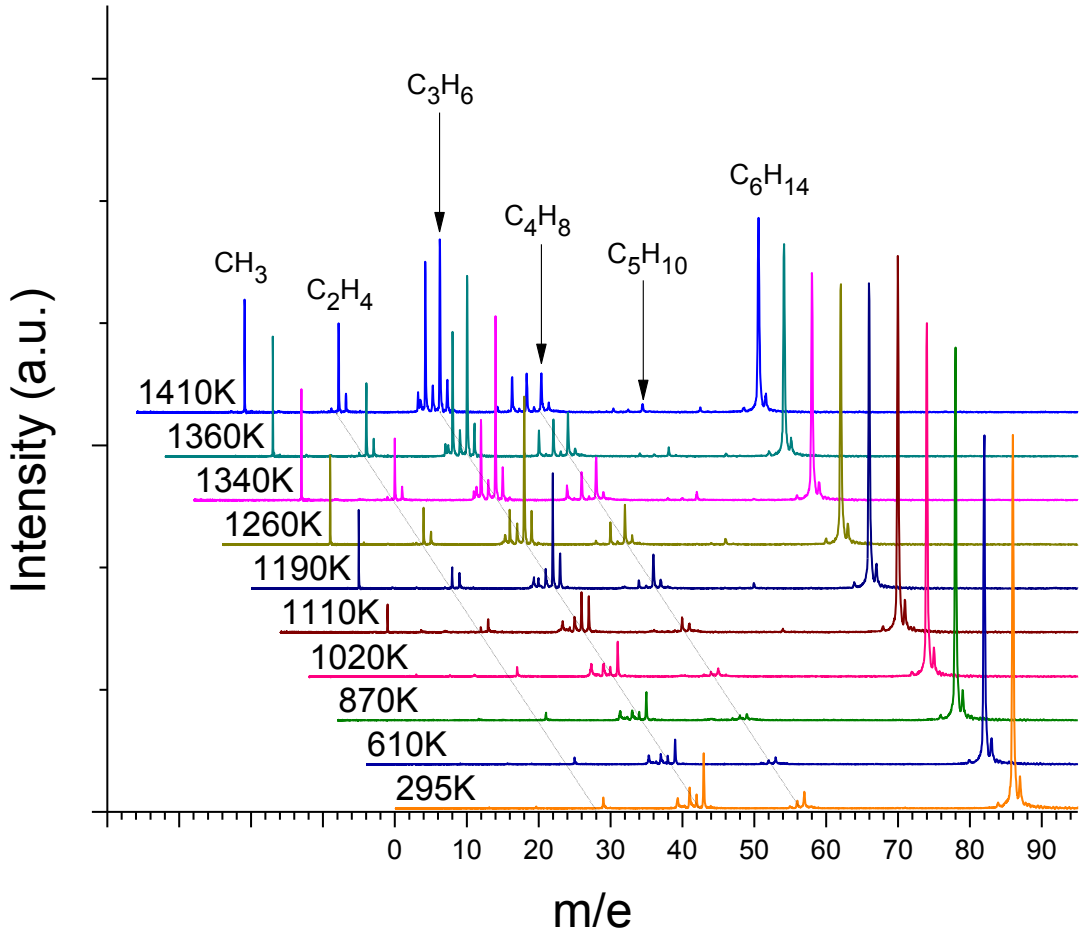

Figure 5.2 Stack plot of mass spectra for pyrolysis of n-hexane (~1%) in He at room temperature and pyrolysis temperatures 610 K to 1410 K. Mass spectra are offset for clarity.

At 1110 K, the intensity of m/e 36 grows significantly indicating a significantly increased production of C_3H_6. A peak is also observed at m/e 56 due to loss of H atom from $^{\bullet}C_4H_9$ produced via reaction 5.7. There is also a slight increase in intensity of m/e 29, due to $^{\bullet}C_2H_5$ also produced via reaction 5.7. A significant peak also appears at m/e 15 with intensity approximately 70 % of that of m/e 42 due to methyl radical. Methyl radical does not appear to be due to primary decomposition of hexane as this would also result in the production of $^{\bullet}C_5H_{11}$ but no peaks are observed in the region of m/e 71. Considering the significant production of $^{\bullet}C_3H_7$ and C_3H_6 at this temperature, methyl is likely produced by secondary loss of methyl radical from propyl radical by reaction 5.5.

Products of the secondary decomposition of $^{\bullet}C_3H_7$ rise significantly at 1190 K indicated by the quadrupling of the intensities of m/e 15 and m/e 42 relative to the intensities at 1110 K. The intensity of m/e 56, with intensity approximately 20% that of m/e 42, also increases significantly as a result of increased $^{\bullet}C_4H_9$ production. Elimination of H_2 from C_4H_8 is also observed resulting in a small peak at m/e 54, C_4H_6.

A peak also appears at m/e 28 at 1190 K as increased pyrolysis temperatures result in less efficient cooling leaving a fraction of C_2H_4 products with enough internal energy to be ionized. A very small fraction of n-hexane molecules undergoes H_2 elimination resulting in peak at m/e 84 that rises just above the baseline. A small peak can also be seen at m/e 70 resulting from C_5H_{10} produced by loss of methyl from hexane and subsequent ejection of H atom.

$$C_6H_{14} \rightarrow {}^{\bullet}CH_3 + {}^{\bullet}C_5H_{11} \qquad (5.8)$$

At 1260 K, peaks at m/e 15, 42, and 56 due to CH_3, C_3H_6, and C_4H_8 increase slightly in intensity. Increased ionization and detection of C_2H_4 results in a doubling of the intensity of m/e 28. The peak at m/e 54 due to C_4H_6, rises sharply indicating increased elimination of H_2 from C_4H_8. Elimination of H_2 from C_3H_6 and $^{\bullet}C_3H_7$ is also observed as peaks at m/e 40 and 41 corresponding to C_3H_4 and $^{\bullet}C_3H_5$, respectively. All other peaks maintain approximately the same intensity at 1260 K.

Secondary H_2 elimination reactions become increasingly prevalent at the highest pyrolysis temperatures, 1340 K to 1410 K. The intensities of m/e 40 and 54 steadily increase with increased temperatures as a result of H_2 elimination from C_3H_6 and C_4H_8 producing C_3H_4 and C_4H_6. At 1340 K and above, a peak is also observed at m/e 52 due to further H_2 elimination from C_4H_6.

(c) Pyrolysis of n-heptane

Mass spectra for pyrolysis of n-heptane (~1%) in He at room temperature and pyrolysis temperatures 660 K to 1590 K are shown in Figure 5.3. The large peak at m/e 100 corresponds to the parent, C_7H_{16}. Peaks at lower masses are observed in the room temperature spectrum due to PIF of the parent. Small peaks at m/e 41, 42, 55, 56, and 57 represent $C_3H_5^{+\bullet}$, $C_3H_6^{+\bullet}$, $C_3H_7^{+\bullet}$, $C_4H_7^{+\bullet}$, $C_4H_8^{+\bullet}$, and $C_4H_9^{+\bullet}$ respectively. The large peak at m/e 43 is due to the photoionization fragment $C_3H_7^{+\bullet}$. As the pyrolysis temperature is increased, thermal decomposition happens prior to ionization and the contribution of PIF to peak intensities is reduced.

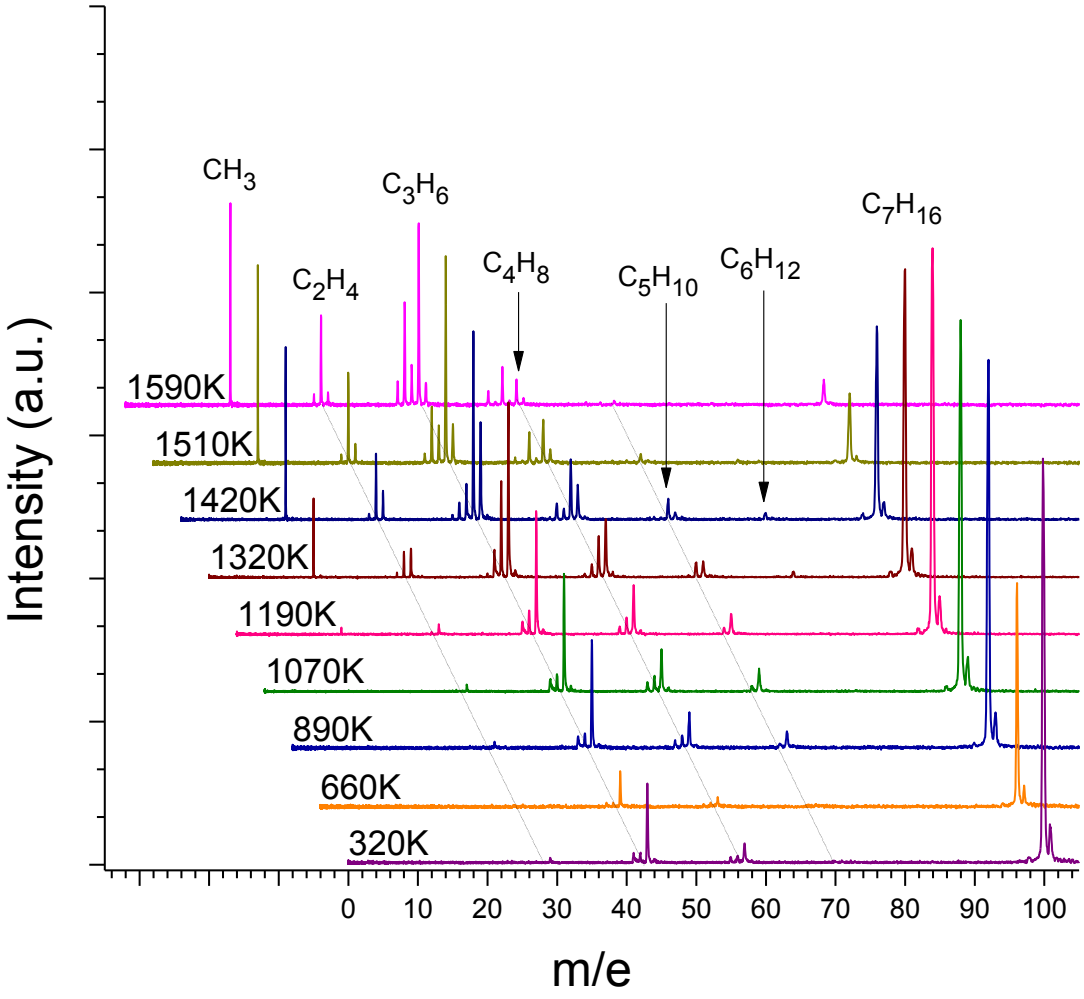

Figure 5.3 Stack plot of mass spectra for pyrolysis of n-heptane (~1%) in He at room temperature and pyrolysis temperatures 660 K to 1590 K. Mass spectra are offset for clarity.

The onset of C_7H_{16} pyrolysis occurs between 890 K and 1070K where intensities of peaks at m/e 42, 43, 56 and 57 are observed to increase. Peaks at m/e 43 and m/e 57 are due to propyl and butyl radicals, $^{\bullet}C_3H_7$ and $^{\bullet}C_4H_9$ produced upon C-C bond homolysis in C_7H_{16} as shown below in reaction 5.9. Peaks at m/e 42 and m/e 56 correspond to C_3H_6 and C_4H_8 produced by the rapid ejection of H atom from $^{\bullet}C_3H_7$ and $^{\bullet}C_4H_9$ as previously described. Small peaks are also observed at m/e 29 and m/e 51 due to C-C bond homolysis at the second bond in the n-heptane chain to produce $^{\bullet}C_2H_5$ and $^{\bullet}C_5H_{11}$ as shown in reaction 5.10 below. A peak at m/e 70 is also seen at 1070 K as C_5H_{10} is produced upon loss of H atom from $^{\bullet}C_5H_{11}$.

$$C_7H_{16} \rightarrow {}^{\bullet}C_3H_7 + {}^{\bullet}C_4H_9 \qquad (5.9)$$

$$C_7H_{16} \rightarrow {}^{\bullet}C_2H_5 + {}^{\bullet}C_5H_{11} \qquad (5.10)$$

According to reaction 5.9, $^{\bullet}C_3H_7$ and $^{\bullet}C_4H_9$ should be produced in a one to one ratio. Assuming similar ionization cross sections, the intensities of the peaks at m/e 57 and m/e 43 should be approximately equal. These results indicate that the β-scission of $^{\bullet}C_4H_9$ to produce ethyl radical and ethene (which is not detected at this temperature) occurs significantly more rapidly than decomposition of $^{\bullet}C_3H_7$. Rapid β-scission of $^{\bullet}C_5H_{11}$ to produce $^{\bullet}C_3H_7$ and ethene may also explain the relatively large m/e 43 peak.

At 1190 K, all aforementioned product peaks increase slightly in intensity. Peaks at m/e 42 and 56 reach approximately 10 % of the intensity of m/e 43 and 56 respectively indicating slightly increased secondary loss of H atom from $^{\bullet}C_3H_7$ and $^{\bullet}C_4H_9$. A small peak is also observed at m/e 15 indicating the production of methyl radical. Homolysis of

the first C-C bond would produce $^{\bullet}CH_3$ and $^{\bullet}C_6H_{13}$ but no corresponding peak is observed at m/e 85. Secondary decomposition of $^{\bullet}C_3H_7$ by reaction 5.4 likely contributes significantly to methyl production in this system.

At 1320 K, $^{\bullet}C_3H_7$ and $^{\bullet}C_4H_9$ production increases significantly as indicated by increasing intensities of peaks at m/e 42, 43, 56, and 57. Peaks at m/e 43 and m/e 57 increase by 40 % and 20 %, respectively. Peaks at m/e 42 and 56 increase in intensity by a factor of 5. Significant elimination of H_2 from $^{\bullet}C_3H_7$ is also observed resulting in a significant increase in the intensity of m/e 41 due to $^{\bullet}C_3H_5$ with intensity 20 % that of m/e 42. The peak at m/e 71 drops slightly in intensity while m/e 70 increases to approximately the same intensity as m/e 71, indicating increased, though still relatively small, production of $^{\bullet}C_5H_{11}$ and C_5H_{10}. Small peaks at m/e 84 and 85, just above the baseline correspond to small fractions of $^{\bullet}C_6H_{13}$ and C_6H_{12} produced by loss of methyl from heptane and subsequent ejection of H atoms from $^{\bullet}C_6H_{13}$.

$$C_7H_{16} \rightarrow {}^{\bullet}CH_3 + {}^{\bullet}C_6H_{13} \qquad (5.11)$$

Secondary decomposition of $^{\bullet}C_3H_7$ and $^{\bullet}C_4H_9$ results in significant increases in the production of methyl and ethyl radicals as indicated by the sharp increase in the intensities of m/e 15 and m/e 29 from 1190 K to 1320 K. In addition, a peak at m/e 28 is also observed as incomplete cooling of ethene allows ionization and detection of a fraction of the ethene products at high pyrolysis temperatures.

Secondary reactions become increasingly significant at 1420 K. Intensities of peaks at m/e 43, 57, and 71 drop significantly while those at m/e 42, 56, and 70 rise

sharply indicating significant H atom loss from $^{\bullet}C_3H_7$, $^{\bullet}C_4H_9$, $^{\bullet}C_5H_{11}$ produced by n-heptane decomposition. C_3H_6 and C_4H_8, produced from these reactions undergo H_2 elimination resulting in small peaks at m/e 40 and 54 due to C_3H_4 and C_4H_6, respectively. Peaks at m/e 15 and m/e 28 increase in intensity by a factor of 2.5.

At 1510 K and 1590 K, m/e 43, 57, and 71 continue to fall in intensity due to secondary decomposition of $^{\bullet}C_3H_7$, $^{\bullet}C_4H_9$, and $^{\bullet}C_5H_{11}$. Intensities of peaks at m/e 42, 56 drop slightly but m/e 40 and 54 steadily increase in intensity as more extensive H_2 elimination from C_3H_6 and C_4H_8 occurs. A peak appears at m/e 39 indicating production of propargyl radical by H_2 elimination from $^{\bullet}C_3H_5$. A small peak at m/e 52 appears at 1590 K corresponding to C_4H_4 formed upon H_2 elimination from C_4H_6.

(d) Pyrolysis of n-octane

Mass spectra for pyrolysis of n-octane (~1%) in He are shown in Figures 5.4 and 5.5. Figure 5.4 shows mass spectra for C_8H_{18} at room temperature and pyrolysis temperatures 540 K to 1140 K. The peak at m/e 114 is due to the parent C_8H_{18}. n-Octane undergoes significant PIF resulting in a number of peaks in the room temperature spectrum. Particularly large peaks are observed at m/e 43 and m/e 57 due to PIF resulting in the formation of $C_3H_7^{+\bullet}$ and $C_4H_9^{+\bullet}$, respectively. Unfortunately, the presence of these peaks makes it difficult to judge the extent of $^{\bullet}C_3H_7$ and $^{\bullet}C_4H_9$ production due to thermal decomposition processes at lower pyrolysis temperatures. Potential C-C bond homolysis pathways include the following.

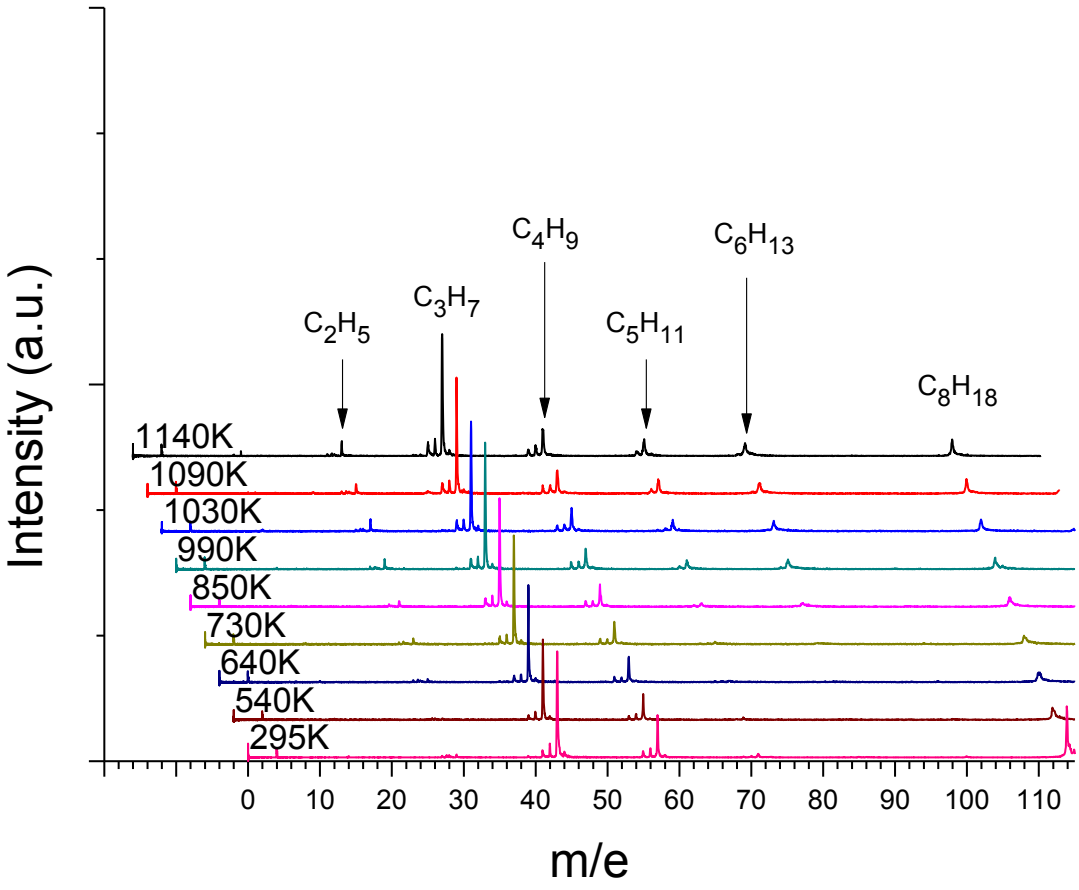

Figure 5.4 Stack plot of mass spectra for pyrolysis of n-octane (~1%) in He at room temperature and pyrolysis temperatures 540 K to 1140 K. Mass spectra are offset for clarity.

$$C_8H_{18} \rightarrow {}^{\bullet}CH_3 + {}^{\bullet}C_7H_{15} \quad (5.12)$$

$$C_8H_{18} \rightarrow {}^{\bullet}C_2H_5 + {}^{\bullet}C_6H_{13} \quad (5.13)$$

$$C_8H_{18} \rightarrow {}^{\bullet}C_3H_7 + {}^{\bullet}C_5H_{11} \quad (5.14)$$

$$C_8H_{18} \rightarrow {}^{\bullet}C_4H_9 + {}^{\bullet}C_4H_9 \quad (5.15)$$

${}^{\bullet}C_3H_7$ and ${}^{\bullet}C_4H_9$ are important products. Given that ${}^{\bullet}C_3H_7$ and ${}^{\bullet}C_4H_9$ have been observed to undergo extensive loss of H atom to produce C_3H_6 and C_4H_8, monitoring peaks at m/e 42 and 56 can give some indication of ${}^{\bullet}C_3H_7$ and ${}^{\bullet}C_4H_9$ production. In addition, the production of ${}^{\bullet}C_3H_7$ is accompanied by that of ${}^{\bullet}C_5H_{11}$ which is not obscured by PIF peaks. Small peaks at m/e 41, 42, 55, and 56 due to $C_3H_5^{+\bullet}$, $C_3H_6^{+\bullet}$, $C_4H_7^{+\bullet}$, and $C_4H_8^{+\bullet}$ are also observed in the room temperature spectrum.

Intensities of peaks at m/e 41-43 and m/e 55-57 stay relatively constant up to 850 K so it is relatively safe to assume that further increases in the intensity of peaks at slightly higher temperatures 1030 K and 1090 K are the result of thermal decomposition processes in addition to the PIF observed at lower temperatures. The intensity of m/e 43 increases slightly at 990 K with a concomitant appearance of a peak at m/e 71. These peaks represent ${}^{\bullet}C_3H_7$ and ${}^{\bullet}C_5H_{11}$ produced by reaction 5.14. Peaks at m/e 29 and m/e 85 with intensities slightly smaller than that of m/e 71 are observed indicating production of ${}^{\bullet}C_2H_5$ and ${}^{\bullet}C_6H_{13}$ by reaction 5.13. A slight increase in the intensity of m/e 57 is observed at 1030 K corresponding to ${}^{\bullet}C_4H_9$ from reaction 5.15. Intensities of all aforementioned

product peaks increase proportionally as the temperature is raised to 1140 K. Peaks at m/e 41, 42, and 56 due to C_3H_5, C_3H_6, and C_4H_8 also increase slightly in intensity.

Mass spectra for pyrolysis of n-octane (~1%) in He at pyrolysis temperatures 1190 K to 1500 K are shown in Figure 5.5. Slight increases in the intensities of peaks corresponding to primary decomposition products $^{\bullet}C_2H_5$, $^{\bullet}C_3H_7$, $^{\bullet}C_4H_9$, $^{\bullet}C_5H_{11}$, and $^{\bullet}C_6H_{13}$ continue as the temperature is raised to 1190 K and up to 1340 K. Significant increases in intensities of peaks due to secondary products, specifically those due to loss of H from $^{\bullet}C_3H_7$, $^{\bullet}C_4H_9$, and $^{\bullet}C_5H_{11,}$ is observed. The peak at m/e 42, corresponding to C_3H_6, steadily grows from approximately 5% of the intensity of m/e 43 at 1190 K to 90 % at 1340 K. Similarly the peak at m/e 56, corresponding to C_4H_8, steadily increases in intensity from 10 % of that of m/e 57 to 50% from 1190 K to 1340 K. A small peak at m/e 70 due to C_5H_{10} is observed at 1230 K and above. Secondary elimination of H_2 from $^{\bullet}C_3H_7$ is also observed as a steady increase in the intensity of m/e 41 corresponding to $^{\bullet}C_3H_5$ from 1190 K to 1340 K.

At 1190 K, a m/e 15 peak indicates methyl production due to secondary reactions as no peaks are observed in the m/e 99 region that might indicate $^{\bullet}C_7H_{15}$ production from reaction 5.12. M/e 15 increases sharply in intensity from 1190 K to 1340 K becoming the highest intensity peak. Decomposition of C_3H_7 via reaction 5.5 contributes significantly to methyl production. Ethene is detected at 1260 K and above appearing as a peak at m/e 28 steadily increasing in intensity at higher temperatures with intensity 70 % of that of m/e 29 at 1340 K.

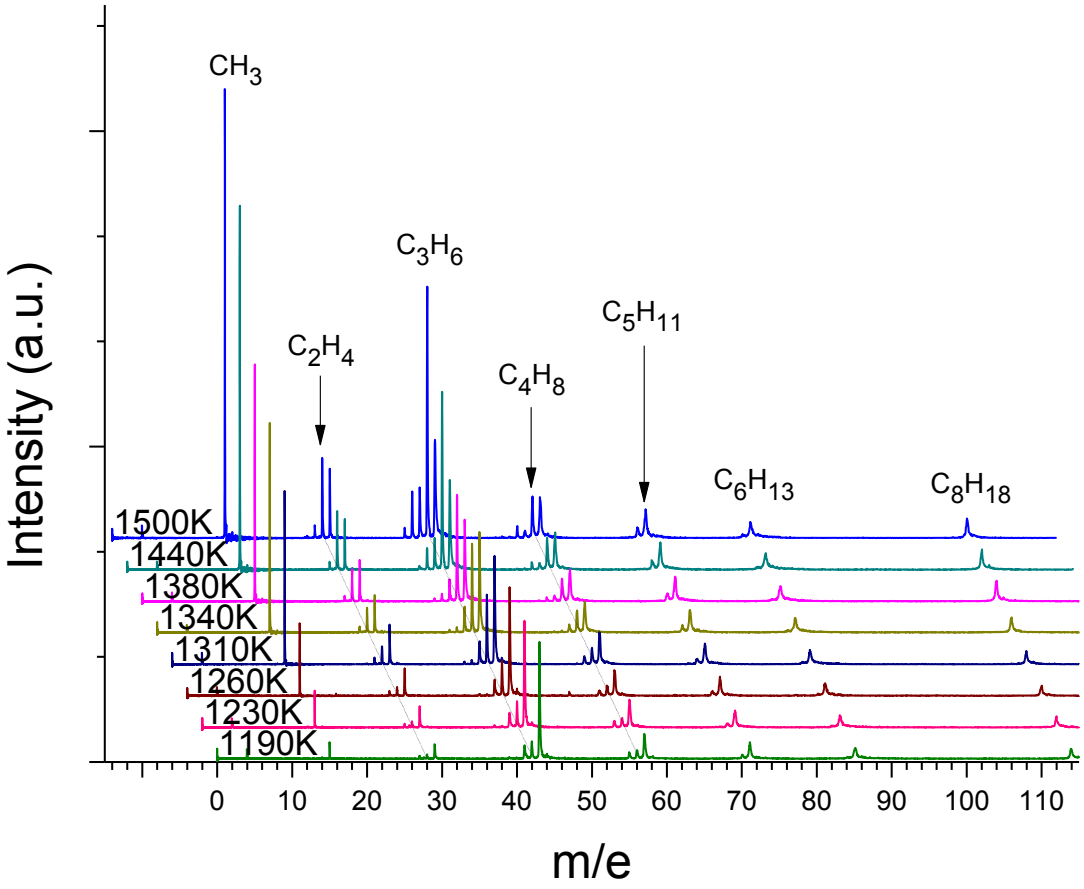

Figure 5.5 Stack plot of mass spectra for pyrolysis of n-octane (~1%) in He at pyrolysis temperatures 1190 K to 1500 K. Mass spectra are offset for clarity.

At 1380 K, m/e 43 begins to fall in intensity as $^{\bullet}C_3H_7$ is further consumed by secondary reactions. Intensities of peaks corresponding to its decomposition products $^{\bullet}CH_3$, C_2H_4, and C_3H_6 increase significantly. Intensities of all other product peaks increase nominally. The intensity of m/e 42 due to C_3H_6 increases substantially at the highest temperatures, 1440 K and 1500 K. As in the pyrolysis of other alkanes, elimination of H_2 from C_3H_6, $^{\bullet}C_3H_7$, and C_4H_8 occurs in this temperature range. Peaks are observed at m/e 41, 42, and 55 corresponding to C_3H_4, $^{\bullet}C_3H_5$, and C_4H_6 produced by these reactions at 1440K. Their intensities increase at 1500K. Secondary reactions also produce significant amounts of $^{\bullet}CH_3$, C_2H_4, and $^{\bullet}C_2H_5$ resulting in significant increases in the intensities of m/e 15, 28, and 29 at 1440 K and 1500 K.

(e) Pyrolysis of n-decane

Mass spectra for pyrolysis of n-decane (~1%) in Ar are shown in Figures 5.6 and 5.7. Figure 5.6 shows mass spectra for $C_{10}H_{22}$ at room temperature and pyrolysis temperatures 760 K to 1190 K. The peak at m/e 142 is due to the parent $C_{10}H_{22}$. Ar was used as the carrier gas to efficiently cool the sample and limit PIF. Nevertheless, significant PIF is observed and peaks at m/e 43, 57, 71, and 84 in the room temperature spectrum represent PIF of $C_{10}H_{22}$ to form $C_3H_7^{+\bullet}$, $C_4H_9^{+\bullet}$, $C_5H_{11}^{+\bullet}$, and $C_6H_{12}^{+\bullet}$, respectively. In addition, a broad peak at m/e 39-40 is observed due to electron impact ionization of the carrier gas, Ar. Unfortunately, this peak obscures some peaks in this mass range.

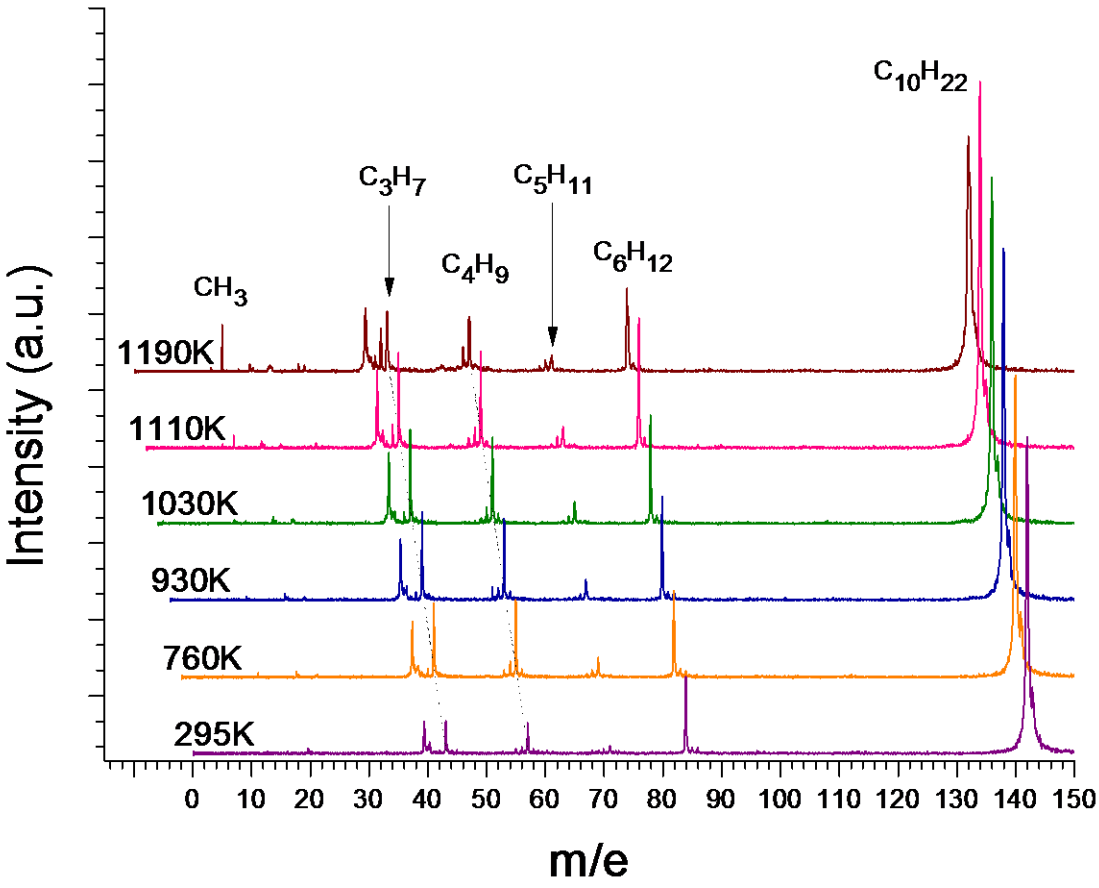

Figure 5.6 Stack plot of mass spectra for pyrolysis of n-decane (~1%) in Ar at room temperature and pyrolysis temperatures 760 K to 1190 K. Mass spectra are offset for clarity.

Due to the significant PIF, the extent of thermal decomposition at low temperatures is difficult to judge. Assuming, efficient cooling of molecules at moderate temperatures, PIF should not increase significantly so further increases in intensity can be attributed to thermal decomposition processes. At 760 K, peaks at m/e 43, 57, and 71 increase significantly in intensity while the peak at m/e 84 maintains a constant intensity. These peaks suggest thermal decomposition of $C_{10}H_{22}$ to produce $^{\bullet}C_3H_7$, $^{\bullet}C_4H_9$, $^{\bullet}C_5H_{11}$ by the following processes.

$$C_{10}H_{22} \rightarrow {}^{\bullet}C_3H_7 + {}^{\bullet}C_7H_{15} \qquad (5.16)$$

$$C_{10}H_{22} \rightarrow {}^{\bullet}C_4H_9 + {}^{\bullet}C_6H_{13} \qquad (5.17)$$

$$C_8H_{18} \rightarrow {}^{\bullet}C_5H_{11} + {}^{\bullet}C_5H_{11} \qquad (5.18)$$

Peaks at m/e 85 and m/e 99 are noticeably absent. These larger radicals appear to undergo β-scission faster than the sampling time scale, producing smaller radicals and ethene which is not detected at these modest temperatures.

$$^{\bullet}C_7H_{15} \rightarrow {}^{\bullet}C_5H_{11} + C_2H_4 \qquad (5.19)$$

$$^{\bullet}C_6H_{13} \rightarrow {}^{\bullet}C_4H_9 + C_2H_4 \qquad (5.20)$$

A small peak is observed at m/e 56 due to C_4H_8 produced by ejection of H atoms from $^{\bullet}C_4H_9$.

The intensities of peaks at m/e 43, 57, 71, and 84 increase slightly at 930 K. The production of C_6H_{12}, indicated by the m/e 84 peak, appears to be produced by loss of H

atom from $^{\bullet}C_6H_{13}$ rather than molecular decomposition of $C_{10}H_{22}$. Molecular decomposition to C_6H_{12} would also produce C_4H_{10} but no peak at m/e 58 is observed. Peaks at m/e 43, 57, 71, and 84 increase further in intensity as the pyrolysis temperature is increased from 930 K up to 1190 K. Loss of H atom from $^{\bullet}C_3H_7$ and $^{\bullet}C_5H_{11}$ radicals occurs at these temperatures. At 1030 K, peaks appear at m/e 36 and m/e 70 as a result of C_3H_6 and C_5H_{10}, respectively. These peaks steadily increase in intensity with increasing temperature reaching 80 % of the intensity of m/e 37 and m/e 71 at 1190 K. Production of C_4H_8 also increases as m/e 56 grows to 30 % of the intensity of m/e 57 at 1190 K. A small peak at m/e 15 appears at 1110 K and increases significantly in intensity at 1190 K indicating production of methyl radical, $^{\bullet}CH_3$. Methyl radical could be produced by loss of methyl from the parent $C_{10}H_{22}$ due to C-C bond fission but more likely is primarily the result of $^{\bullet}C_3H_7$ decomposition to methyl radical and ethene as observed in the decomposition of other n-alkanes.

Mass spectra for pyrolysis of n-decane (~1%) in Ar at pyrolysis temperatures 1260 K to 1510 K are shown in figure 5.7. Peaks at m/e 43, 57, and 71 increase slightly in intensity from 1260 to 1510 K due to continued decomposition of $C_{10}H_{22}$ by reactions 5.16, 5.17, and 5.18 to form $^{\bullet}C_3H_7$, $^{\bullet}C_4H_9$, and $^{\bullet}C_5H_{11}$. Peaks at m/e 56 and 70 increase proportionally to m/e 57 and m/e 71 due to loss of H from $^{\bullet}C_4H_9$ and $^{\bullet}C_5H_{11}$. The peak at m/e 42 due to C_3H_6 is 20 % more intense than m/e 43 at 1260 K and steadily grows to 60 % larger intensity than m/e 43 at 1470 K and 1510 K. The peak at m/e 84 grows slowly across the temperature range 1260 K to 1510 K as a result of $C_{10}H_{22}$ decomposition with subsequent loss of H atom from $^{\bullet}C_6H_{13}$. A small peak appears at m/e 28 due to ethene at

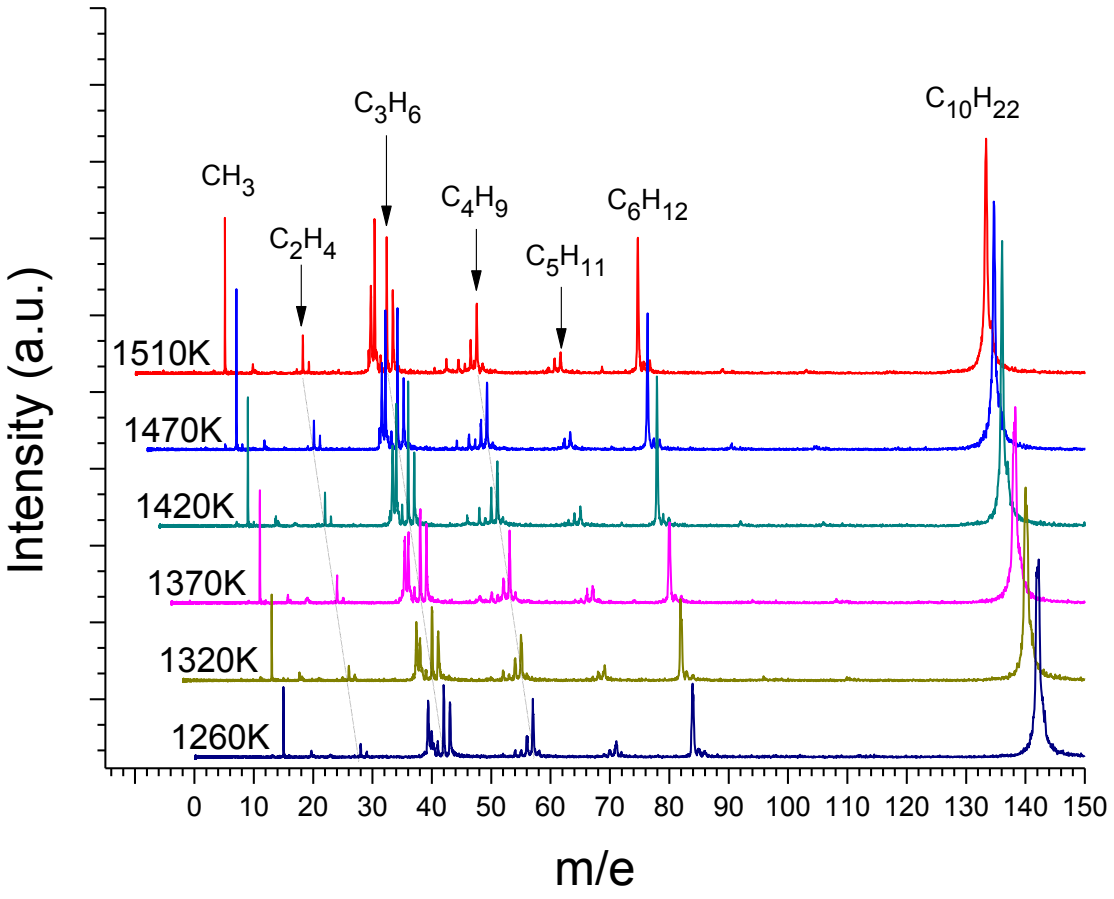

Figure 5.7 Stack plot of mass spectra for pyrolysis of n-decane (~1%) in Ar at pyrolysis temperatures 1260 K to 1510 K. Mass spectra are offset for clarity.

1260 K where a fraction of ethene molecules can be ionized and detected. A small peak is also observed at m/e 29. These peaks increase in intensity to a limited extent from 1260 K to 1510 K. Notably, the intensity of m/e 29 is small at all temperatures suggesting significant formation of ethene by β-scission of larger radicals rather than H loss from ethyl radical.

Peaks at m/e 40 and 54 appear at 1320 K due to H_2 elimination from C_3H_6 and C_4H_8 respectively. M/e 54 steadily increases by approximately 10% with each temperature increase at 1370 K, 1420 K, and 1470K where it is 15 % of the intensity of m/e 57. The peak at m/e 40 is partially obscured by the broad peak at m/e 39-40 resulting from electron impact ionization of Ar, but grows significantly as the temperature is increased becoming equal in intensity to m/e 37 at 1370 K and double the intensity of m/e 37 at 1470 K and 1510 K. The intensity of m/e 15 is approximately the same as that of m/e 40 across this temperature range indicating significant secondary decomposition of $^{\bullet}C_3H_7$.

5.4 Discussion

Heavy production of $^{\bullet}C_3H_7$ and C_3H_6 is observed in all of the pyrolysis results, particularly at higher temperatures. For the pyrolysis of n-heptane, n-octane, and n-decane significant fractions of C_4, C_5, and C_7 products would necessarily accompany the production of $^{\bullet}C_3H_7$ and C_3H_6 but are only observed in limited quantities. It seems clear that these larger radicals, particularly those containing 5 or more carbon atoms,

decompose rapidly producing smaller radicals and olefins. This is consistent with observations on the decomposition of 1-pentyl radical rapidly decomposing by β-scission to form propyl radical and ethene.

$$CH_2CH_2{-}CH_2CH_2CH_3 \rightarrow C_2H_4 + {}^{\bullet}C_3H_7 \qquad (5.21)$$

Unfortunately, this rapid secondary decomposition of large radicals combined with rapid decomposition of ethyl radical to H atoms and ethene (which is not readily detected in this system), make accurate judgment of initial C-C bond fission branching ratios difficult. However, it is clear that for the pyrolysis of all n-alkanes studied here significant decomposition occurs before the appearance of methyl radical. Thus it can be concluded that loss of methyl radical from n-alkanes is least significant in alkane pyrolysis.

At high pyrolysis temperatures, significant quantities of C_3H_4, C_3H_5, C_3H_6, C_4H_6 and C_4H_8 are observed in the pyrolysis of all n-alkanes in this study. According to the generally accepted Rice-Herzfeld mechanism, alkyl radicals primarily decompose by β-scission but significant quantities of ${}^{\bullet}C_3H_7$ and ${}^{\bullet}C_4H_9$ eject hydrogen atom and undergo H_2 elimination as well.

$${}^{\bullet}C_3H_7 \rightarrow C_3H_6 + {}^{\bullet}H \rightarrow C_3H_4 + H_2 + {}^{\bullet}H \qquad (5.22)$$

$${}^{\bullet}C_3H_7 \rightarrow {}^{\bullet}C_3H_5 + H_2 \qquad (5.23)$$

$${}^{\bullet}C_4H_9 \rightarrow C_4H_8 + H \rightarrow C_4H_6 + H_2 + {}^{\bullet}H \rightarrow C_4H_4 + 2\,H_2 + {}^{\bullet}H \qquad (5.24)$$

Kinetic models of alkane pyrolysis may need to be adjusted to account for the importance of these H_2 elimination pathways.

5.5 Conclusion

Flash pyrolysis VUV-PI-TOFMS was performed on n-pentane, n-hexane, n-heptane, n-octane, and n-decane. The formation of free radicals from C-C bond fission is observed for all alkanes. Homolysis of the α C-C bond is the least significant C-C bond homolysis pathway. Radicals containing five or more carbons undergo rapid β-scission reactions to form smaller radicals and olefins. Significant fractions of $^{\bullet}C_3H_7$ and $^{\bullet}C_4H_9$ radicals produced by alkane pyrolysis undergo loss of H atom followed by H_2 elimination. Elimination of H_2 from $^{\bullet}C_3H_7$ to form $^{\bullet}C_3H_5$ is also observed.

References

(1) Balaban, A. T. *Pure and Applied Chemistry* **1983**, *55*, 199–206.

(2) Rice, F. *Journal of the American Chemical Society* **1931**, *53*, 1959.

(3) Rice, F.; Herzfeld, K. *Journal of the American Chemical Society* **1934**, *1262*, 284–289.

(4) Kossiakoff, A.; Rice, F. *Journal of the American Chemical Society* **1943**, *65*, 590–595.

(5) Burk, R. E.; Laskowski, L.; Lankelma, H. P. *Journal of the American Chemical Society* **1941**, *63*, 3248–3250.

(6) Doue, F.; Guiochon, G. *The Journal of Physical Chemistry* **1969**, *73*, 2804–2809.

(7) Kunzru, D.; Shah, Y. T.; Stuart, E. B. *Industrial & Engineering Chemistry Process Design and Development* **1972**, *11*, 605–612.

(8) Allara, D. L.; Edelson, D. *International Journal of Chemical Kinetics* **1975**, *VII*, 479–507.

(9) Ebert, K. H.; Ederer, H. J.; Isbarn, G. *International Journal of Chemical Kinetics* **1983**, *15*, 475–502.

(10) Billaud, F.; Freund, E. *Industrial & Engineering Chemistry Fundamentals* **1986**, *25*, 433–443.

(11) Imbert, F. E.; Marshall, R. M. *International Journal of Chemical Kinetics* **1987**, *19*, 81–103.

(12) Dominef, F. *Energy & Fuels* **1989**, *3*, 89–96.

(13) Safarik, I.; Strausz, O. P. *Research on Chemical Intermediates* **1996**, *22*, 275–314.

(14) Curran, H. J.; Gaffuri, P.; Pitz, W. J.; Westbrook, C. K. *Combustion and Flame* **1998**, *114*, 149–177.

(15) Savage, P. E. *Journal of Analytical and Applied Pyrolysis* **2000**, *54*, 109–126.

(16) Hunter, K. C.; East, A. L. L. *The Journal of Physical Chemistry A* **2002**, *106*, 1346–1356.

(17) Yuan, T.; Zhang, L.; Zhou, Z.; Xie, M.; Ye, L.; Qi, F. *The Journal of Physical Chemistry A* **2011**, *115*, 1593–601.

(18) Ding, J.; Zhang, L.; Zhang, Y.; Han, K. L. *The Journal of Physical Chemistry A* **2013**, *117*, 3266–78.

(19) Chambreau, S. D.; Zhang, J. *Chemical Physics Letters* **2001**, *343*, 482–488.

CHAPTER 6

Pyrolysis of Silane and Germane Mixture

6.1 Introduction

There has been significant interest in the growth of polycrystalline $Si_{1-x}Ge_x$ thin films since the early 1990s when they were first applied to Si-based heterojunction bipolar transistors providing improved current gain performance over poly-Si transistors and the ability for band gap tuning.[1,2] More recently, $Si_{1-x}Ge_x$ has been shown to have promising applications in modulation doped field effect transistors (MODFET)[3], strained-Si complementary metal-oxide semiconductor filled effect transistors (MOSFET)[4,5], photodetectors[6], and active matrix liquid crystal displays (AMLCD).[7]

Chemical vapor deposition (CVD), using gas phase precursors such as silane (SiH_4) and germane (GeH_4), is a relatively low cost means of producing $Si_{1-x}Ge_x$ thin films. $Si_{1-x}Ge_x$ has been produced using a variety of CVD techniques including ultra-high vacuum CVD (UHVCVD)[8,9], low pressure CVD (LPCVD)[10-14], atmospheric pressure CVD (APCVD)[15,16], and rapid thermal CVD (RTCVD). [17,18] Secondary gas phase reactions are essentially negligible in UHVCVD processes but are quite significant in LPCVD and APCVD applications. However, the use of LPCVD and APCVD are preferable due to their lower cost and simpler instrumentation.

Although the kinetics of $Si_{1-x}Ge_x$ film growth have been widely studied, they are not yet well understood. Film growth rate and composition are dependent not just on relative concentration of silane and germane precursors but temperature and pressure as

well. [19] Thus, optimization of the growth procedure and selection of the appropriate CVD technique continues to be a subject of active research. Indeed, much recent work has been devoted to finding a suitable kinetic model for the deposition of $Si_{1-x}Ge_x$ from silane and germane. [19-21]

An example of the relatively complex kinetics of $Si_{1-x}Ge_x$ deposition is that under low temperature (T= 400-600 ^{0}C) CVD conditions. In this temperature regime, film growth rate is known to decrease with increasing germane concentration thus limiting the incorporation of Ge into the film to approximately 35%.[22] It is supposed that the growth rate is not limited by adsorption of the growth species but by surface nucleation or gas phase kinetics.[22,23] Thus, a better understanding of gas phase silane and germane reactions at elevated temperatures is important to the optimization of CVD techniques.

Prior work in this lab has involved the characterization of highly unsaturated silicon and germane clusters, Si_xH_y (x=3-10, y=0-3) and Ge_xH_y (x=2-7) formed by flash pyrolysis of silane and germane, respectively, at 20 to 100 μs time scale.[24,25] In this work, the flash pyrolysis technique is used to directly observe initial reactive intermediates and primary pyrolysis products in a 1:1 silane and germane mixture thus providing insights into the early stages of gas phase reactions of the silane and germane mixture in CVD. Upon pyrolysis of silane and germane, highly unsaturated mixed clusters $Si_xGe_yH_z$ (x=1-3, y=1-5, z=0-4) are directly observed.

The observation and characterization of Si_xGe_y clusters is also of fundamental interest. An understanding of the structural, electronic, and thermodynamic properties of small heteronuclear clusters is an important step in characterizing the macroscopic

properties of bulk $Si_{1-x}Ge_x$. Synthesis of saturated $Si_xGe_yH_z$ compounds was first performed by Timms et al. in the early 1960s.[26] Three synthesis methods were used: hydrolysis of MgGeSi alloys, hydrolysis of SiO-GeO mixtures, and silent electric discharge on mixtures of disilane or trisilane and digermane. Mackay et al. studied the structural isomerism of Si_2GeH_8 and $SiGe_2H_8$ by combining NMR, IR and mass spectrometric detection with the silent electric-discharge synthesis method used by Timms and produced nearly equivalent amounts of each Si_2GeH_8 isomer but dominant amounts of the $SiH_3GeH_2GeH_3$ isomer of $SiGe_2H_8$.[27] Viswanathan later synthesized SiGe, Si_2Ge, $SiGe_2$, and Si_2Ge_2 from solid semiconductor-grade silicon and germanium powder by Kneudsen-effusion mass spectrometry and determined enthalpies of formation of these clusters.[28] The current study represents, to our knowledge, the first experimental observation of the mixed hydride clusters, $Si_xGe_yH_z$ (x=1-3, y=1-5, z=0-4), in the gas phase.

A number of theoretical studies have also been performed in order to elucidate the geometry and the energetics of unsaturated $Si_xGe_yH_z$ clusters. In 1999, Andriotis et al. studied the ground-state geometries of SiGe, Si_2Ge_2, Si_4Ge_2, and Si_2Ge_4 using a semi-empirical approach.[29] They concluded that the tetramer, Si_2Ge_2, has a planar rhombus structure and the hexamers an octahedral structure. Li et al. used a B3LYP-DFT method to identify minimum energy structures of select Si_xGe_y structures where $n = x + y \leq 10$ and found that these binary clusters have similar ground-state structures to corresponding Si_n and Ge_n clusters but with lower symmetries.[30] Marim et al. expanded the *ab initio* study performed by Li to include all possible structures where n = 3-5,7.[31] Bing et al. in a

very recent *ab initio* study conclude that the mixing energies of Si_xGe_y clusters is negative for the majority of clusters indicating that the binary clusters are generally more stable than pure Si and Ge clusters.[32] They note that, due to the particular stability of binary clusters $SiGe_2$, Si_2Ge_2, Si_2Ge_3, Si_2Ge_3, Si_2Ge_4, and Si_2Ge_5, these clusters should be readily produced experimentally.

6.2 Experimental

Pyrolysis experiments and Si-Ge cluster formation were conducted on a home-built vacuum ultraviolet (VUV) photoionization time-of-flight mass spectrometer (TOFMS) apparatus that has been previously described.[33-36] Silane (99.998%) was obtained from Matheson. Germane (99.997+%) was obtained from Aldrich Chemicals. All gas samples were used without further purification.

6.3 Results and Discussion

The pyrolysis products were monitored with nozzle temperatures varying from 800 K to 1780 K in approximately 100 K increments. At temperatures up to 1100 K, known silane and germane pyrolysis products were observed including SiH_2, Si_2H_4, Si_2H_2, Si, GeH_2, and Ge. The results were in agreement with the previously proposed silane and germane pyrolysis mechanisms.[25,34,37,38] Further details on the pyrolysis of silane and germane can be found in separate publications.[24,25,34] As in the previous studies, silicon and germanium clusters were also produced at temperatures above approximately 1100 K. Si_xH_z (x=1-4) and Ge_yH_z (y=0-6) were observed (Figure 6.1).

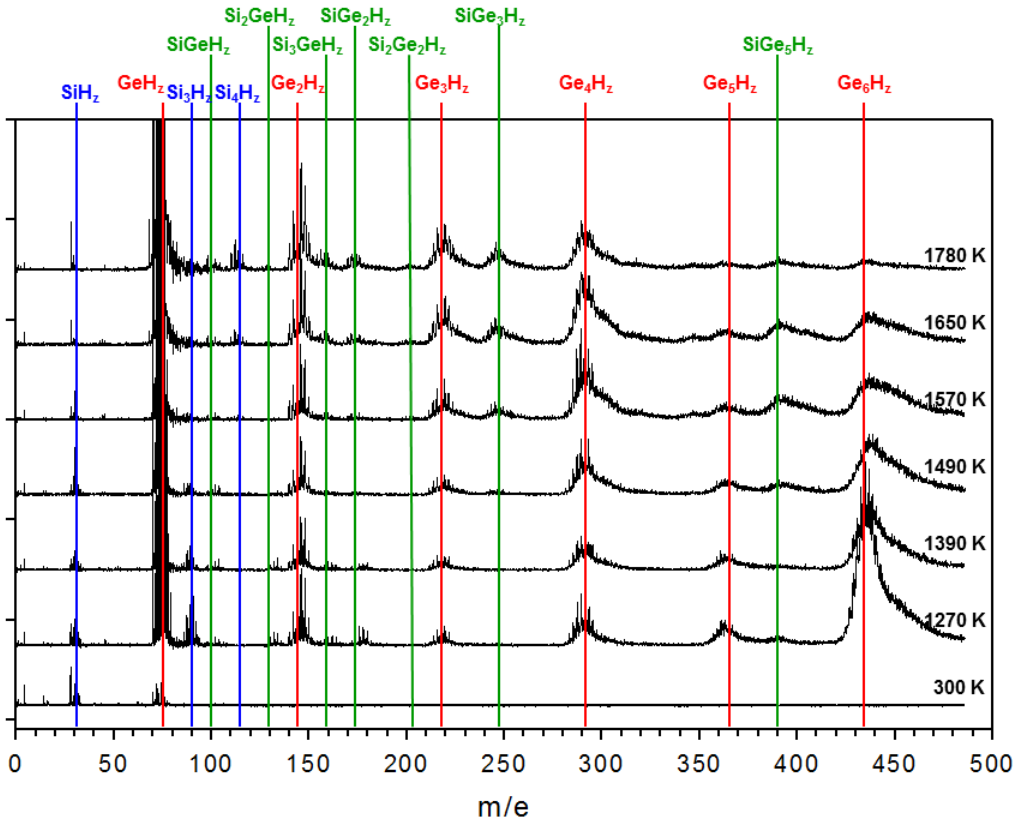

Figure 6.1 $Si_xGe_yH_z$ formation upon flash pyrolysis of silane and germane (2% each in He at 1.5 atm total backing pressure) between 1270 K and 1780 K, detected using 10.45eV photoionization/ TOFMS. Baselines of the mass spectra are offset for clarity.

Si_5H_z and Si_6H_z clusters may also have been produced but obscured by the significantly larger Ge_2H_z and $SiGe_2H_z$ peaks, respectively. Silicon and germanium mixed clusters began to appear at higher pyrolysis temperatures and were clearly detectable at pyrolysis temperatures 1270 K and above. Generally, germanium rich clusters were observed in greater quantities than silicon rich clusters. This is primarily due to the fact that the Ge-H bonds in germane are weaker than the Si-H bonds in silane.[25,34] Thus, the decomposition of germane was more favored. The results of silane and germane pyrolysis and Si/Ge mixed cluster production are shown in Figure 6.1 and in more detail in Figures 6.2-6.4.

Germanium exists in five stable isotopic forms ^{70}Ge (20.5%), ^{72}Ge (27.4%), ^{73}Ge (7.8%), ^{74}Ge (36.5%), and ^{76}Ge (7.8%). Silicon has three stable isotopes ^{28}Si (92.2%), ^{29}Si (4.7%), ^{30}Si (3.1%). Therefore, the Si_xH_z, Ge_xH_z and mixed $Si_xGe_yH_z$ clusters appear as groups of peaks in the mass spectra. At pyrolysis temperatures 1270 K and higher, peak groupings with m/e beginning at 98, 126, 154, and 170 were observed indicating the production of $SiGeH_z$, Si_2GeH_z, Si_3GeH_z, $SiGe_2H_z$, respectively (Figure 6.1). Peaks in the range m/e 238 to 258 were also observed corresponding to either $SiGe_3H_z$, Si_6GeH_z, or perhaps both. Possible Si_5GeH_z peaks in the range m/e 210 to 226 are obscured by the relatively large Ge_3H_z signal that appears in the same region of the spectra. Very small peaks in the m/e 196 to 208 region indicated some production of Si_2Ge_2 although, due to the low signal to noise ratio, they were not well resolved. A general increase in signal was observed in the m/e 390 region indicating the production of $SiGe_5H_z$ but, due to

decreasing resolution at higher mass ranges, individual peaks were not well resolved. Si_4GeH_z was not observed. In general, the mixed clusters with multiple Ge atoms were more abundant than those with multiple Si atoms. This is consistent with the more facile production of Ge_xH_z than Si_xH_z clusters.

The production of highly unsaturated silicon and germanium mixed clusters by gas phase pyrolysis exhibited clear temperature dependence as observed in our prior studies involving the production of pure silicon and pure germanium clusters.[24,25,34] At lower temperatures (~1100 K) mostly hydrogen rich clusters are produced. As the pyrolysis temperature was increased, greater proportions of highly unsaturated and bare clusters were observed. Theoretical isotopic abundances of bare (completely dehydrogenated) Si, Ge, and mixed Si and Ge clusters were modeled by fitting to a multinomial distribution using the natural Si and Ge isotopic abundances, and they are shown in the insets of Figures 6.2-6.4.

Small peaks at m/e 98,100,102, 104, 106, and 108 appeared at 1270 K pyrolysis temperature indicating the production of $SiGeH_z$ (Figure 6.2). At 1390 K, the m/e 106 and 108 peak disappeared while the others at lower mass grew slightly, indicating loss of hydrogen from the $SiGeH_z$ clusters. At higher temperatures m/e 98, 100, and 102 peaks grew while the m/e 104 peak decreased in size. The m/e 98, 100, and 102 peaks represent the most isotopically dominant SiGe clusters. At the higher temperatures (1650K and 1780K) the mass peak pattern is very similar to that of the modeled bare SiGe cluster (inset), indicating that the $SiGeH_z$ clusters produced are mostly bare clusters (z=0). Note

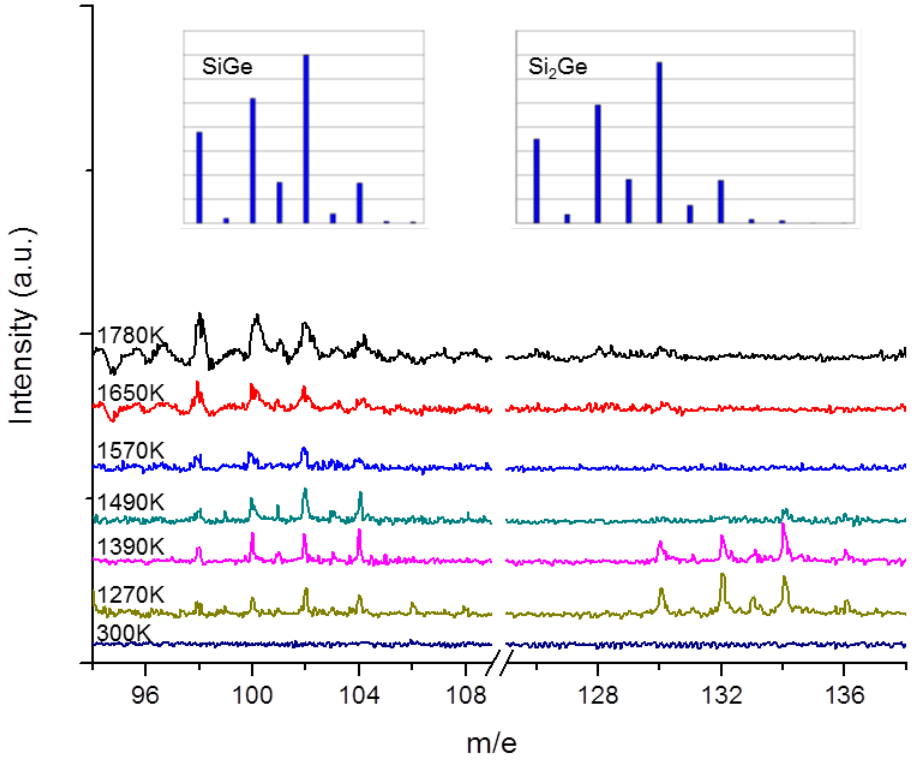

Figure 6.2 $SiGeH_z$ and Si_2GeH_z formation upon flash pyrolysis of silane and germane between 1270 K and 1780 K. Baselines of the mass spectra are offset for clarity. Inset: Modeled isotopic abundances of bare (completely dehydrogenated) $SiGeH_z$ and Si_2GeH_z clusters.

that at 1270K the mass peak pattern is consistent with SiGe and $SiGeH_2$ mixture, and evolution of the mass peaks at high temperature indicates loss of H_2 instead of H.

Similar results were observed for Si_2GeH_z (Figure 6.2). Partially unsaturated silicon/germanium mixed clusters were observed at temperatures 1270 K and above. Further loss of hydrogen occurred at higher temperatures. At 1270 K, peaks were observed at m/e 130, 132, 133, and 134 representing Si_2GeH_z. As the bare Si_2Ge clusters are primarily mass 126, 128, and 130 amu, the mass profile of the peaks at 1270 K very closely follows the natural isotopic abundances for bare Si_2Ge with the mass of each peak increased by 4. Therefore, the Si_2GeH_z clusters produced at 1270 K contained some hydrogen, primarily with $z = 4$. At 1390 K, the peaks at m/e 130, 132, 133, and 134 began to decrease in size. These peaks began to fall into the baseline at higher temperatures as less saturated clusters were produced resulting in smaller peaks at each individual mass. At 1780 K, very small peaks appeared at m/e 126, 128, and 130 indicating the production of bare Si_2Ge clusters.

Partially unsaturated Si_3GeH_z clusters were also observed at 1270 K (Figure 6.3). Again, the profile of the peaks indicates a predominance of clusters containing 4 hydrogen atoms. Peaks at m/e 158, 160, 162, and 164 became smaller at 1390 K and smaller still at 1490 K. At 1570 K, peaks at 158, 160, and 162 began to grow and a small peak at 156 appeared. At 1650 K, a peak at m/e 154 appeared representing the lowest mass Si_3Ge bare cluster, $^{28}Si_3{}^{70}Ge$. Peaks at m/e 156, 158, and 160 continued to grow. At 1790 K, the peaks at m/e 154, 156, 158, 160 continued to grow while the m/e 162 peak remained approximately the same size. This produced a profile nearly identical to the

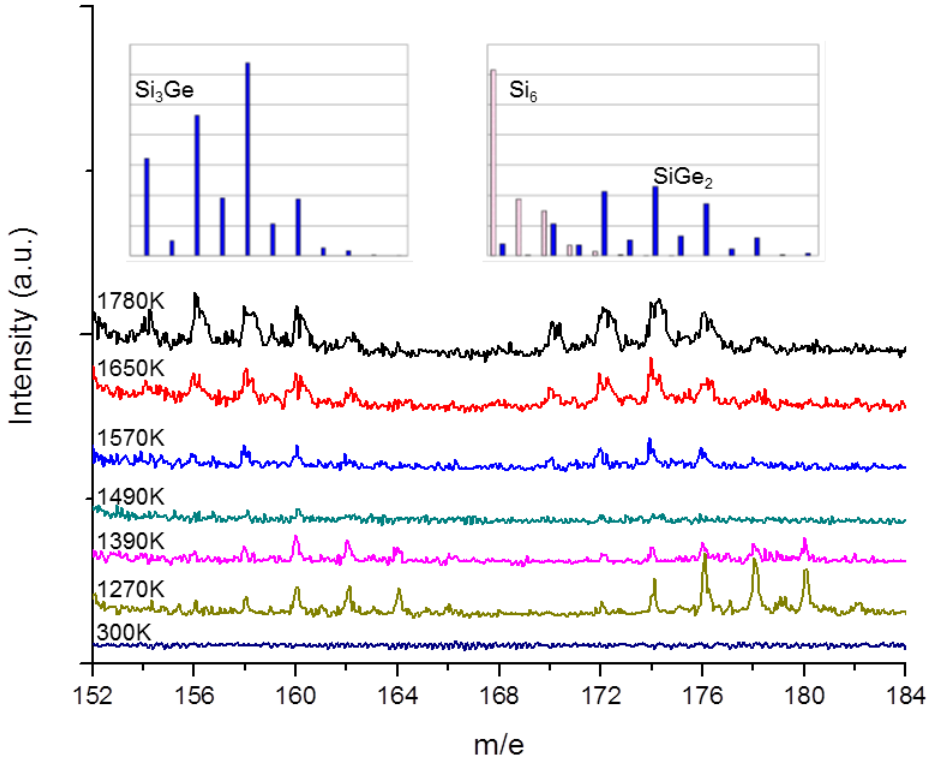

Figure 6.3 Si_3GeH_z and $SiGe_2H_z$ formation upon flash pyrolysis of silane and germane between 1270 K and 1780 K. Baselines of the mass spectra are offset for clarity. Inset: Modeled isotopic abundances of bare (completely dehydrogenated) Si_3GeH_z and $SiGe_2H_z$ clusters.

modeled Si_3Ge cluster indicating an increase in the production of bare Si_3Ge clusters. The development of the mass peak profiles as pyrolysis temperatures were increased indicates that the preferred is for loss of H_2 from Si_3GeH_z rather than loss of H. This mechanism is consistent with the fact that H_2 loss is the lower energy channel.

Production of $SiGe_2H_z$ and subsequent dehydrogenation (Figure 6.3) proceeded in a way that was completely analogous to that of Si_3GeH_z. At 1270 K, peaks at m/e 172, 174, 176, 178, and 180 were observed with peak intensities indicating predominance of Si_3GeH_z (z=4) clusters. These peaks decreased in intensity at moderate temperatures 1390 K and 1490 K. At 1570 K, a peak at m/e 170 appeared and peaks at m/e 172, 174, 176, and 178 increased in intensity again. At 1790 K, m/e 170, 172, 174, 176, and 178 all became more prominent and a m/e 168 peak appeared, and the resulting mass peak profile was nearly identical to that of the modeled $SiGe_2$ cluster. It is worth noting that there is significant overlap in the masses of Si_6 and $SiGe_2$ clusters. By isotopic modeling, Si_6 exists with masses including 168, 169, 170, and 171 amu in abundances 62%, 19%, 15%, and 3%, respectively. However, despite the 19% theoretical abundance of mass 169 Si_6, a peak at m/e 169 was not observed. Therefore, the contribution of Si_6 to the peaks in this mass region was probably negligible.

At temperatures 1570 K and above, peaks were observed at m/e 238, 240, 242, 244, 245, 246, 247, 248, 249, and 250. Because $SiGe_3H_z$ and Si_6GeH_z both would be expected to show peaks in the region m/e 238 to 256, these peaks cannot be unambiguously identified. However the peak intensity profile follows the calculated theoretical mass profile of $SiGe_3$ quite closely (Figure 6.4). The highest intensity peak on

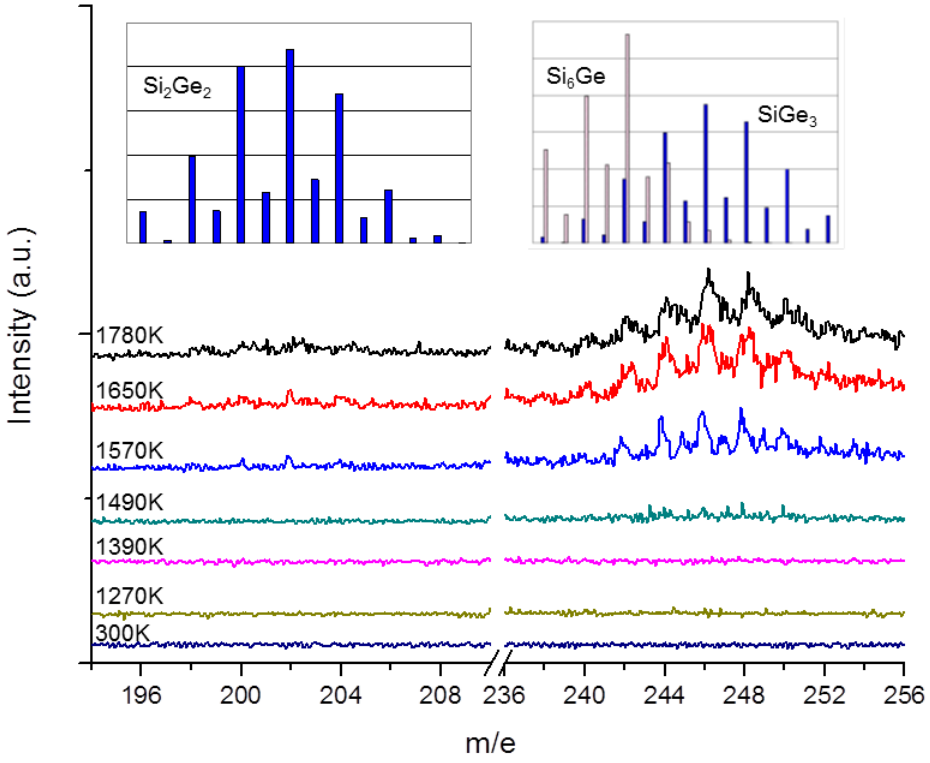

Figure 6.4 $Si_2Ge_2H_z$ and $SiGe_3H_z$ formation upon flash pyrolysis of silane and germane between 1270 K and 1780 K. Baselines of the mass spectra are offset for clarity. Inset: Modeled isotopic abundances of bare (completely dehydrogenated) $Si_2Ge_2H_z$ and $SiGe_3H_z$ clusters.

the mass spectra was at m/e 246 corresponding to the most prevalent $SiGe_3$ mass. The most common Si_6Ge masses are 238, 240, and 242 amu but the m/e 238, 240, and 242 peaks were relatively small in the spectra. Therefore, the peaks in the m/e 238 to 250 can be assumed to indicate primarily $SiGe_3H_z$ production. Similarly, $SiGe_5$ peaks were observed in the m/e = 210 to 226 range at higher pyrolysis temperatures ($\geq$ 1570 K). However, individual peaks were not well resolved.

Composition of the $Si_xGe_yH_z$ clusters and their hydrogen content can be evaluated by comparing the relative experimental peak intensities to the relative theoretical intensities of Si_xGe_y clusters based on isotopic abundances. This can be done quantitatively by fitting peaks in the mass spectra to Gaussian peaks to determine the experimental intensities. Peaks that are known to correspond to bare clusters are used to determine the theoretical abundance of higher mass bare clusters in the series. The contributions of the bare clusters can then be subtracted to determine the relative area of the peaks that are due to hydrogenated clusters, particularly $Si_xGe_yH_1$. Performing this process iteratively will reveal the relative amounts of each $Si_xGe_yH_z$ for any $z>0$.[25] Unfortunately, because the peaks that we might use as reference bare cluster peaks for $SiGeH_z$, Si_2GeH_z, Si_3GeH_z, $SiGe_2H_z$ and $SiGe_3H_z$ were quite small, the peaks could not be fit with enough precision to provide very meaningful quantitative results.

A similar qualitative assessment can be made by performing two comparisons: (a) comparing the mass profile of peaks corresponding to a particular $Si_xGe_yH_z$ to the theoretical mass profile of the bare clusters, and (b) comparing the relative size of a peak that can be unambiguously ascribed to a bare cluster to other peaks in the series. For

Si_3GeH_z, and $SiGe_2H_z$, $SiGe_3H_z$ the m/e 154, 168, and 238 peaks, respectively, represent known bare clusters. All of these peaks grew significantly at higher temperatures indicating an increased proportion of bare clusters. In addition, at the higher temperatures, the mass profile for the peaks corresponding to each cluster were in fairly good agreement with the theoretical mass profile, although the width of the some peaks complicated this comparison. Peaks beginning at m/e 98 corresponding to $SiGeH_z$ do not appear to follow the theoretical mass peak distribution. However, the lower mass peaks 98,100, and 102 were most prominent in both the model and the spectra indicating extensive dehydrogenation at 1650 K and above. No definitive conclusions can be made about the Si_2GeH_z clusters because the mass peaks were not very well resolved at the higher temperatures, but, again, the lowest mass peaks dominated which suggests that mostly bare clusters were produced at high temperatures.

Formation of polysilanes by the pyrolysis of silane are widely believed to occur by the insertion of silylene into silanes as shown below:[34,38,39]

$$SiH_2 + SiH_4 \leftrightarrow Si_2H_6$$

$$SiH_2 + Si_nH_{2(n+1)} \leftrightarrow Si_{n+1}H_{2(n+2)}$$

Subsequent dehydrogenation, particularly at higher pyrolysis temperatures, results in the formation of bare silicon clusters. Germanium clusters are believed to form by an analogous mechanism.[25,40] Mixed silicon and germanium clusters are likely formed by the same insertion mechanism as evidenced by the appearance of primarily hydrogenated $SiGeH_z$, Si_2GeH_z, Si_3GeH_z, and $SiGe_2H_z$ clusters at pyrolysis temperatures of approximately 1200 K-1500 K, and increasingly larger amounts of bare clusters at higher

temperatures. Also, $Si_xGe_yH_z$ clusters produced in this study at relatively low pyrolysis temperatures almost exclusively contain even numbers of hydrogen atoms (z = 2 or 4) thus providing further evidence for the insertion and sequential H_2 loss mechanism.

Condensation of bare clusters is also believed to contribute to cluster formation particularly for larger clusters Si_n (n>4) in silane pyrolysis.[24] Condensation of smaller clusters may also be important in the formation of silicon germanium mixed clusters. Hydrogenated $SiGe_3H_z$ and $SiGe_5H_z$ clusters are not observed at lower pyrolysis temperatures, and $SiGe_3$ and $SiGe_5$ clusters do not seem to be created from the dehydrogenation of $SiGe_3H_z$ and $SiGe_5H_z$ clusters, therefore condensation of smaller bare clusters may contribute significantly to their formation. In addition, the growth of the $SiGe_5H_z$ peak at higher pyrolysis temperatures is accompanied by a decrease in the Ge_5H_z peak intensity. This observation might imply the combination of Ge_5 with Si in the production of $SiGe_5$.

6.4 Conclusion

Direct observation of highly unsaturated Si/Ge mixed clusters $SiGeH_z$, Si_2GeH_z, Si_3GeH_z, $SiGe_2H_z$, $SiGe_3H_z$ and $SiGe_5H_z$ from the pyrolysis of a 1:1 silane:germane mixture is reported. Flash pyrolysis coupled with VUV-TOFMS is used to isolate and observe hydrogenated $Si_xGe_yH_z$ reactive intermediates and their subsequent dehydrogenation to form bare Si_xGe_y clusters. Si/Ge mixed clusters likely form by the insertion of silylene SiH_2 and germylene GeH_2 into silane, germane, polysilanes, and

polygermanes. Si_xGe_y mixed clusters, particularly those in which $x+y>4$, may also form by the combination of smaller clusters.

References

(1) E. Kasper, *Journal of Crystal Growth* **1995**, 150, 921.

(2) B.S. Meyerson, *Proceedings of the IEEE* **1992**, 80, 1592.

(3) K. Ismail, S. Rishton, J.O. Chu, K. Chan, B.S. Meyerson, *IEEE Electron Device Letters* **1993**, 14, 348.

(4) D.K. Nayak, K. Goto, A. Yutani, J. Murota, Y. Shiraki, *IEEE Transactions on Electron Devices* **1996**, 43, 1709.

(5) S.K. Ray, R. Mahapatra, S. Maikap, *Journal of Materials Science-Materials in Electronics* **2006**, 17, 689.

(6) L. Colace, G. Masini, G. Assanto, *IEEE Journal of Quantum Electronics* **1999**, 35, 1843.

(7) M. Takabatake, J. Ohwada, Y.A. Ono, K. Ono, A. Mimura, N. Konishi, *IEEE Transactions on Electron Devices* **1991**, 38, 1303.

(8) L.P. Chen, T.C. Chou, W.C. Tsai, G.W. Huang, H.C. Tseng, H.C. Lin, C.Y. Chang, *Japanese Journal of Applied Physics Part 2-Letters* **1995**, 34, 869.

(9) C. Li, S. John, E. Quinones, S. Banerjee, *Journal of Vacuum Science & Technology A-Vacuum Surfaces and Films* **1996**, 14, 170.

(10) M. Cao, A. Wang, K.C. Saraswat, *Journal of the Electrochemical Society* **1995** 142, 1566.

(11) J.W. Kim, M.K. Ryu, K.B. Kim, S.J. Kim, *Journal of the Electrochemical Society* **1996**, 143, 363.

(12) T.J. King, K.C. Saraswat, *Journal of the Electrochemical Society* **1994**, 141, 2235.

(13) R. Schutz, J. Murota, T. Maeda, R. Kircher, K. Yokoo, S. Ono, *Applied Physics Letters* **1992**, 61, 2674.

(14) J.M. Hartmann, V. Loup, G. Rolland, M.N. Semeria, *Journal of Vacuum Science & Technology* B **2003**, 21, 2524.

(15) T.I. Kamins, D.J. Meyer, *Applied Physics Letters* **1991**, 59, 178.

(16) H. Kuhne, T. Morgenstern, A. Fischer, G. Kissinger, D. Kruger, *Crystal Research and Technology* **1994**, 29, 199.

(17) P. Campbell, D.G. Walmsley, R.L.F. Chong, D. Gay, H.S. Gamble, D.W. McNeill, *Applied Physics A-Materials Science & Processing* **1998**, 66, S1067.

(18) P. Warren, I. Sagnes, D. Dutartre, P.A. Badoz, J.M. Berroir, Y. Guldner, J.P. Vieren, M. Voos, *Microelectronic Engineering* **1994**, 25, 171.

(19) M.W. Stoker, T. Merchant, A. Morton, J. Hildreth, *Microelectronic Engineering* **2003**, 69, 633.

(20) X.L. Yang, M. Tao, *Journal of the Electrochemical Society* **2007**, 154, H53.

(21) I.M.R. Lee, C.G. Takoudis, *Journal of the Electrochemical Society* **1996**, 143, 1719.

(22) P.M. Garone, J.C. Sturm, P.V. Schwartz, S.A. Schwarz, B.J. Wilkens, *Applied Physics Letters* **1990**, 56, 1275.

(23) J. Olivares, J. Sangrador, A. Rodriguez, T. Rodriguez, *Journal De Physique IV* **1999**, 9, 321.

(24) S.D. Chambreau, L.M. Wang, J.S. Zhang, *Journal of Physical Chemistry* A **2002**, 106, 5081.

(25) S.D. Chambreau, J.S. Zhang, *Chemical Physics Letters* **2002**, 351, 171.

(26) P.L. Timms, C.S. Phillips, C.C. Simpson, *Journal of the Chemical Society* **1964**, 1467.

(27) K.M. Mackay, S.T. Hosfield, S.R. Stobart, Journal of the C*hemical Society A - Inorganic Physical Theoretical* **1969**, 2937.

(28) R. Viswanathan, R.W. Schmude, K.A. Gingerich, *Journal of Chemical Thermodynamics* **1995**, 27, 763.

(29) A.N. Andriotis, M. Menon, G.E. Froudakis, *Journal of Cluster Science* **1999**, 10, 549.

(30) S.D. Li, Z.G. Zhao, X.F. Zhao, H.S. Wu, Z.H. Jin, *Physical Review B* **2001**, 64,

(31) L.R. Marim, L.T. Ueno, F.B.C. Machado, A. Dal Pino, Jr., *Phys. Status Solidi B* **2007**, 244, 3601.

(32) D. Bing, Q.C. Nguyen, X.-f. Fan, J.-L. Kuo, *The Journal of Physical Chemistry A* **2008**, 112, 2235.

(33) S.D. Chambreau, J.S. Zhang, J.C. Traeger, T.H. Morton, *International Journal of Mass* Spectrometry **2000**, 199, 17.

(34) S.D. Chambreau, J.S. Zhang, *Chemical Physics Letters* **2001**, 343, 482.

(35) D.W. Kohn, H. Clauberg, P. Chen, *Review of Scientific Instruments* **1992**, 63, 4003.

(36) D.M. Lubman, R.M. Jordan, *Review of Scientific Instruments* **1985**, 56, 373.

(37) C.G. Newman, J. Dzarnoski, M.A. Ring, H.E. Oneal, *International Journal of Chemical Kinetics* **1980**, 12, 661.

(38) A.A. Onischuk, V.P. Strunin, M.A. Ushakova, V.N. Panfilov, *International Journal of Chemical Kinetics* **1998**, 30, 99.

(39) M.A. Ring, H.E. Oneal, *Journal of Physical Chemistry* **1992**, 96, 10848.

(40) H. Kawasaki, J. Kida, K. Sakamoto, T. Fukuzawa, M. Shiratani, Y. Watanabe, *Japanese Journal of Applied Physics Part 2-Letters* **1998**, 37, L475.

CHAPTER 7

Pyrolysis of Tetramethylsilane and Tetramethylgermane

7.1 Introduction

SiC is an interesting material due to its wide band gap which allows for high temperature, high frequency, and high power microelectronic applications. In addition SiC has a variety of attractive physical properties including high mechanical strength, wear resistance, and thermal stability. SiC thin films are generally produced via the chemical vapor deposition (CVD) of SiH_4 and C_3H_8 precursors on Si substrate at temperatures above 1300^0C. However, this method has proven problematic due to the large difference in lattice constants and thermal expansion coefficients between Si and SiC.[1] Organosilanes such as tetramethylsilane (TMS) already contain a Si-C bond and generally decompose at relatively low temperatures, thus making them promising alternatives to the SiH_4/C_3H_8 mixture. Indeed, precursors such as TMS have been successfully used to grow high quality SiC films by a variety of CVD techniques including plasma enhanced CVD, low pressure CVD, hot-wire catalytic CVD, and others,[2–11] but further study is required in order to better control the SiC thin film properties.

The germanium analog of TMS, tetramethylgermane (TMG) also has found use in CVD processes particularly for deposition of GeC. Geranium carbide materials are not as well studied as silicon carbides but they are known to have several interesting properties

that warrant further study of the CVD processes of GeC. These include tunable refractive index by varying germanium/carbon ratios, and band gap tunability which may prove useful in photovoltaic applications.

Although the mechanism of SiC deposition from TMS pyrolysis is not yet well understood, the gas phase pyrolysis of TMS has been previously studied using static cell[12], flow cell[13], and "wall-less reactor"[14] techniques. These studies suggest that TMS pyrolysis proceeds by first order reaction kinetics in which the initial cleavage of one Si-C bond is the rate determining step. Successive losses of the remaining methyl groups were then proposed to occur in succession.[13,14]

$$Si(CH_3)_4 \rightarrow {}^{\bullet}Si(CH_3)_3 + {}^{\bullet}CH_3$$

$${}^{\bullet}Si(CH_3)_3 \rightarrow {:}Si(CH_3)_2 + {}^{\bullet}CH_3$$

$${:}Si(CH_3)_2 \rightarrow {}^{\bullet}SiCH_3 + {}^{\bullet}CH_3$$

$${}^{\bullet}SiCH_3 \rightarrow Si + {}^{\bullet}CH_3$$

Kim et. al. more recently suggested that the loss of the second methyl was in fact the rate limiting step in TMS pyrolysis.[1] Recent hot filament dissociation vacuum-ultraviolet time-of-flight mass spectrometry (VUV-TOFMS) experiments measured methyl as the primary product of catalytic TMS dissociation on heated tungsten wire.[15] Hydrogen abstraction by methyl and its pyrolysis complement from the parent may also be an important pathway.[16]

$$Si(CH_3)_4 + {}^{\bullet}CH_3 \rightarrow {}^{\bullet}Si(CH_3)_3CH_2 + CH_4$$

$$^{\bullet}Si(CH_3)_3 + {}^{\bullet}CH_3 \rightarrow Si(CH_3)_2CH_2 + CH_4$$

Only two known studies of TMG pyrolysis exist. In the previously referenced "wall-less reactor" study,[14] the mechanism of TMG pyrolysis was stated to be the same as that for TMS shown above. Smith and Patrick studied the TMG pyrolysis in 1983 using the Knudsen cell very low pressure pyrolysis (VLPP) technique and determined a Ge-C bond energy of 83 kcal mol^{-1} but did not propose a mechanism for the TMG pyrolysis.[17]

In this study, the flash pyrolysis VUV-PI-TOFMS technique is used to study TMS and TMG thermal decomposition processes relevant to SiC and GeC CVD. Prior mechanistic studies of SiC CVD precursors were complicated by the recombination of reactive intermediates prior to detection and fragmentation of pyrolysis products due to electron impact (EI) and multi-photon ionization (MPI). In this work, TMS and TMG are pyrolyzed on a short 20-100 μs time scale minimizing secondary reactions and recombination of the pyrolysis products. A 10.45 eV "soft" photoionization light source is used to ionize pyrolysis products for detection by time-of-flight mass spectrometry thereby minimizing photofragmentation. This technique allows the direct observation of initial thermal decomposition products and reactive intermediates providing greater insight into the gas-phase processes involved in CVD.

7.2 Experimental

The TMS pyrolysis experiments were conducted on a home-built vacuum ultraviolet (VUV) photoionization time-of-flight mass spectrometer (TOFMS) apparatus

that has been previously described.[18,19] TMS (99.9%) and TMG (99%) were obtained from Sigma-Aldrich and used without further purification. Samples were diluted to approximately 1% concentration in He carrier gas by passing He through liquid TMS or TMG contained in glass bubblers immersed in cold temperature baths. A -41 ^{0}C acetonitrile/ dry ice bath was used for TMS. TMG was held at -10 ^{0}C using a saturated NaCl solution with ice.

7.3 Results

(a) Tetramethylsilane Pyrolysis

Pyrolysis of TMS was observed at temperatures of 660 K, 910 K, 1060 K, 1200 K, 1300 K, 1390 K, 1470 K, and 1540K. Pyrolysis mass spectra are shown in Figures 7.1, 7.3, and 7.4. The major products of TMS pyrolysis up to 1470 K are shown in Figure 7.1 along with a room temperature mass spectrum. At room temperature, peaks are observed at m/e = 88 and m/e = 73 which correspond to the parent TMS peak and the $(CH_3)_3Si^+$ trimethylsilyl cation, respectively. The trimethylsilyl fragment predominates in the room temperature spectrum appearing in a 3.8:1 ratio relative to the parent peak. This is expected due to the relative instability of the TMS cation. The appearance energy of $(CH_3)_3Si^+$ is 10.2eV.[20] Thus, the 10.45 eV ionization source is sufficiently energetic to photoionize and fragment a significant fraction of the TMS molecules. Silicon isotope peaks of TMS and $(CH_3)_3Si^+$ due to ^{29}Si, ^{30}Si are also observed at m/e = 89, 90 and m/e = 74, 75, respectively. The relative abundances of ^{28}Si, ^{29}Si, and ^{30}Si are 0.9223, 0.0467, and 0.031, respectively. The pyrolysis temperature was increased incrementally to 660 K,

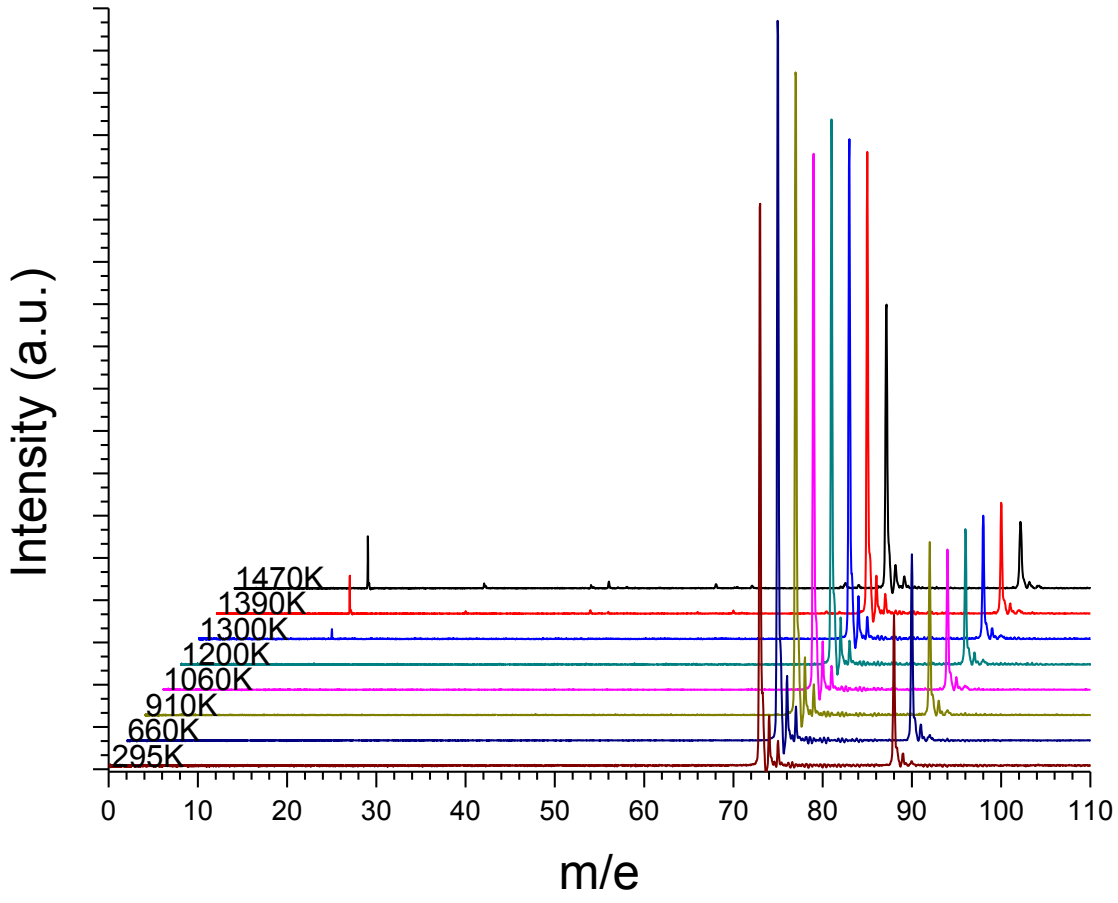

Figure 7.1 Stack plot of mass spectra for pyrolysis of $Si(CH_3)_4$ (~1%) in He at room temperature and pyrolysis temperatures 660K to 1470 K. Mass spectra are offset for clarity.

910 K, and 1060 K. However, no thermal decomposition was observed at these temperatures.

At pyrolysis temperature 1200 K a peak begins to appear at m/e = 15 indicating the production of methyl radicals. The production of $(CH_3)_3Si^{\bullet}$ results in a simultaneous

decrease in intensity of the m/e = 88 parent peak and increase in the intensity of the m/e = 73 peak although the contribution of $(CH_3)_3Si^{\bullet}$ to the m/e = 73 peak is somewhat obscured by the presence of the large photoionization fragment peak at the same mass. Methyl production is accompanied by a drop in the intensity of the TMS peak relative to the intensity of the $(CH_3)_3Si^{+}$ fragment peak, or an increase of the intensity ratio of m/e 73 vs. m/e 88, as shown in Figure 7.2.

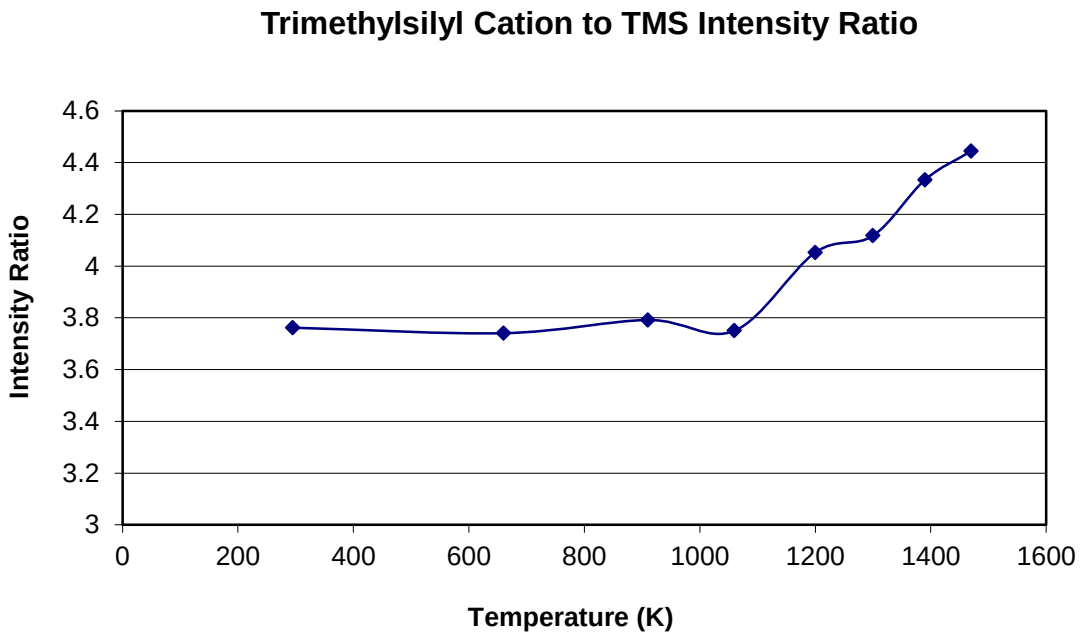

Figure 7.2 Ratio of the peak intensities of m/e 73 of $Si(CH_3)_3^{+\bullet}$ versus $Si(CH_3)_4$ parent peak showing the onset of thermal decomposition of TMS at approximately 1100 K.

These data indicate cleavage of the Si-C bond as the initial step of TMS thermal decomposition:

$$(CH_3)_4Si \rightarrow (CH_3)_3Si^{\bullet} + {}^{\bullet}CH_3 \qquad (7.1)$$

The intensity of the methyl peak continues to grow as the nozzle temperature is increased to 1300 K. The size of the TMS parent again declines relative to that of the $(CH_3)_3Si^+$ fragment indicating further methyl loss from the parent (Figure 7.2). A small peak at m/e 58 also appears indicating subsequent methyl loss from $(CH_3)_3Si^{\bullet}$ as seen in Figures 7.3 and 7.4.

$$(CH_3)_3Si^{\bullet} \rightarrow (CH_3)_2Si + {}^{\bullet}CH_3 \qquad (7.2)$$

At 1390 K, increased amounts of methyl and $(CH_3)_2Si^{\bullet}$ are produced. In addition, loss of multiple hydrogen atoms from $(CH_3)_3Si^{\bullet}$ occurs as evidenced by the appearance of peaks at m/e 72, 70, and 68. Small peaks at m/e 54 and 56 appear to indicate H_2 elimination from $(CH_3)_2Si$. New peaks also appear at m/e 42 and 44 and a very small peak at m/e 43 which corresponds to $(CH_3)Si^{\bullet}$. The relatively small amount of $(CH_3)Si^{\bullet}$ observed serves to indicate that the further loss of methyl from $(CH_3)_2Si^{\bullet}$

$$(CH_3)_2Si \rightarrow (CH_3)Si + {}^{\bullet}CH_3 \qquad (7.3)$$

is far less prevalent in TMS decomposition than its previous analogs, reactions 7.1 and 7.2. Instead there appears to be elimination of methane from $(CH_3)_2Si$ after isomerization to produce $SiCH_2$, although loss of H atom from $(CH_3)Si^{\bullet}$ may also contribute.

$$(CH_3)_2Si \rightarrow SiCH_2 + CH_4 \qquad (7.4)$$

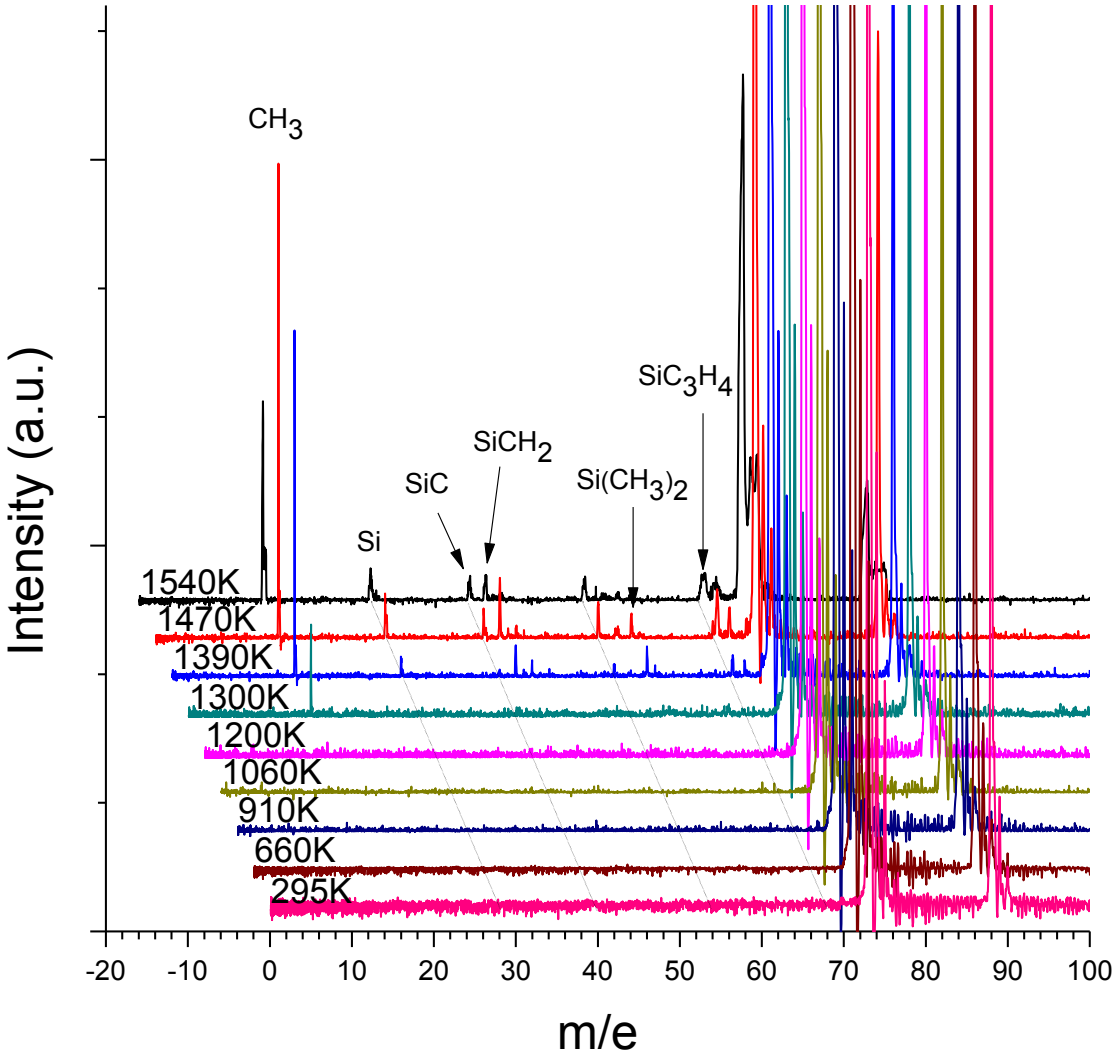

Figure 7.3 Stack plot of mass spectra for pyrolysis of $Si(CH_3)_4$ (~1%) in He at room temperature and pyrolysis temperatures 660K to 1540 K enlarged to more clearly show product peaks. Mass spectra are offset for clarity.

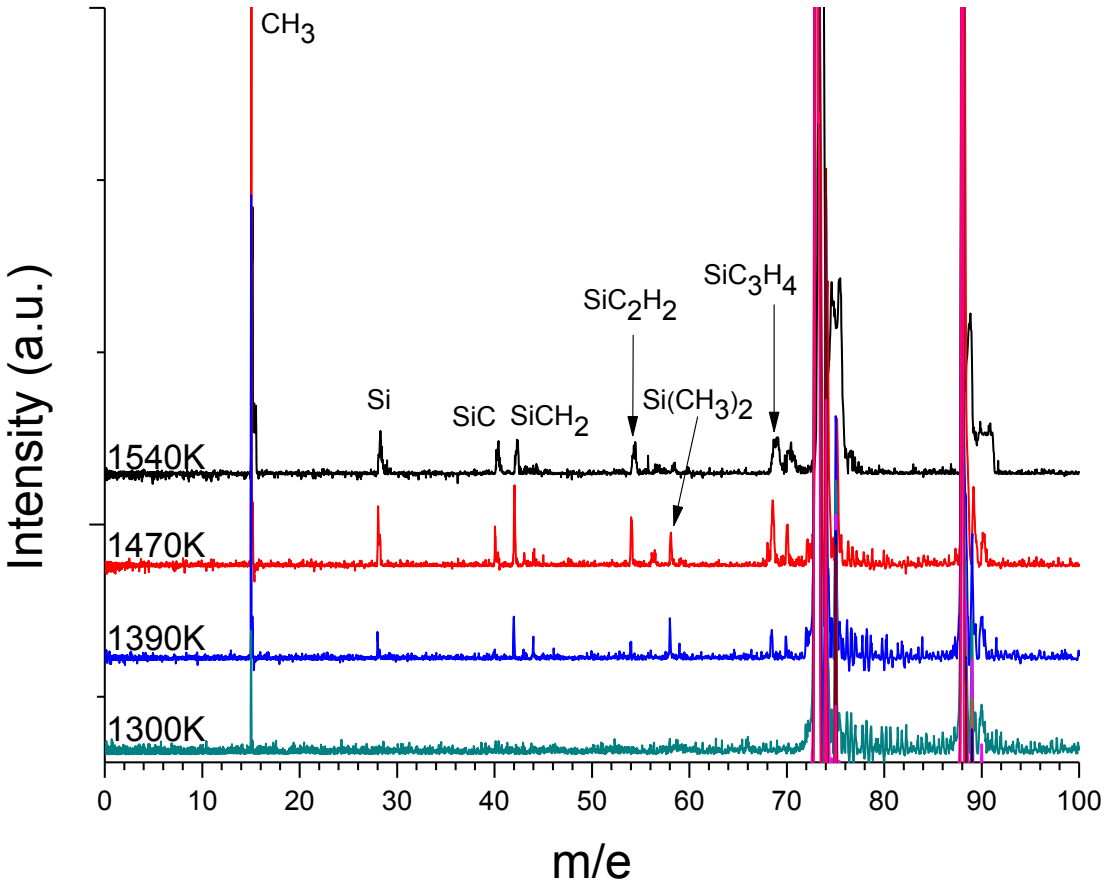

Figure 7.4 Stack plot of mass spectra for pyrolysis of $Si(CH_3)_4$ (~1%) in He at pyrolysis temperatures 1390 K, 1470 K, and 1540 K enlarged to show minor and secondary pyrolysis products.

A peak at m/e= 28 is also observed. This mass corresponds to that of a bare ^{28}Si atom and ethene, although ethene is not well ionized in this experiment due to its high IE.

At pyrolysis temperatures of 1470 K, significant loss of hydrogen from $(CH_3)_3Si^{\bullet}$, $(CH_3)_2Si$, and $SiCH_2$ is observed. The peaks m/e = 70, and 68 increase significantly in height indicating increased hydrogen loss from $(CH_3)_3Si^{\bullet}$. A drop in intensity of the m/e=58, $(CH_3)_2Si^{\bullet}$, is accompanied by an increase in m/e = 54 and 56 indicating that a significant fraction of $(CH_3)_2Si^{\bullet}$ radicals isomerize and undergo one and two sequential H_2 elimination reactions. Increased fraction of $SiCH_2$, m/e = 42, is also observed along with the appearance of a peak at m/e 40 due to SiC. Increased amounts of bare Si and/or ethene at m/e = 28 are also produced. The spectrum at pyrolysis temperature 1540 K appears similar to that at 1470 K. However, the peaks are less resolved and sensitivity is reduced.

Throughout all the temperatures, peaks are not observed in the range m/e = 83-87, indicating that the loss of hydrogen from the parent is a relatively insignificant dissociation channel. Also, no additional molecules larger than the parent were formed due to secondary reactions in the short time scale of our experiment.

(b) Tetramethylgermane Pyrolysis

Mass spectra for pyrolysis of $Ge(CH_3)_4$ (~1%) in He pyrolysis temperatures 930 K to 1570 K as well as at room temperature are shown in Figures 7.5 and 7.6. Photoionization fragmentation is more prevalent in the TMG pyrolysis mass spectra

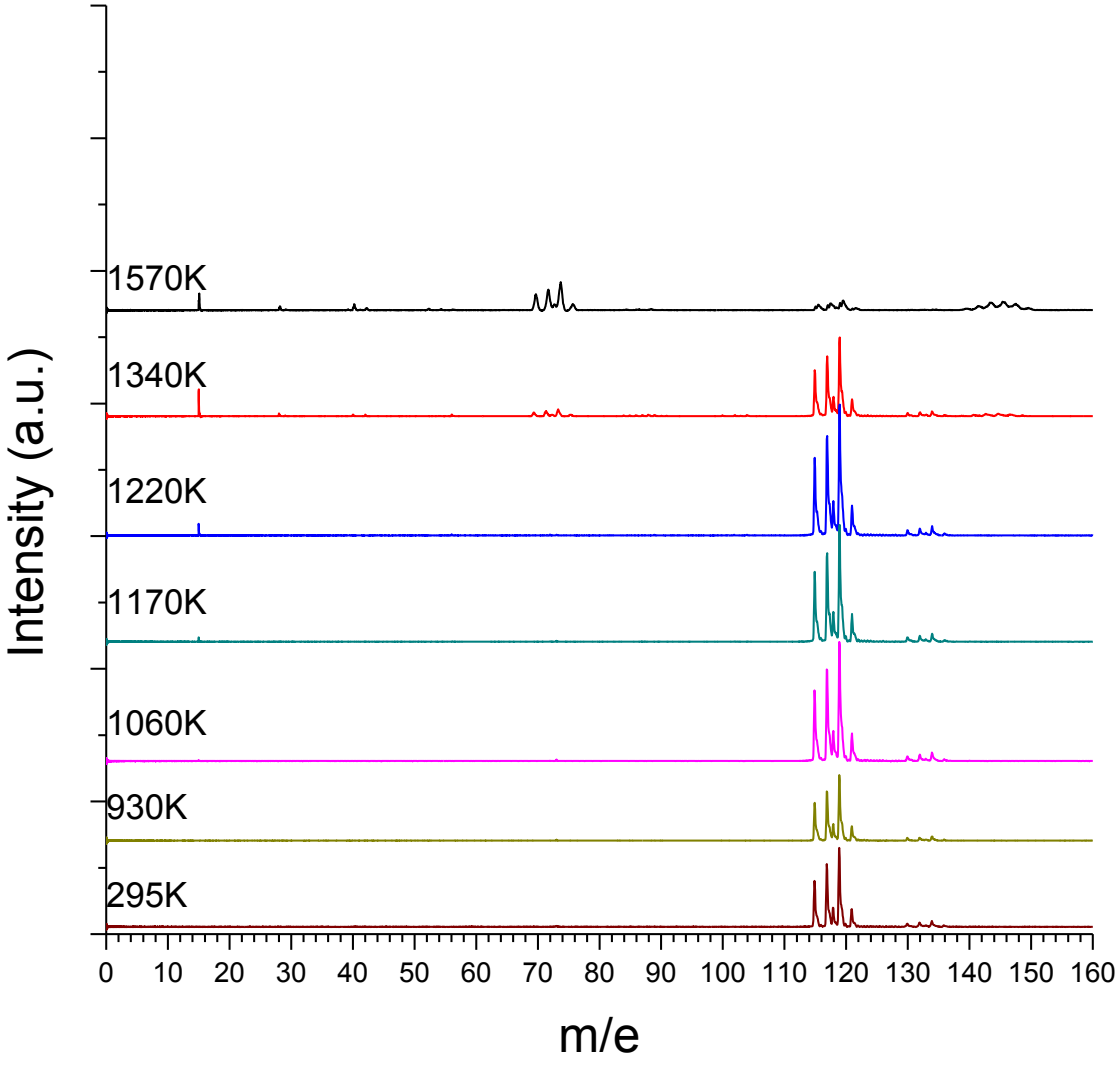

Figure 7.5 Stack plot of mass spectra for pyrolysis of $Ge(CH_3)_4$ (~1%) in He at room temperature and pyrolysis temperatures 930 K to 1570 K.

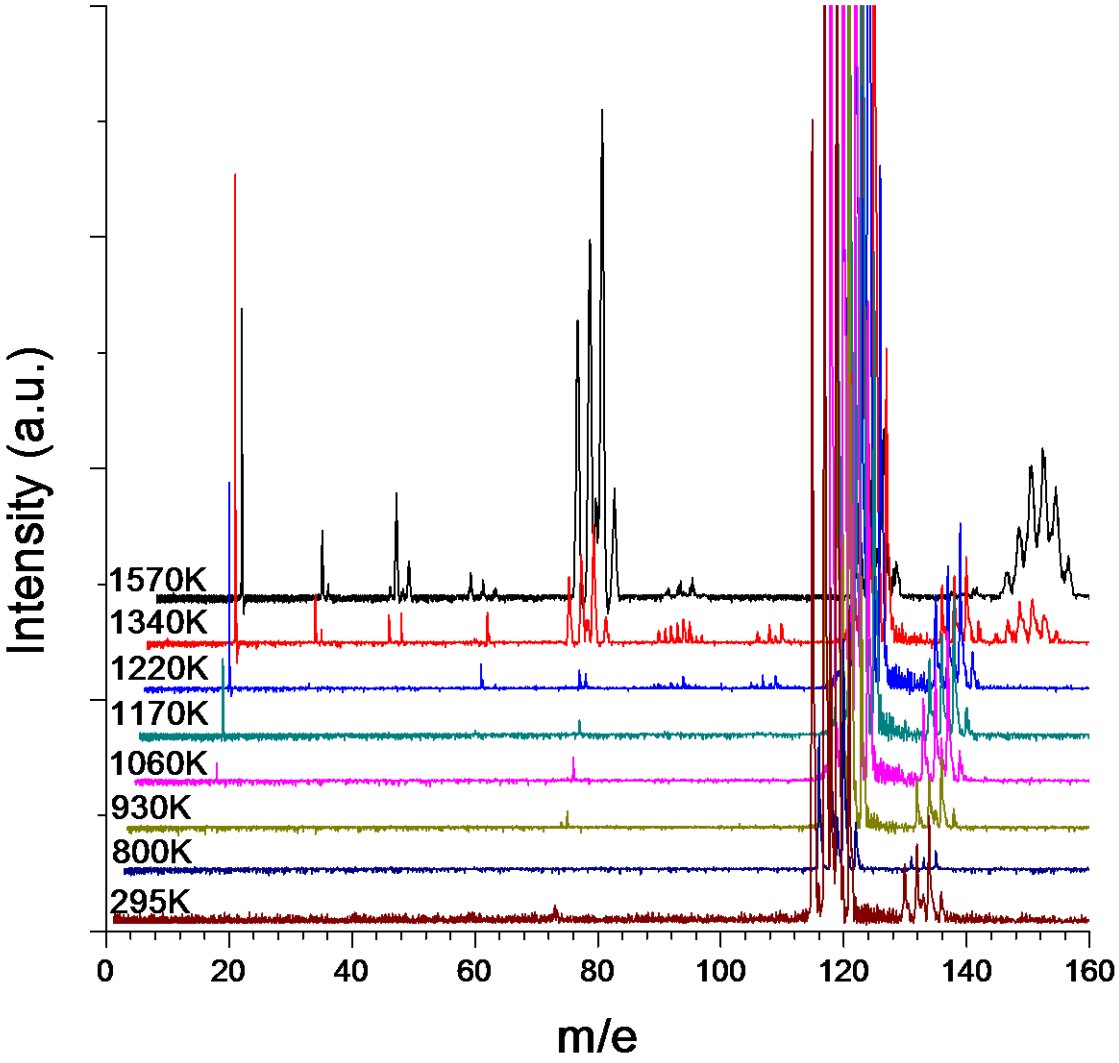

Figure 7.6 Stack plot of mass spectra for pyrolysis of $Ge(CH_3)_4$ (~1%) in He at room temperature and pyrolysis temperatures 800 K to 1570 K enlarged to more clearly show product peaks. Mass spectra are offset for clarity.

than in those for TMS due to the weaker Ge-C bond. For that reason, in Figure 7.5, the largest series of peaks in the room temperature spectrum is due to the photoionization fragment $Ge(CH_3)_3^{+\bullet}$. This species is indicated by the series of peaks at m/e 115,117, 118, 119, and 121 due to germanium isotopes ^{70}Ge, ^{72}Ge. ^{73}Ge, ^{74}Ge, and ^{76}Ge, with natural abundances 0.2123, 0.2766, 0.0733, 0.3594, 0.0744, respectively. A small series of peaks can also be seen at m/e 130, 132, 133, 134, and 136 due to the parent, TMG, but the intensity of the peaks indicates extensive photoionization fragmentation of TMG.

Viewing Figure 7.6, the onset of pyrolysis is observed at 1060 K where peaks appear at m/e 15 and m/e 74 corresponding to methyl radical and the most abundant Ge isotope, ^{74}Ge. As the pyrolysis temperature is raised to 1170 K, the m/e 15, methyl peak continues to grow indicating further thermal decomposition of TMG with the loss of methyl radicals.

At 1220 K increased methyl production continues as the m/e 15 peak increases in intensity by a factor of 3. New pyrolysis products are also observed. Figure 7.7 shows an expanded view of pyrolysis products at the pyrolysis temperatures above 1220 K. Small peaks appear at m/e 100, 102, 103 and 104 with the familiar Ge isotope profile indicating secondary loss of methyl from $Ge(CH_3)_3^{\bullet}$ to form $Ge(CH_3)_2$. A small peak at m/e 89 corresponds to $^{74}GeCH_3$ indicating continued Ge-C bond homolysis. Peaks at m/e 72 and 73 appear due to Ge atom. There is a minor product at 1220 K at m/e 56, which is likely C_4H_8 produced from secondary reactions of methyl radicals.

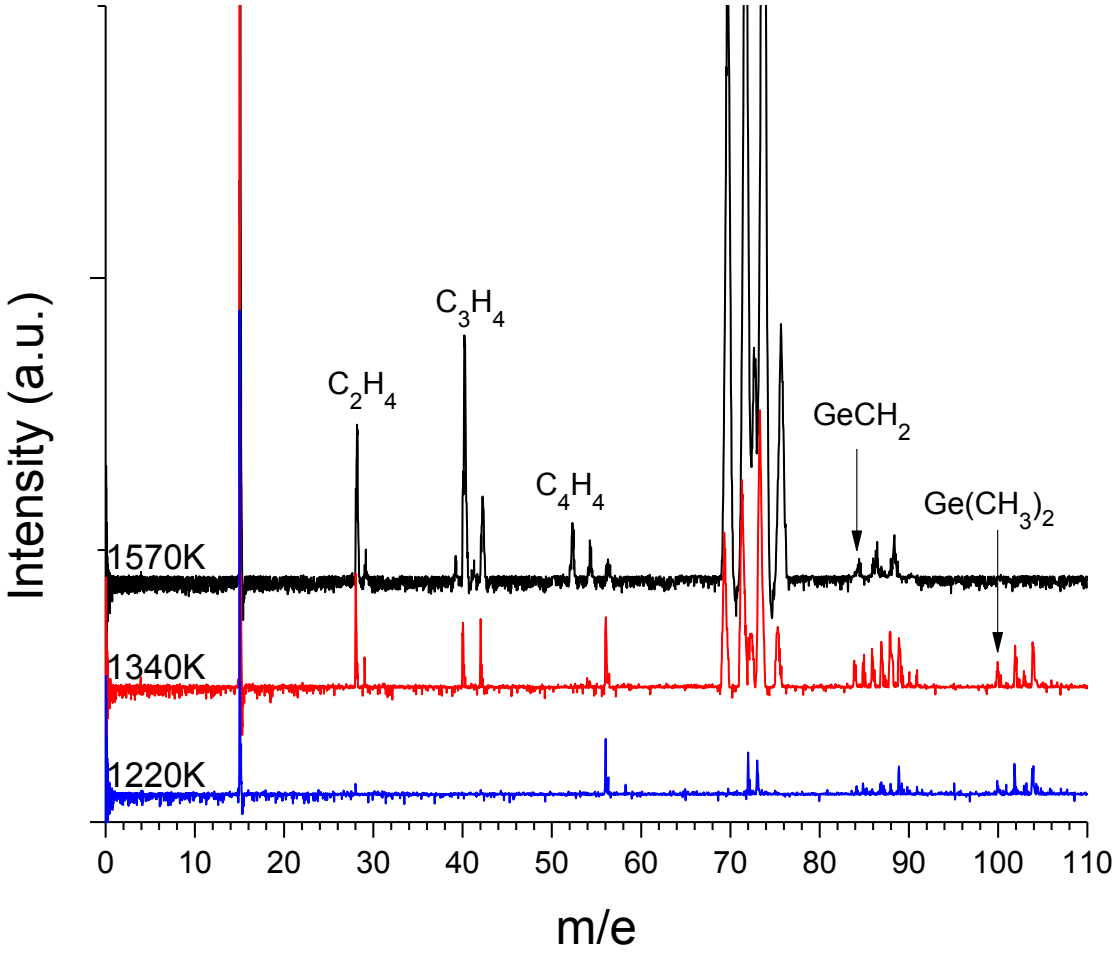

Figure 7.7 Stack plot of mass spectra for pyrolysis of $Ge(CH_3)_4$ (~1%) in He at pyrolysis temperatures 1220 K, 1340 K, and 1570 K enlarged to more clearly show product peaks.

When the pyrolysis temperature is raised to 1340 K, m/e 15 grows significantly indicating further methyl loss from TMG and its fragments. Peaks at m/e 100, 102, 103, and 104 double in size relative to those at 1220 K as a result of further secondary loss of methyl from $^{\bullet}Ge(CH_3)_3$. A series of peaks is observed in the region m/e 84 to 91. The m/e 84 peak is due to $^{70}GeCH_2$. ^{71}Ge does not occur naturally so m/e 85 exclusively represents $^{71}GeCH_3$. The fraction of $GeCH_3$ relative to $GeCH_2$ can be judged by the ratio of these peak intensities which is approximately 6 to 5. The rest of the series m/e 86 to 91 is due to a mixture of $GeCH_2$ and $GeCH_3$ exhibiting the loss of H atom from $GeCH_3$ to form $GeCH_2$. The m/e 56 peak increases in intensity by about 20% indicating increased C_4H_8 production. C_3H_6 and C_3H_4 are also observed as peaks at m/e 40 and 42. A peak at m/e 28 appears due to ethene with m/e 29, $^{\bullet}C_2H_5$ also observed. Significant formation of Ge atoms begins as demonstrated by the peaks at m/e 70, 72, 73, 74, and 75 in Figure 7.6 bearing the Ge isotope mass profile. A mass of unresolved peaks in the m/e 140 to 148 region also appears indicating condensation of Ge atoms to form Ge_2.

At 1540 K, the m/e 15 peak decreases in intensity by about 50% indicating the consumption of methyl radicals in secondary reactions. Aforementioned peaks at m/e 28 40, and 42 also grow significantly as the products C_2H_4 and C_3H_4 are the likely products of the methyl secondary reactions. The C_4H_8 peak at m/e 56 drops sharply in intensity from 1340 K to 1570 K due to H_2 elimination to form C_4H_6 and C_4H_4 as indicated by the appearance of peaks at m/e 52 and m/e 54. Production of Ge and Ge_2 increases by about 5 times at 1570 K resulting in a sharp increase of intensity at peaks in the m/e 70 to 75 and m/e 140 to 148 mass regions. No peaks appear at m/e 100 through 104 indicating that

$Ge(CH_3)_2$ is completely depleted by methyl loss reactions at 1570 K, as is the $GeCH_3$ product of this reaction, as H atom loss results in the disappearance of peaks at m/e 85, 87, and 89.

7.4 Discussion

The observed TMS pyrolysis products and proposed decomposition pathways are summarized in Scheme 7.1. At temperatures of 1060 K and below, little significant TMS pyrolysis is observed. The significant increase of the m/e= 73 peak relative to the parent at 1200 K and the growth of the m/e = 58 peak at 1390 K, corresponding to $(CH_3)_3Si^{\bullet}$ and $(CH_3)_2Si^{\bullet}$ respectively, indicate the importance of the loss of a first and second methyl group from the parent as a reaction pathway in the early stages of TMS decomposition, as also indicated by methyl production giving rise to a significant m/e 15 peak. Loss of H atom from the parent was not observed, and this is expected due to the much larger C-H bond dissociation energy of 97 kcal mol^{-1} versus 79 kcal mol^{-1} for the Si-C bond.[21,22] It has been suggested that abstraction of H atom from TMS by methyl is a significant secondary process.[21,23] However, this was also not observed, probably due to the short <100 μs reaction time, thus minimizing secondary reactions.

Loss of 1, 3, and 5 H atoms from $^{\bullet}Si(CH_3)_3$, which has not been previously suggested in the literature, is observed to be competitive with the loss of a second methyl radical as evidenced by significant peaks at m/e 68 and 70 as well as a left hand shoulder to the m/e 73, $^{\bullet}Si(CH_3)_3$, peak which is likely a poorly resolved m/e 72 peak. These are likely due to loss of a single H atom from $Si(CH_3)_3$, followed by successive H_2

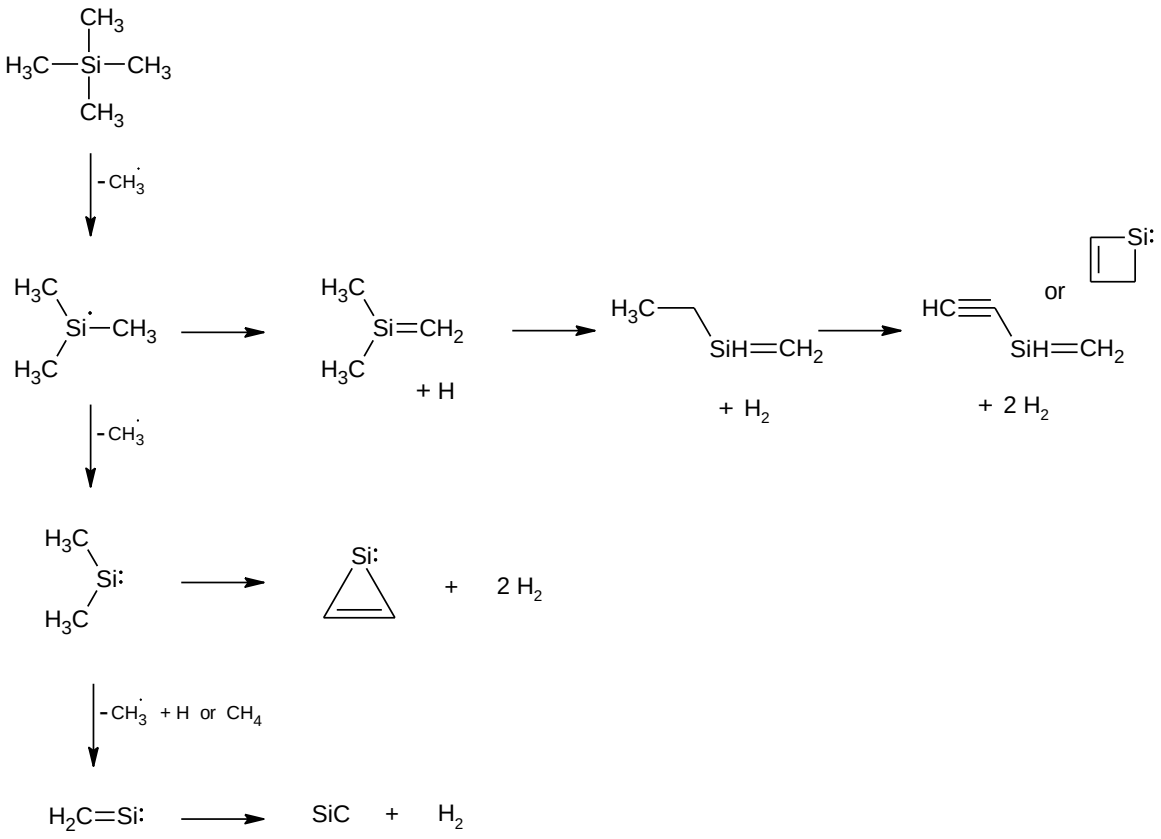

Scheme 7.1 Decomposition of TMS including example mechanism for H_2 elimination from $^{\bullet}Si(CH_3)_3$ via isomerization to a linear structure prior to H_2 elimination.

elimination reactions. However, the formation of these compounds would require isomerization of $^{\bullet}Si(CH_3)_3$. A mechanism via a linear structure is shown in Scheme 7.1 as an example and includes SiC_2H_4 which is also produced. Successive H_2 elimination from $Si(CH_3)_2$ is also observed producing SiC_2H_2. Ab initio calculations by Wu et al. have identified silacyclopropenylidene as the most stable SiC_2H_2 isomer suggesting that H_2 elimination likely occurs through a cyclic intermediate.[24]

The remainder of the decomposition chemistry is dominated by secondary reactions of methyl radical. These are more easily interpreted using the pyrolysis spectra of TMG for two reasons: (i) the weaker Ge-C bond is more easily cleaved leading to grater relative methyl production and thus higher rates of secondary reactions, and (ii) larger masses for product fragments that contain Ge, making Ge fragments less likely to have the same mass as small hydrocarbon products produced by methyl secondary reactions.

TMG pyrolysis proceeds in a manner similar to that of TMS pyrolysis with sequential loss of methyl radicals. However, due to the fact that the Ge-C bond is weaker than the Si-C bond, loss of a third methyl radical is observed in TMG pyrolysis while this does not occur to a significant extent under the same TMS pyrolysis conditions. Production of C_2H_4 dominated the secondary reactions with $^{\bullet}C_2H_5$ also appearing. Notably, m/e 29 due to $^{\bullet}C_2H_5$, and other significant hydrocarbon peaks such as m/e 56, C_4H_8, are not significant in TMS pyrolysis spectra. Thus, it can be concluded that secondary formation of hydrocarbon products is relatively low in TMS pyrolysis

conducted on the time scale of this experiment. C_2H_4 and larger unsaturated hydrocarbon products, such as C_3H_6, are likely due to recombination of radicals and rapid hydrogen elimination according to the now well established Rice-Herzfeld mechanism as indicated below.[25]

$$^{\bullet}CH_3 + {}^{\bullet}CH_3 \rightarrow C_2H_6$$

$$^{\bullet}CH_3 + C_2H_6 \rightarrow CH_4 + {}^{\bullet}C_2H_5$$

$$^{\bullet}CH_3 + {}^{\bullet}C_2H_5 \rightarrow C_3H_8 \rightarrow C_3H_6 + H_2$$

7.5 Conclusion

Pyrolysis of $Si(CH_3)_4$ (TMS) and $Ge(CH_3)_4$ (TMG) was performed. Direct and secondary pyrolysis products produced on the 20 to 100 μs time scale were directly observed. The primary thermal decomposition process for both TMS and TMG was cleavage of the Si-C and Ge-C bonds to form $^{\bullet}Si(CH_3)_3$ and $^{\bullet}Ge(CH_3)_3$, respectively. Secondary loss of a second methyl radical was also observed in both processes. A previously unobserved secondary decomposition process involving loss of H atom from $^{\bullet}Si(CH_3)_3$ followed by elimination of H_2 to form SiC_3H_8, SiC_3H_6, and SiC_3H_4, likely involving isomerization to a linear or cyclic arrangement, was also observed. Sequential loss of the third methyl with significant formation of Ge and Ge_2 was observed in the pyrolysis of TMG. Loss of a third methyl radical from TMS was not significant in the 20 to 100 μs time scale at the 910 K to 1540 K temperatures reached in this experiment. However Si and SiC where observed, perhaps due to elimination of methane from

$(CH_3)_2Si$. Secondary reactions of methyl to form unsaturated C_xH_y species, particularly in TMG decomposition, were also observed.

References

(1) Kim, K. C.; Nahm, K. S.; Hahn, Y. B.; Lee, Y. S.; Byun, H.-S. *Journal of Vacuum Science & Technology A: Vacuum, Surfaces, and Films* **2000**, *18*, 891.

(2) Thomas, L.; Maille, L.; Badie, J. M.; Ducarroir, M. *Surface Coatings Technology* **2001**, *142-144*, 314–320.

(3) Rynders, S. W.; Scheeline, A.; Bohrf, P. W. *Journal of Applied Physics* **1991**, *69*, 2951–2960.

(4) Seo, Y.; Nahm, K.; Suh, E. *Journal of Vacuum Science & Technology A: Vacuum, Surfaces, and Films* **1997**, *15*, 2226–2233.

(5) Fonseca, J. L. C.; Tasker, S.; Apperley, D. C.; Badyal, J. P. S. *Macromolecules* **1996**, *29*, 1705–1710.

(6) Herlin, N.; Lefebre, M.; Pealat, M.; Perrin, J. *Journal of Physical Chemistry* **1992**, *96*, 7063.

(7) Madigou, V.; Veintemillas, S.; Rodriguez-clemente, R.; Figueras, A.; Armas, B. *Journal of Crystal Growth* **1995**, *148*, 390–395.

(8) Veintemillasverdaguer, S.; Figueras, A.; Rodriguezclemente, R. *Journal of Crystal Growth* **1993**, *128*, 349–353.

(9) Lee, M.; Bent, S. F. *Journal of Vacuum Science & Technology A: Vacuum, Surfaces, and Films* **1998**, *16*, 1658–1663.

(10) Matsumura, H. *Applied Physics Letters* **1987**, *51*, 804.

(11) Mahan, A.; Carapella, J. *Journal of Applied Physics* **1991**, *69*, 6728–6730.

(12) Helm, D. F.; Mack, E. *Journal of the American Chemical Society* **1937**, *59*, 60–62.

(13) Clifford, R.; Gowenlock, B. *Journal of Organometallic Chemistry* **1972**, *34*, 53–61.

(14) Taylor, J. E.; Milazzo, T. S. *The Journal of Physical Chemistry* **1978**, *82*, 847–852.

(15) Sharma, R. C.; Koshi, M. *Spectrochimica Acta. Part A, Molecular and Biomolecular Spectroscopy* **2006**, *65*, 787–91.

(16) Baldwin, A. C.; Davidson, I. M. T.; Reed, M. D. *Journal of the Chemical Society, Faraday Transactions 1* **1978**, *74*, 2171.

(17) Smith, G. P.; Patrick, R. *International Journal of Chemical Kinetics* **1983**, *15*, 167–185.

(18) Chambreau, S. D.; Zhang, J.; Traeger, J. C.; Morton, T. H. *International Journal of Mass Spectrometry* **2000**, *199*, 17–27.

(19) Chambreau, S. D.; Zhang, J. *Chemical Physics Letters* **2001**, *343*, 482–488.

(20) Murphy, M. K.; Beauchamp, J. L. *Journal of the American Chemical Society* **1977**, *99*, 2085.

(21) Kerr, J. A.; Stephens, A.; Young, J. C. *International Journal of Chemical Kinetics* **1969**, *1*, 339–351.

(22) Davidson, I. M. T.; Stephenson, I. L. *Chemical Communications (London)* **1966**, 746.

(23) Chaundry, A. U.; Gowenlock, B. G. *Journal of Organometallic Chemistry* **1969**, *16*, 221–226.

(24) Wu, Q.; Simmonett, A.; Yamaguchi, Y. *The Journal of Physical Chemistry C* **2009**, *114*, 5447–5457.

(25) Leathard, D. A.; Purnell, J. H. *Annual Review of Physical Chemistry* **1970**, *21*, 197–224.

CHAPTER 8

Pyrolysis of Methyltrichlorosilane, Dimethyldichlorosilane, and Methyldichlorosilane

8.1 Introduction

Interest in the chemistry of chloroorganosilanes has increased in recent years due to their potential as chemical vapor deposition (CVD) precursors for the deposition of silicon carbide (SiC). A variety of chemical precursors for SiC deposition, including tetramethylsilane, silane/propane mixture, and others have historically been investigated and used for the growth of SiC thin films. Chloroorganosilanes, particularly methyltrichlorosilane (CH_3SiCl_3, MTS), have several potential advantages over traditional SiC CVD precursors and have been investigated as SiC CVD precursors for over a decade.[1–7] MTS and other methylchlorosilanes already contain a Si-C bond potentially increasing the ease and kinetics of SiC deposition. These precursors also decompose at relatively low temperatures allowing for a lower thermal energy budget for deposition. In addition, the production HCl upon thermal decomposition of MTS may serve to suppress the preferential deposition of pure Si rather than SiC on Si substrates, easing the production of quality SiC thin films.[8] MTS has been shown to be a useful precursor for the deposition of SiC, presumably due to the presence of a stoichiometric ratio of Si and C atoms in the molecule in addition to the reasons listed above.

Theoretical studies of MTS pyrolysis were performed by Osterheld et al. in 1994 and, later, Ge et al. in 2006.[9–11] Osterheld et al. performed RRKM calculations to estimate kinetic constants for the following potential MTS decomposition pathways.

$$CH_3SiCl_3 \rightarrow {}^{\bullet}CH_3 + {}^{\bullet}SiCl_3 \qquad (8.1)$$

$$CH_3SiCl_3 \rightarrow HCl + CH_2SiCl_2 \qquad (8.2)$$

$$CH_3SiCl_3 \rightarrow {}^{\bullet}H + {}^{\bullet}CH_2SiCl_3 \qquad (8.3)$$

Osterheld et al. predicted pathway 8.1 to be the fastest by about two orders of magnitude over reaction 8.3. Reaction 8.2 was predicted to be insignificant at pressures below 2 Torr but to come within one order of magnitude of reaction 8.1 at higher pressures.

Ge et al. investigated the potential energy surface for the dissociation of MTS using second-order perturbation theory (MP2) with the aug-cc-pVDZ basis set and coupled cluster theory (CCSD(T)) with the aug-cc-pVDZ basis set. They determined forward and reverse Gibbs free energy barriers at 11 temperatures between 0 K and 2000 K for eight potential decomposition pathways. Figure 8.1 summarizes the results of their calculations for Gibbs free energies at the temperature 1400 K. Their results indicate that the barrierless homolysis of the SiC bond (i.e. reaction 8.1) is the most kinetically favorable pathway followed by H atom loss, reaction 8.3. Elimination of methyl chloride, shown as reaction 8.4 below, was found to be the most thermodynamically favorable,

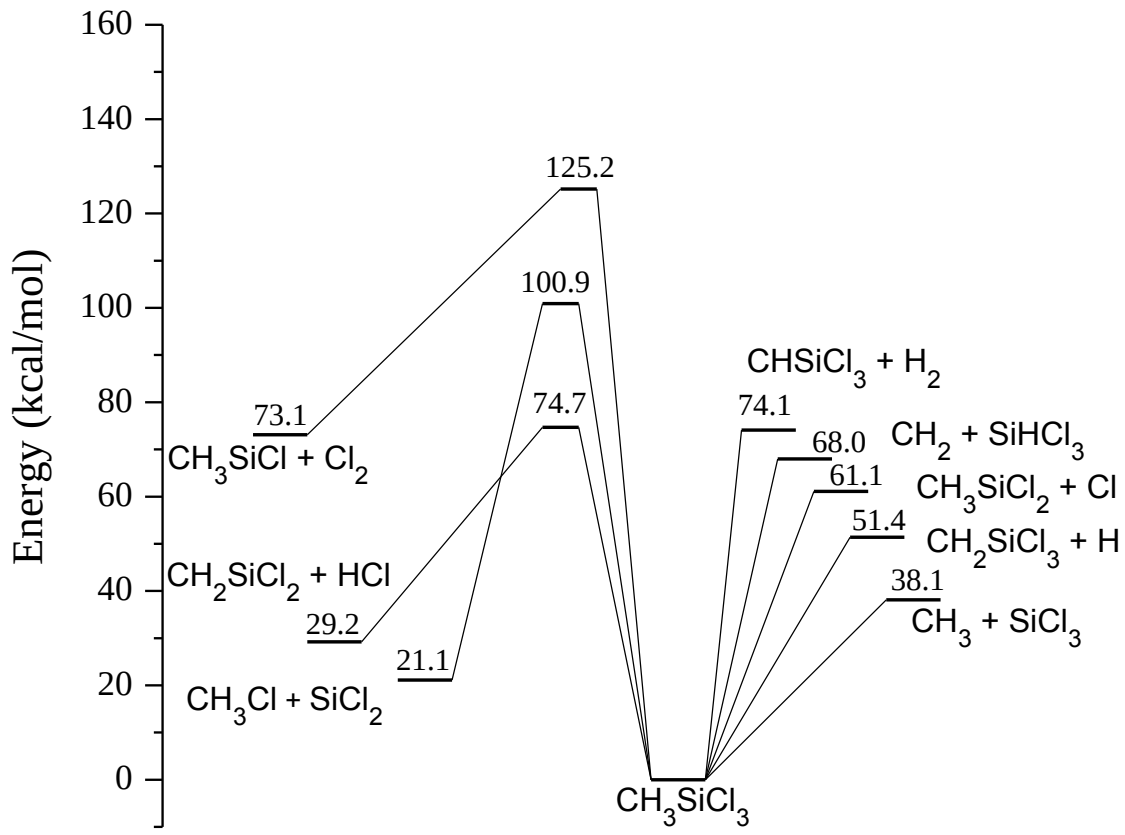

Figure 8.1 Potential energy surface for unimolecular dissociation pathways of methyltrichlorosilane. Figures are obtained from theoretical calculations performed by Ge et. al. in reference 10. Stated energies are Gibbs free energies in kcal mol^{-1} at 1400 K temperature.

with a Gibbs free energy increase of 21.1 kcal mol^{-1} relative to MTS. However, the reaction barrier is quite high at 100.9 kcal mol^{-1}.

$$CH_3SiCl_3 \rightarrow CH_3Cl + SiCl_2 \qquad (8.4)$$

HCl elimination was also found to be competitive thermodynamically with a much lower reaction barrier of 74.7 kcal mol^{-1}.

The thermal decomposition of MTS was first studied experimentally in 2004 by Mousavipour et al. using a flow system coupled with GC/ FID detection. MTS pyrolysis was studied in the temperature range 825 to 977 K and pressure range 10 to 120 torr. Major end products observed were CH_4, CH_3Cl, $SiCl_2$, and CH_2SiCl_2. Influenced by the earlier theoretical work of Osterheld et al., Mousavipour et al. proposed initiation of the pyrolysis by bond homolysis of the Si-C bond and also by molecular elimination of HCl (reactions 8.1 and 8.2) followed by a number of secondary reactions in a 15 equation kinetic model and measured the rate constant of reaction 8.1 to be $(9.6 \pm 2.5) \times 10^9 \exp(-(392 \pm 18)$ kJ mol^{-1} /RT) s^{-1}.

In this study, we investigate the pyrolysis of MTS as well as dimethyldichlorosilane, $Si(CH_3)_2Cl_2$, and methyldichlorosilane, $SiHCH_3Cl_2$. $Si(CH_3)_2Cl_2$ pyrolysis provides information regarding the decomposition of a similar potential CVD precursor containing a non-stoichiometric ratio of Si an C atoms. The mechanism of potential HCl elimination will be elucidated by considering the pyrolysis of $SiHCH_3Cl_2$, which has an H atom attached to Si in contrast with the remaining 3 H atoms all attached to the C atom of the methyl group. Flash pyrolysis vacuum-ultraviolet mass spectrometry (VUV-TOFMS) is used to directly observe reactive intermediates in the pyrolysis of

methyltrichlorosilane, dimethyldichlorosilane, and methyldichlorosilane in the 20-100 μs time scale to improve fundamental understanding of the decomposition kinetics of these molecules, and gain further insight into the SiC deposition process for these potential SiC deposition precursors.

8.2 Experimental

Samples of CH_3SiCl_3 (99%) and $Si(CH_3)_2Cl_2$ (99.5%) were obtained from Sigma-Aldrich. $SiHCl_2CH_3$ (98%) was obtained from Fisher Scientific. All samples were used without further purification. Samples were diluted to approximately 1% concentration in Ar or He carrier gas by passing the carrier gas through the liquid samples contained in glass bubblers immersed in cold temperature baths maintained at approximately -10 ^{0}C using a saturated NaCl and ice solution.

8.3 Results

(a) Pyrolysis of methyltrichlorosilane

Mass spectra for the pyrolysis of MTS in Ar at temperatures 1080 K to 1520 K are shown in Figure 8.2. A room temperature mass spectrum is also included. The parent, MTS, peak does not appear in the spectra due to the fact that the ionization potential of MTS is 11.36 eV, significantly higher than the 10.45 eV provided by ionization photons.[12] However, some photoionization fragmentation (PIF) of MTS does occur due to electron impact ionization as evidenced by small peaks at m/e 113 and 115 that

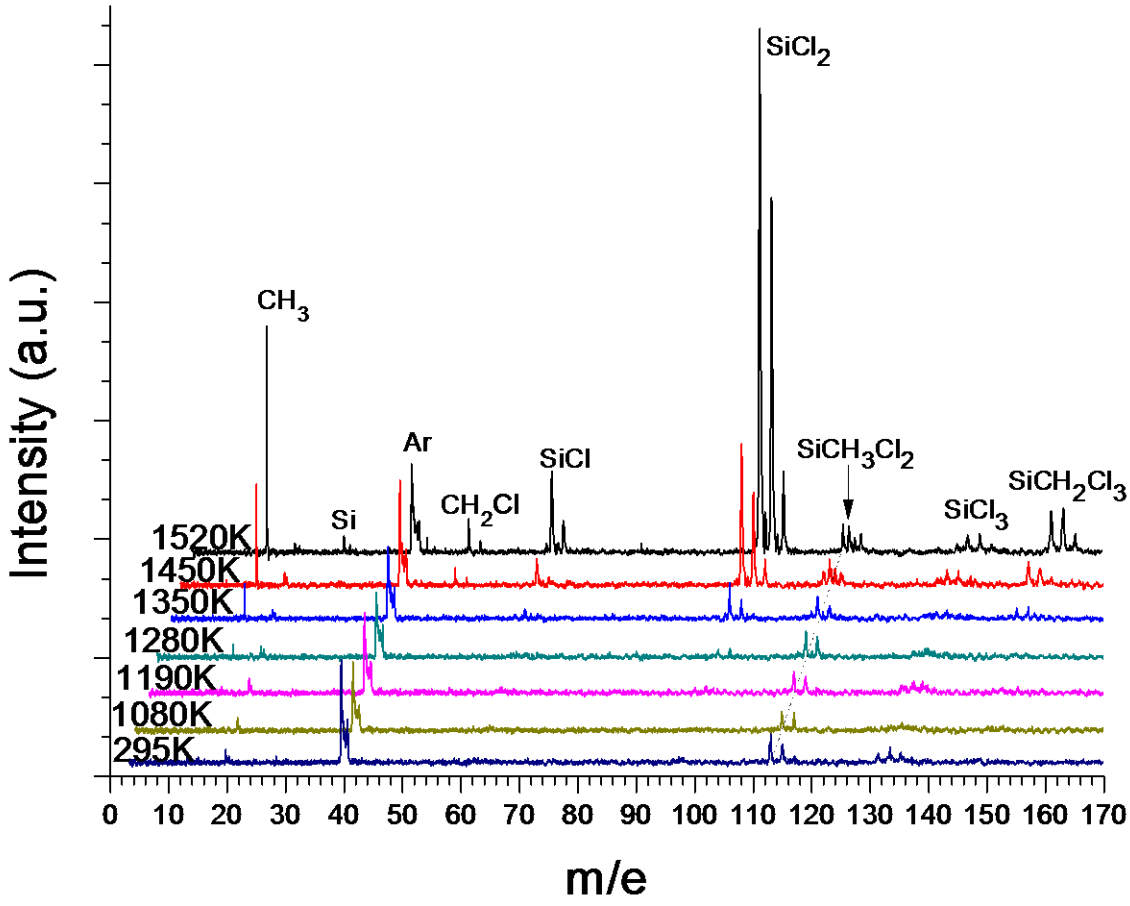

Figure 8.2 Stack plot of mass spectra for pyrolysis of CH_3SiCl_3 (~1%) in Ar at room temperature and pyrolysis temperatures 1080 K to 1520 K. Mass spectra are offset for clarity.

represent $SiCH_3Cl_2^{\bullet+}$. These peaks appear as a doublet at these masses due to the natural isotopic abundances of and ^{35}Cl and ^{37}Cl isotopes. Ar was chosen as the carrier gas over He in this experiment to provide efficient cooling of molecules and limit photoionization fragmentation.

Silicon has three common isotopes ^{28}Si, ^{29}Si, and ^{30}Si with ^{28}Si being the most abundant by far. Natural abundances of Si and Cl isotopes are shown in Table 8.1. Also shown are mass profiles for $SiCl_x$ (x = 1-3) species calculated using natural abundances of Si and Cl and employing combinatorics.

		Percentage Abundance					
$SiCl_x$	Base Mass	Base Mass	Mass +1	Mass +2	Mass +3	Mass +4	Higher Mass
Si	28 amu	92%	5%	3%	0%	0%	0%
Cl	35 amu	76%	0%	24%	0%	0%	0%
SiCl	63 amu	70%	4%	25%	1%	1%	0%
$SiCl_2$	98 amu	53%	3%	36%	2%	7%	0%
$SiCl_3$	133 amu	40%	2%	40%	2%	14%	2%

Table 8.1 Natural isotopic abundances of silicon and chlorine and mass profiles of $SiCl_x$ (x = 1-3) species calculated from natural Si and Cl abundances using combinatorics.

The mass profiles shown in Table 8.1 prove useful in the assignment of peaks in the pyrolysis mass spectra of CH_3SiCl_3, $Si(CH_3)_2Cl_2$, and $SiHCl_2CH_3$, particularly due to the characteristic mass ratios for products containing $SiCl_2$ and $SiCl_3$. For example, the $SiCH_3Cl_2^{\bullet+}$ photfragment appears as a doublet at m/e 113 and 115 with a peak intensity ratio of approximately 3:2, equivalent to the 53% to 36% ratio stated in Table 8.1. A small peak is also predicted at m/e 117 although this peak is barely visible above the baseline due to its very low intensity. A small triplet at m/e 133, 135, and 137 is also

observed in the room temperature spectrum due to PIF forming $SiCl_3^{\bullet+}$ taking the approximate mass profile stated in Table 8.1.

When the temperature of the pyrolysis micro-reactor is heated to 1080 K peaks appear essentially identical to the room temperature spectrum. It is worth noting that peaks at m/e 113 and 115 produced by PIF of MTS at room temperature do not increase with increased nozzle temperatures of 1080 K. This demonstrates the effective cooling provided by supersonic expansion prior to detection assuring that further increases in the intensity of m/e 113 and 115 peaks are solely due to thermal decomposition processes.

The onset of MTS pyrolysis occurs at approximately 1190 K. At this temperature a small peak at m/e 15 is observed indicating loss of methyl from MTS via reaction 8.1. At 1280 K, m/e 15 grows and peaks emerge at m/e 98 and 100 with the 3 to 2 ratio characteristic of $SiCl_2$ being formed via reaction 8.4. CH_3Cl is also produced in this process but it has an ionization energy of 11.22 eV, significantly higher than that of the ionization source in this experiment, so it is not detected.[13]

As the pyrolysis temperature is raised to 1350 K, other pyrolysis processes begin to be observed. Peaks at m/e 98 and 100 increase significantly in intensity. Very small peaks are also observed at m/e 147 and 149 indicating the production of CH_2SiCl_3 by loss of H atom from MTS (i.e. reaction 8.3). The intensity of the m/e 15 methyl peak also increases indicating further decomposition of MTS via reaction 8.1 to produce methyl. The combined intensities of m/e 98 and 100 are about 50% greater than that of m/e 15 indicating the importance of reaction 8.4 at 1350 K.

Given the importance of reaction 8.1, methyl loss from MTS, at 1350 K, observation of peaks at m/e 133, 135, and 137, indicating production of the complement $SiCl_3$, is also expected, but not observed to a significant extent. This is partially due to the fact that the intensity is spread out over 3 peaks, decreasing the intensity of each individual peak. Secondary decomposition of $SiCl_3$ to form SiCl and Cl_2 also appears to be taking place. This is indicated by small peaks at m/e 63 and 65 corresponding to SiCl. The IE of Cl_2 is 11.48 eV, significantly, higher than 10.45 eV, thus it is not detected.[14] Loss of chlorine atom from $SiCl_2$ is also a possible source of SiCl.

$$^{\bullet}SiCl_3 \rightarrow {}^{\bullet}SiCl + Cl_2 \qquad (8.5)$$

At 1450 K, methyl production due to reaction 8.1 continues to increase as the intensity of the m/e 15 peak triples relative to that at 1350 K. $SiCl_3$ peaks at m/e 133, 135, and 137 are clearly visible above the baseline. Secondary decomposition of $SiCl_3$ via reaction 8.5 also continues as exhibited by peaks at m/e 63 and 65 growing in intensity by approximately 4 times relative to the same peaks in the 1350 K spectrum.

Despite the still significant contribution of reaction 8.1 in MTS pyrolysis, reaction 8.4 begins to become the dominant decomposition pathway at temperatures 1450 K and above. Peaks at m/e 98, 100, and 102 increase dramatically in intensity. The peaks exhibit the mass profile characteristic of $SiCl_2$ as shown in Table 8.1. Loss of H atoms from MTS, reaction 8.3, also increases significantly as demonstrated by the 5 fold increase of intensity of the peaks at m/e 147 and 149. A small peak at m/e 151 also becomes visible. The m/e 147, 149, 151 triplet representing $SiCl_3$ has an approximate 3:3:1 ratio as

expected for a product containing one Si atom and 3 Cl atoms. Small peaks are also observed at m/e 112 and 114 indicating the production of $SiCH_2Cl_2$ by molecular elimination of HCl, reaction 8.2. Peaks at m/e 49 and 51 also appear at 1450 K representing the production of CH_2Cl by secondary processes.

Production of all previously mentioned pyrolysis products increases when the pyrolysis temperature is raised to 1520 K. Peak intensities increase by 2 to 2.5 times for all products with the exception of peaks corresponding to $SiCl_2$. Peaks at m/e 98, 100, and 102 increase in intensity over 400% at 1520 K relative to those in the 1450 K spectrum indicating the further dominance of thermodynamically favored reaction 8.4 at high temperature.

(b) Pyrolysis of dimethyldichlorosilane

Mass spectra for the pyrolysis of $Si(CH_3)_2Cl_2$ in He at temperatures 900 K to 1510 K are shown in Figure 8.3. A room temperature spectrum is also shown in which peaks at m/e 128, 130, and 132 representing $Si(CH_3)_2Cl_2$ are observed exhibiting the triplet mass profile characteristic of $SiCl_2$. The ionization energy of $Si(CH_3)_2Cl_2$ is 10.7 eV, somewhat higher that that provided by the ionization source thus only a small proportion of $Si(CH_3)_2Cl_2$ with excess rotational and vibrational energy remaining after supersonic expansion are ionized and detected.[15] For this reason, the intensities of these peaks is relatively low. A peak can also be seen at m/e 56 due to a small amount of contaminant

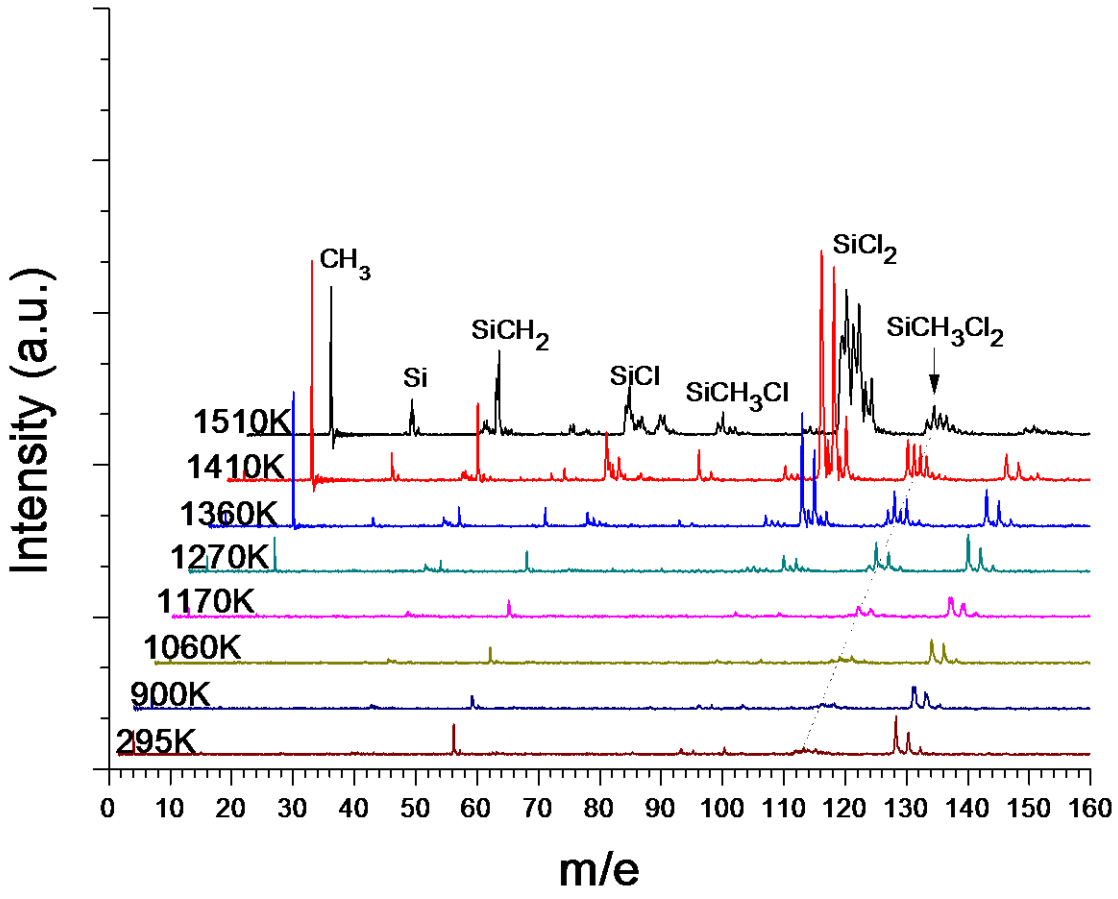

Figure 8.3 Stack plot of mass spectra for pyrolysis of $SiCl_2(CH_3)_2$ (~1%) in He at room temperature and pyrolysis temperatures 900 K to 1520 K. Mass spectra are offset for clarity.

from a prior experiment that could not be completely removed but does not significantly impair the interpretation of the $Si(CH_3)_2Cl_2$ results.

The first signs of $Si(CH_3)_2Cl_2$ pyrolysis are observed when the pyrolysis temperature is raised to 1170 K. Two small peaks emerge at m/e 113 and 115 representing the production of $SiCH_3Cl_2$ by SiC bond homolysis also forming methyl radical. A very small peak is also observed at m/e 15 representing methyl.

$$Si(CH_3)_2Cl_2 \rightarrow {}^{\bullet}SiCH_3Cl_2 + {}^{\bullet}CH_3 \qquad (8.6)$$

Further methyl loss from $Si(CH_3)_2Cl_2$ via reaction 8.6 is observed as the pyrolysis temperature is raised to 1360 K indicated by significant growth of m/e 15 and m/e 113/ 115 peak intensities. Molecular elimination of methane from $Si(CH_3)_2Cl_2$ is observed as a minor process at 1360 K indicated by small peaks at m/e 112 and 114 which represent production of $SiCH_2Cl_2$.

$$Si(CH_3)_2Cl_2 \rightarrow SiCH_2Cl_2 + CH_4 \qquad (8.7)$$

Very small peaks are also observed at m/e 78 and 80 representing $SiCH_3Cl$, likely formed by elimination of CH_3Cl from the parent, $Si(CH_3)_2Cl_2$.

$$Si(CH_3)_2Cl_2 \rightarrow SiCH_3Cl + CH_3Cl \qquad (8.8)$$

Peaks also appear at m/e 98 and 100 indicating the production of $SiCl_2$ by sequential loss of a second methyl radical from $Si(CH_3)_2Cl_2$ as shown as reaction 8.9 below. Despite small contribution of reactions 8.7 and 8.8 to $Si(CH_3)_2Cl_2$ pyrolysis, reaction 8.6 is by far the most dominant $Si(CH_3)_2Cl_2$ decomposition pathway as indicated

not only by the large intensity of the m/e 113/ 115 peaks due to the $^{\bullet}SiCH_3Cl_2$ primary decomposition product but the even larger intensity of the m/e 98 and 100 peaks indicating secondary methyl loss to form $SiCl_2$.

$$^{\bullet}SiCH_3Cl_2 \rightarrow SiCl_2 + {}^{\bullet}CH_3 \qquad (8.9)$$

Other secondary decomposition processes are also observed at 1360 K. Molecular elimination of CH_3Cl from $SiCH_3Cl_2$ results in the formation of SiCl as evidenced by small peaks at m/e 63 and 65. A small but significant peak at m/e 42 is observed due $SiCH_2$ which appears to be formed by secondary elimination of HCl from $SiCH_3Cl$.

$$^{\bullet}SiCH_3Cl_2 \rightarrow SiCl + CH_3Cl \qquad (8.10)$$

$$SiCH_3Cl \rightarrow HCl + SiCH_2 \qquad (8.11)$$

At the highest pyrolysis temperatures 1410 K and 1510 K, sequential loss of methyl radicals via reaction 8.6 and 8.9 continues to be the dominant decomposition pathway for $Si(CH_3)_2Cl_2$ with minor contributions from other aforementioned processes, with reaction 8.8 followed by reaction 8.11 being the most significant.

(c) Pyrolysis of methyldichlorosilane

Mass spectra for the pyrolysis of $SiHCH_3Cl_2$ in He at temperatures 1030 K to 1470 K are shown in Figure 8.4. The included room temperature spectrum does not feature any peaks. Although the ionization energy for $SiHCH_3Cl_2$ is not known, it is not ionized to any extent by the 10.45 eV ionization source in this experiment, and thus

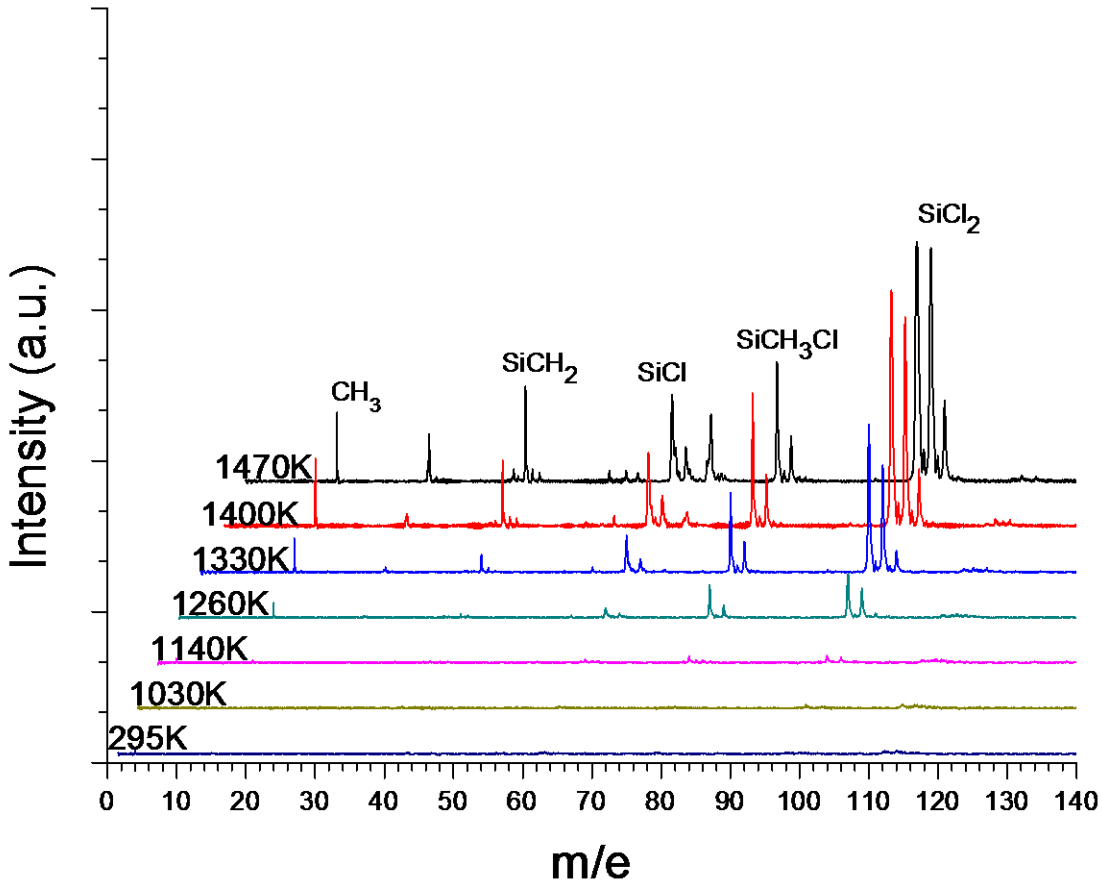

Figure 8.4 Stack plot of mass spectra for pyrolysis of $SiHCl_2CH_3$ (~1%) in He at room temperature and pyrolysis temperatures 1030 K to 1470 K. Mass spectra are offset for clarity.

parent peaks at m/e 114, 116, and 118 are not observed. No pyrolysis of $SiHCH_3Cl_2$ is observed at nozzle temperatures 1030 K and 1140 K.

The onset of pyrolysis is observed at 1260 K. The highest intensity peaks are observed at m/e 98 and 100, indicating significant production of $SiCl_2$ formed by the molecular elimination of methane as shown by reaction 8.12 below. Also observed are peaks at m/e 78 and 80 corresponding to $SiCH_3Cl$ which results from the molecular elimination of HCl written at reaction 8.13 below.

$$SiHCH_3Cl_2 \rightarrow SiCl_2 + CH_4 \qquad (8.12)$$

$$SiHCH_3Cl_2 \rightarrow SiCH_3Cl + HCl \qquad (8.13)$$

Very small peaks are also observed at m/e 63 and 65 representing the production of SiCl likely due to a secondary reaction involving the cleavage of the Si-C bond in $SiCH_3Cl$ producing SiCl and methyl radical. A small peak due to methyl at m/e 15 is also observed.

$$SiCH_3Cl \rightarrow {}^{\bullet}SiCl + {}^{\bullet}CH_3 \qquad (8.14)$$

As the pyrolysis temperature is increased to 1330 K, all of the aforementioned decomposition processes occur to a greater extent, but in approximately the same proportions. Combined $SiCl_2$ peak intensities at m/e 98, 100, and 102 indicating reaction 8.12 are about three times those of the m/e 78 and 80, $SiCH_3Cl$, peaks corresponding to reaction 8.13. Small peaks at m/e 42 and 43 are also observed at 1330 K as a result of $SiCH_2$ produced by secondary HCl elimination from $SiCH_3Cl$.

As the pyrolysis temperature is raised to 1400 K and 1470 K, all prior decomposition processes continue to occur to an increasing extent. Notably, the m/e 42 peak becomes quite large relative to m/e 43 indicating production of C_3H_6 due to methyl secondary reactions. Additionally a peak at m/e 68 is also observed representing C_5H_8 also due to secondary reaction of methyl radicals.

8.4 Discussion

Major decomposition pathways for MTS are summarized in Scheme 8.1. The MTS pyrolysis results from this study appear to generally support relative product and reactant Gibbs free energies determined by theoretical calculations recently performed by Ge et al.[10] Si-C bond homolysis to form methyl radical via reaction 8.1 is the dominant decomposition process at the lowest pyrolysis temperatures (~1280 K) as expected since this process has the lowest reaction barrier according to their calculations.

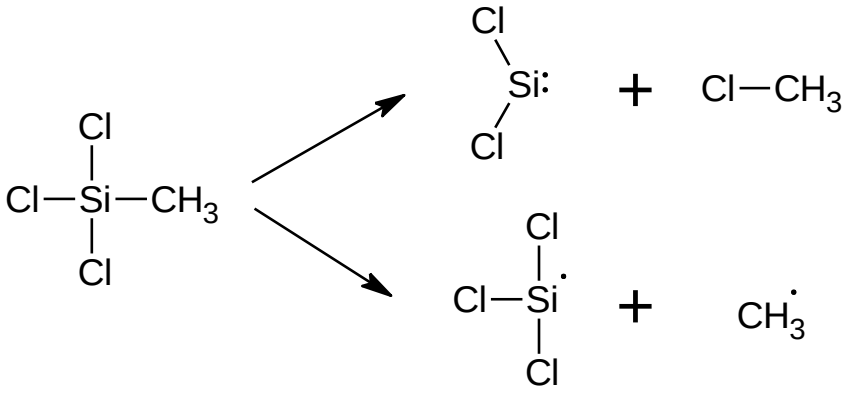

Scheme 8.1 Major decomposition pathways of methyltrichlorosilane.

As the pyrolysis temperature is increased, $SiCl_2$ production due to molecular elimination of chloromethane via reaction 8.4 becomes increasingly dominant. This provides evidence that reaction 8.4 is the most thermodynamically favorable pathway as determined by Ge et al.

Calculated transition state Gibbs free energies appear to be less accurate. The calculated barrier of 100.9 kcal mol^{-1} for reaction 8.4 appears to be too high to sufficiently explain the dominance of $SiCl_2$ production by reaction 8.4 relative to other competitive processes, particularly H atom loss form MTS by homolysis of the C-H bond that is part of the methyl group. Given the relatively low energy requirement for H atom loss, it would be expected to be much more prevalent than observed in this study.

Reaction 8.2, HCl elimination, is also only observed to a very limited extent although it was presumed to be a relatively significant process given the theoretical results of Osterheld, et al., and Ge. et al., and in the kinetic model of Mousavipour et al. The transition state barrier for HCl elimination from MTS was calculated to be significantly lower than that of reaction 8.4 at 74.7 kcal mol^{-1} for reaction 8.2 versus, 100.9 kcal mol^{-1} for reaction 8.4. This does not appear consistent with observations in this study. HCl elimination is relatively limited at all temperatures.

Major decomposition pathways of dimethyldichlorosilane are shown in Scheme 8.2. Decomposition of $Si(CH_3)_2Cl_2$ is driven by Si-C bond homolysis via reaction 8.6 as evidenced by significant $SiCH_3Cl_2$ production at temperatures as low as 1170 K. MTS and $Si(CH_3)_2Cl_2$ both follow a methyl radical loss process at temperatures approximately 1350 K and below. Above these temperatures methyl chloride elimination dominates in

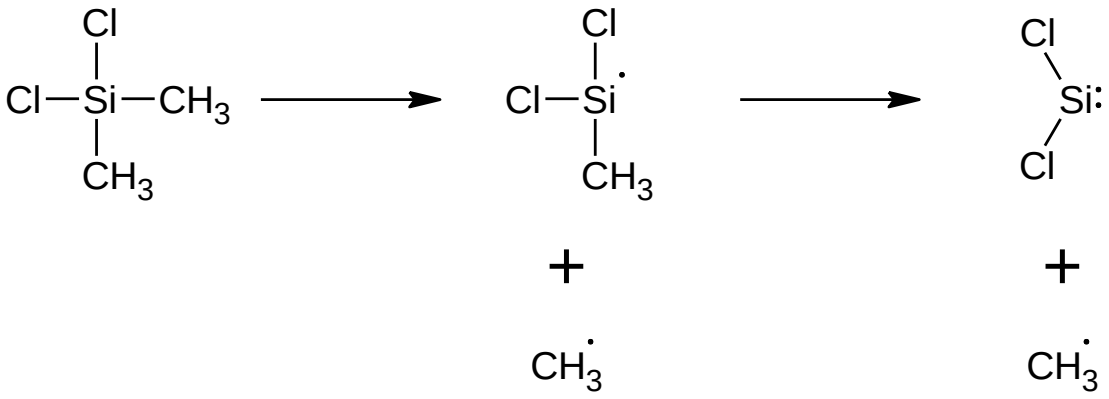

Scheme 8.2 Major decomposition pathways of dimethyldichlorosilane.

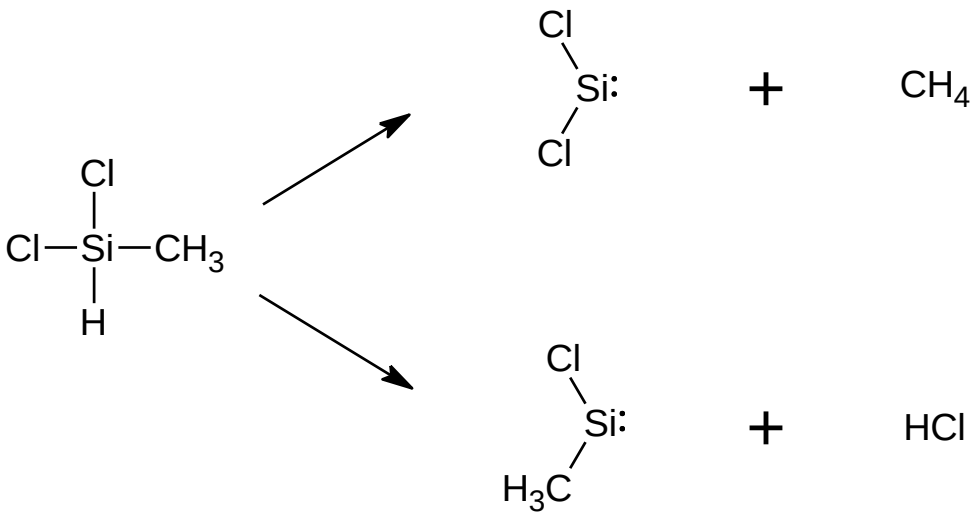

Scheme 8.3 Major decomposition pathways of methyldichlorosilane.

MTS pyrolysis. However elimination of methyl chloride is not a significant decomposition pathway for $Si(CH_3)_2Cl_2$ which instead continues to lose sequential methyl radicals with methyl and $SiCl_2$ being the primary decomposition products at high temperatures. Whereas $Si(CH_3)_2Cl_2$ decomposition primarily occurs by Si-C bond homolysis reactions, decomposition of $SiHCH_3Cl_2$ occurs mostly by molecular elimination of methane and HCl, as shown in Scheme 8.3, presumably due to the availability of a H bonded to Si, the Si-H bond being significantly weaker than the C-H bonds on MTS.

Notably, $SiCl_2$ is the dominant high temperature product in the pyrolysis of all three substances studied here, yet little is now known about its structure and energetics. Given, that it is so prevalent in the pyrolysis of MTS, $Si(CH_3)_2Cl_2$, and $SiHCH_3Cl_2$, it is likely to be and important intermediate in CVD deposition from a number of chloroorganosilane precursors. Given the importance of the $SiCl_2$ intermediate, further theoretical and experimental study of $SiCl_2$ is well warranted.

Conclusion

Unimolecular thermal decomposition of methyltrichlorosilane (CH_3SiCl_3) , dimethyldichlorosilane ($Si(CH_3)_2Cl_2$), and methyldichlorosilane ($SiHCH_3Cl_2$) was performed on the 20-100 μs time scale. Pyrolysis of CH_3SiCl_3 proceeds primarily by Si-C bond homolysis to form $SiCl_3$ and methyl radicals at temperatures of approximately 1200 K to 1350 K. Above 1350 K, molecular elimination of CH_3Cl to form $SiCl_2$ becomes increasingly important as the pyrolysis temperature is increased with other minor

pyrolysis pathways including C-H bond fission and HCl elimination also contributing. Pyrolysis of $Si(CH_3)_2Cl_2$ occurs almost exclusively by sequential loss of methyl radicals ultimately forming $SiCl_2$ in significant concentrations. Pyrolysis of $SiHCH_3Cl_2$ involves molecular elimination of both methane and HCl in an approximately 3 to 1 ratio. $SiCl_2$ is produced in significant concentrations indicating that it is an important intermediate in SiC CVD from chloroorganosilanes.

References

(1) Leone, S.; Henry, A.; Janzén, E.; Nishizawa, S. *Journal of Crystal Growth* **2013**, *362*, 170–173.

(2) Liu, C.; Yang, Y.; Luo, X. *Journal of Wuhan University of Technology-Mater. Sci. Ed.* **2012**, *27*, 871–875.

(3) It, M.; Besmann, T. M.; Sheldon, B. W.; Moss, T. S.; Kaster, M. D. *Journal of the American Ceramic Society* **1992**, *75*, 2899.

(4) Sone, H.; Kaneko, T.; Miyakawa, N. *Journal of Crystal Growth* **2000**, *219*, 245–252.

(5) Loumagne, F.; Langlais, F.; Naslain, R. *Journal of Crystal Growth* **1995**, *155*, 198–204.

(6) Cagliostro, D.; Riccitiello, S. *Journal of the American Ceramic Society* **1993**, *76*, 49–53.

(7) Cagliostro, D. E.; Riccitiello, S. R.; Carswell, M. G. *Journal of the American Ceramic Society* **1990**, *73*, 607–614.

(8) Papasouliotis, G. D.; Sotirchos, S. V. *Journal of Materials Research* **1999**, *14*, 3397–3409.

(9) Osterheld, T. H.; Allendorf, M. D.; Melius, C. F. *The Journal of Physical Chemistry* **1994**, 6995–7003.

(10) Ge, Y.; Gordon, M. S.; Battaglia, F.; Fox, R. O. *The Journal of Physical Chemistry A* **2007**, *111*, 1462–74.

(11) Ge, Y.; Gordon, M. S.; Battaglia, F.; Fox, R. O. *The Journal of Physical Chemistry A* **2010**, *114*, 2384–92.

(12) Steele, W.; Nichols, L.; Stone, F. *Journal of the American Chemical Society* **1962**, *981*, 4441–4445.

(13) Hochmann, P.; Templet, P. H.; Wang, H. T.; McGlynn, S. P. *Journal of Chemical Physics* **1975**, *60*, 3650.

(14) Yencha, A. J.; Hopkirk, A.; Hiraya, A.; Donovan, R. J.; Goode, J. G.; Maier, R. R. J.; King, G. C.; Kvaran, A. *The Journal of Physical Chemistry* **1995**, *99*, 7231.

(15) Green, M. C.; Lappert, M. F.; Pedley, J. B.; Schmidt, W.; Wilkins, B. T. *The Journal of Organometallic Chemistry* **1971**, *31*, 55.

CHAPTER 9

Conclusion

Investigation of the initial steps of thermal decomposition mechanisms of important fossil fuel components and SiGe, GeC, SiC chemical vapor deposition (CVD) precursors was performed using flash pyrolysis vacuum-ultraviolet time-of-flight mass spectrometry. Benzyl radical, the primary decomposition product of toluene, was confirmed to thermally decompose via loss of H atom after isomerization with loss of H atom from the side chain being preferred. Pyrolysis of linear alkanes by C-C bond cleavage to form two free radicals was directly observed. Fission of central C-C bonds occurred most rapidly and cleavage of the α C-C bond to form methyl radical was not significant. Decomposition of 1-butyl and 1-pentyl radicals by β-scission and loss of H atom was confirmed and significant 1,4-H migration prior to β-scission was observed for the 1-pentyl radical.

Formation of highly unsaturated gas phase $Si_xGe_yH_z$ (x=1-3, y=1,2,3, and 5) clusters was observed upon pyrolysis of one to one SiH_4/GeH_4 mixture due to a silylene/ germylene insertion mechanism. Tetramethylgermane $Ge(CH_3)_4$, underwent loss of sequential methyl radicals and significant secondary formation of Ge and Ge_2 was observed. Loss of methyl radical was also observed in the pyrolysis of tetramethylsilane, $Si(CH_3)_4$, along with secondary H atom loss from $^{\bullet}Si(CH_3)_3$ followed by successive H_2 elimination reactions. Pyrolysis of important SiC precursor, methyltrichlorosilane, was

observed and proceeded primarily by Si-C bond homolysis to form $SiCl_3$ and methyl radicals at temperatures lower pyrolysis temperatures 1200 K to 1350 K, and molecular elimination of CH_3Cl to form $SiCl_2$ at higher temperatures, supporting recent theoretical calculations. Pyrolysis mechanisms of alternative SiC CVD precursors dimethyldichlorosilane, $Si(CH_3)_2Cl_2$, and methyldichlorosilane, $SiHCH_3Cl_2$, were also investigated. $Si(CH_3)_2Cl_2$ mainly underwent SiC bond homolysis while $SiHCH_3Cl_2$ pyrolysis was dominated by HCl and CH_4 molecular elimination.